INSTITUTO SUPERIOR TÉCNICO
Universidade Técnica de Lisboa

Analysis of the viscous/molecular subgrid-scale dissipation terms in LES based on transport equations: *A priori* tests

Sara Tavares Rego

Dissertação para obtenção do Grau de Mestre em

Engenharia Aeroespacial

Júri

Presidente:	Prof. Fernando José Parracho Lau
Orientador:	Prof. Doutor José Carlos Fernandes Pereira
Co-Orientador:	Doutor Carlos Frederico Neves Bettencourt da Silva
Vogal:	Prof. João Manuel Melo de Sousa

Setembro de 2008

Acknowledgements

Foremost, I would like to thank my supervisors Professor José Carlos Pereira and Doctor Carlos Bettencourt da Silva for the opportunity of working and learning from them. They were allways there to share their knowledge and expertise on the subject, providing me with all the support I needed.

Furthermore, I would like to thank to all my colleagues at LASEF, for their advice and support, without which things would certainly have been more difficult.

And finally, I want to thank my family and friends for all their love.

Resumo

Na simulação das grandes escalas, alguns modelos sub-malha são baseados na utilização de uma equação de transporte adicional para a evolução da energia cinética sub-malha. Do mesmo modo, em problemas onde se pretende estudar a dinâmica de um escalar, utiliza-se uma equação de transporte para a variância do escalar sub-malha. Nestas equações figuram quantidades sub-malha que, não estando disponíveis no momento em que se realizam as simulações das grandes escalas, têm de ser modeladas. O objectivo deste trabalho é analisar três modelos para os termos de dissipação viscosa/molecular sub-malha que aparecem nestas equações.

Os modelos estudados foram (a) o modelo clássico usado por Schumann (1975) [1] e Yoshizawa (1982) [2], (b) o modelo baseado em modelos híbridos RANS/LES de Paterson e Peltier (2005) [3] e Hanjalic (2005) [4], e (c) o modelo para a dissipação da variância do escalar sub-malha usado por Jiménez *et al.* (2001) [5]. O comportamento estatístico dos modelos foi aferido através de testes *a priori* a uma base de dados calculada com simulações numéricas directas (da Silva e Pereira (2007) [6]).

Tanto os modelos clássicos como o modelo para a dissipação molecular da variância do escalar sub-malha de Jiménez *et al.* [5] demonstraram bons resultados nos testes *a priori*. Os modelos baseados em modelos híbridos apresentaram um comportamento pior.

Palavras-chave: Modelos sub-malha, Dissipação viscosa/molecular sub-malha, Turbulência isotrópica, Simulações Numéricas Directas

Abstract

Some subgrid modelling strategies in large eddy simulations (LES) involve the use of a transport equation for the subgrid-scale (SGS) kinetic energy. Likewise, for problems regarding active or passive scalar fields, a SGS scalar variance transport equation is also used. The terms from these transport equations comprise sub-filter scale quantities that are not accessible during LES and thus require modelling. Our main focus here concerns the modelling the viscous and the molecular SGS dissipation terms, for which three strategies are assessed.

The models assessed here are (a) the classical model (Schumann (1975) [1], Yoshizawa (1982) [2]), (b) the model used in hybrid RANS/LES (Paterson and Peltier (2005) [3], Hanjalic (2005) [4]), and (c) the model for the molecular SGS dissipation of SGS scalar variance from Jiménez *et al.* (2001) [5]. *A priori* tests are performed to the data bank results from direct numerical simulations of statistically stationary homogeneous isotropic turbulence (da Silva and Pereira (2007) [6]) and the behaviour of these models is interpreted by means of statistical analysis and spectra from the exact and modelled molecular SGS dissipations.

Both classical models for the molecular SGS dissipation and the model from Jiménez *et al.* for the molecular SGS dissipation of SGS scalar variance yield very good results, whereas the models tested here and used in hybrid RANS/LES give poor results.

Keywords: Subgrid-scale modelling, Viscous/molecular SGS dissipation, Isotropic turbulence, Direct Numerical Simulations

Contents

Acknowledgements i

Resumo ii

Abstract iii

List of Figures vi

I Background 1

1 Introduction 2
1.1 Turbulence . . . 2
1.1.1 Characteristics of a turbulent flow . . . 2
1.1.2 Scales in a turbulent flow . . . 3
1.2 Numerical simulations . . . 5
1.2.1 Reynolds-averaged Navier-Stokes . . . 6
1.2.2 Direct numerical simulations . . . 7
1.2.3 Large eddy simulations . . . 7
1.3 Homogeneous isotropic turbulence . . . 8
1.4 Objective of this work . . . 9
1.5 Organization of the thesis . . . 9

2 Large eddy simulations 10
2.1 Governing equations . . . 11
2.2 Filtered equations . . . 13
2.2.1 The filtering procedure . . . 13
2.2.2 Application to the flow equations . . . 15
2.3 Subgrid-scale models . . . 17
2.4 Models based on transport of $\tau_{ii}/2$ and $q_\theta/2$ . . . 25
2.4.1 Transport equation for the SGS kinetic energy . . . 25
2.4.2 Transport equation for the SGS scalar variance . . . 26
2.4.3 Modelled transport equations . . . 26
2.4.4 Models for the viscous and molecular SGS dissipation terms . . . 26

3 Data bank 28
3.1 Direct numerical simulations of homogeneous isotropic turbulence . . . 28
3.2 Numerical code . . . 29
3.2.1 Pseudo-spectral methods . . . 29
3.2.2 Third-order Runge-Kutta method . . . 30

4 *A priori* tests **31**
4.1 *A priori* tests: setting up the variables 31
4.2 *A priori* tests: analysis on the physical space 33
4.3 *A priori* tests: analysis on the Fourier space 37

II Results: Article published in the Journal of Turbulence **38**

List of Figures

1.1 Flow over a cylinder: two realizations. Source: Davidson [7]. 3
1.2 Different scales on a turbulent ring. Source: Tsinober [8]. 4
1.3 Richardson's energy cascade. Source: Davidson [7]. 5
1.4 Kinetic energy spectrum. Source: Wilcox [9]. 6
1.5 Homogeneous flow past a grid. Source: Tsinober [8]. 8

2.1 Turbulent flow signal decomposed in a filtered and subgrid component. From Frisch [10]. 14
2.2 Box filter. From Sagaut [11]. 15
2.3 Energy transfer function in wave number space. Source: Davidson [7]. 21

3.1 Computational domain and instantaneous turbulent field. Courtesy: C. Silva. . 29
3.2 Kinetic energy and scalar variance spectra from all direct numerical simulations. From [6]. 30

4.1 A function with positive skewness. Source: Tennekes and Lumley [12]. 35
4.2 Functions with small and large kurtosis. Source: Tennekes and Lumley [12]. . . 36

Part I

Background

Chapter 1

Introduction

In the present section, some of the very basic issues of turbulence models are presented. Large eddy simulations are becoming an increasingly important tool to solve turbulent flows and one critical issue regarding these simulations is concerned with the modelling of the small scales. This introductory section is aimed at delivering the proper background information required to a better understanding of the formalisms and discussions which will follow.

1.1 Turbulence

Many examples of turbulent flows can be found in our everyday lives. For example, the motion of fluid flow in the atmosphere or in the ocean is, to a significant proportion, turbulent. Almost all the boundary layers around flying aircrafts are turbulent. Turbulence also has an important role in the dispersion of pollutants that come out of car exhausts or factory chimneys. Turbulent external flows around transport vehicles are responsible for an increased aerodynamic drag force and, directly related to this, an additional fuel consumption.

1.1.1 Characteristics of a turbulent flow

Turbulent flows are originated by the amplification of small scale disturbances imposed to the flow. Besides the disturbances to which a fluid flow is subject, another important criterion that serves as an indicator of whether or not the flow characteristics are favourable to the occurence of turbulence is the dimensionless Reynolds number defined by $\mathtt{Re} = \mathtt{u}\mathtt{l}/\nu$, where $\mathtt{u}$ and $\mathtt{l}$ are the flow characteristic velocity and length scales and ν is the kinematic viscosity of the fluid. Turbulence arises in flows at high Reynolds numbers.

Unlike in a laminar flow regime, where the motion of the flow has an orderly and smooth nature, a turbulent flow is characterized by a highly irregular and chaotic velocity field associated with the presence of coherent structures, eddies, of many different lengthscales.

Despite a rather chaotic and unpredictable behaviour, turbulent flows are known to possess stable statistical properties [8]. For instance, if an experiment is performed twice, with the same initial and boundary conditions, and the instantaneous value of a given flow variable is measured in each one of these experiments, the details of the measured signals will differ strongly from

one experiment to the other. This behaviour, represented on figure 1.1, is due to the extreme sensitivity of turbulent flows to small disturbances. However, the statistics of both sets of

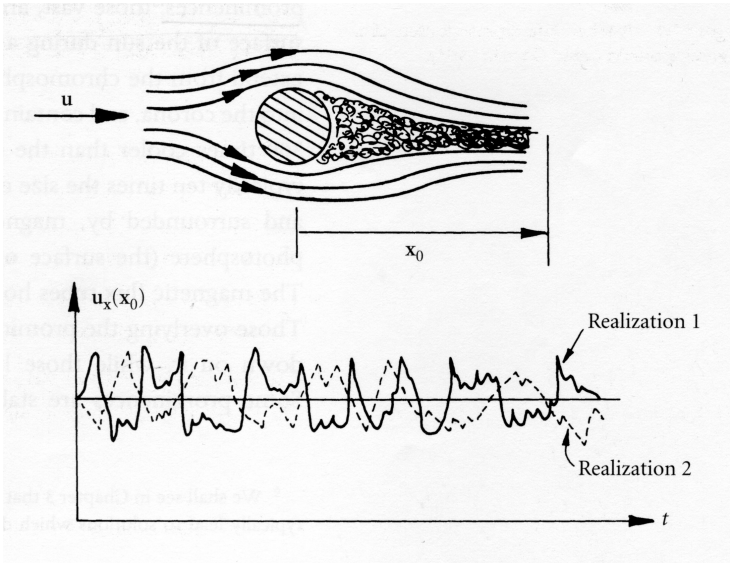

Figure 1.1: Representation of a flow over a cylinder. Two measurements of the instantaneous velocity, $u_x(t)$, are made at x_0 for two realizations of the experience with the same initial and boundary conditions. Source: Davidson. [7]

mesurements are likely to present a similar behaviour, for example, the mean value is supposed to be the same for both signals.

Another important characteristic of a turbulent flow is its great ability to mix fluid, which has a direct impact on the rates of heat and mass transfer, for example. It is this mixing capability which is responsible for the uniform temperature inside a room and that ensures an efficient mixing between fuel and oxidizer in combustion processes or a relatively fast dispersion of pollutants in the atmosphere. In a laminar flow field mixing is only due to molecular diffusion, but mixing rates in turbulent flows largely exceed the molecular diffusion rates, the difference between both being more than a couple orders of magnitude [12].

1.1.2 Scales in a turbulent flow

The dynamics of a turbulent flow is characterized by the existence of a wide range of eddies of different length scales, as represented on figure 1.2. Large scales, of the order of the integral scale l, arise from instabilities in the mean flow and their maximum dimension is dictated by the flow's boundary conditions, thus they are accountable for most of the energy extraction from the mean flow field to the turbulent fluctuating field. Just like the mean flow, larger turbulent scales are also subject to inertial instability mechanisms and, as a result, they give rise to smaller eddies and this process repeats itself until the size of the smallest eddies is so small that their frail structure can no longer subsist to the action of molecular viscosity. The Kolmogorov micro-scale η characterizes the dimension of the smallest possible scale in a turbulent flow.

In 1922, English physicist Lewis Richardson introduced the *energy cascade* concept to explain

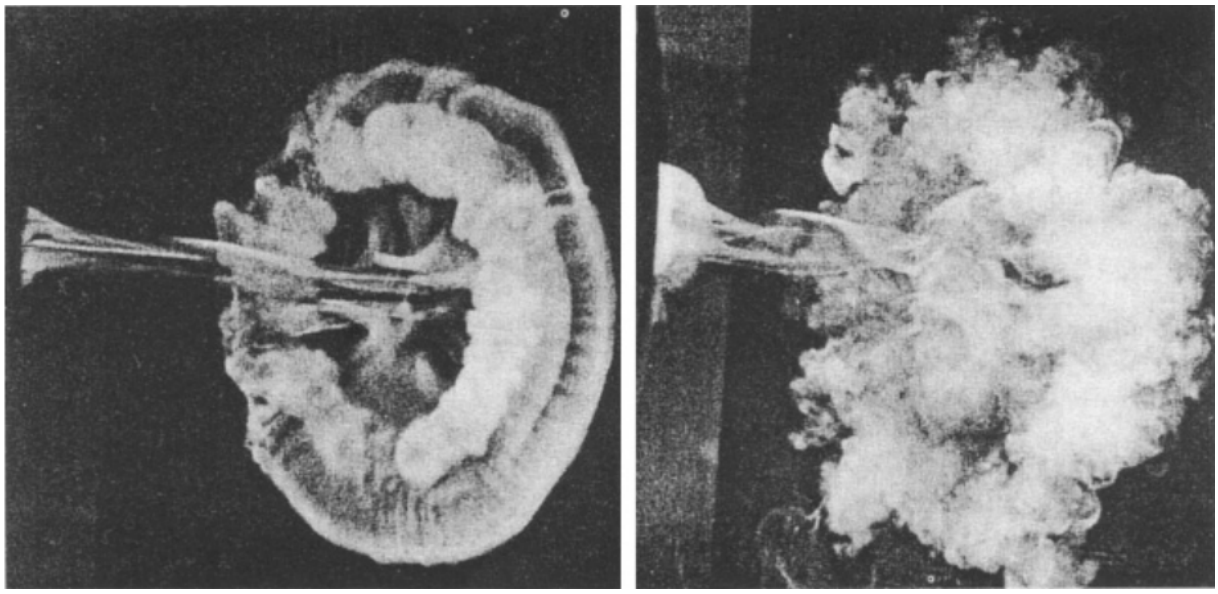

Figure 1.2: In this picture we observe a sudden transition to turbulence in a laminar vortex ring. It is possible to identify the different length scales on the turbulent ring (right). Source: Tsinober [8].

how turbulent kinetic energy, the kinetic energy associated with turbulent velocity fluctuations, is transferred through the turbulent flow scales. This concept is based on a hierarchical description of the interactions between the different flow scales, where the inertial instability mechanisms to which the flow structures are subject cause them to originate subsequently smaller eddies until they reach the smallest physically possible size. This idea is represented on figure 1.3. During the entire process there is a continuous energy flux from the larger to the smaller flow structures, an *energy cascade*. Because the Reynolds number is large in turbulent flows, viscosity does not play a significant role in most part of the energy cascade process, intervening only at the end, when the Reynolds number based on the eddy size is of order of unity. This scenario, $\mathsf{Re} \sim 1$, only comes across for the smallest eddies and thus the action of the viscous forces, which results in the final dissipation of the turbulent kinetic energy, is associated with the smallest coherent structures.

Overall, kinetic energy in a turbulent flow is transferred from the large scales to the small as illustrated by the energy cascade concept (forward energy transfer), however we can find local regions in the flow where energy flows from the small to the large scales (backward energy transfer).

One tool commonly used to evaluate how the turbulent kinetic energy is distributed across the different lengthscales of a turbulent flow is the energy spectrum function. The energy spectrum function represents the contribution to the turbulent kinetic energy from eddies with wave number k, where the wave number is associated with a characteristic scale for the eddy size r by $\mathsf{k} = 2\pi/\mathsf{r}$. From observation of a typical energy spectrum function sketch on figure 1.4, we can infere that the turbulent scales with a lower k, i.e. the larger scales, carry the largest amount of the energy in a turbulent field and therefore they are often designated by energy containing

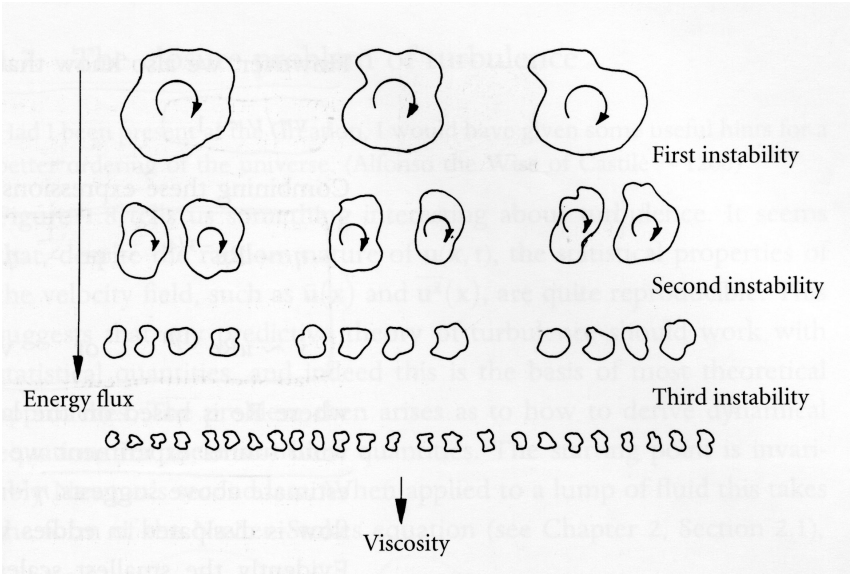

Figure 1.3: Schematic representation of Richardson's energy cascade. This concept is based on a continuous energy flux from the larger to the smaller structures of turbulent flows. Source: Davidson [7].

eddies. On the other hand, smaller scales contribute with the smallest amount of kinetic energy and they are related with the end of the energy transfer mechanism. They are the dissipative scales. In between, energy is transferred from the energy containing eddies to the dissipative scales and the wave numbers in that range are said to belong to the inertial sub-domain range.

The boundary conditions of a turbulent flow define the shape of the larger scale eddies. Their structure depends on whether we are dealing with turbulent jets, wakes or boundary layers. However, after being subject to a series of instability mechanisms upon which new smaller eddies are generated, the anisotropy of the flow structures starts to slowly fade away and the resulting eddies only feel the larger scales by the energy flux arriving to them. This is what Kolmogorov defined in his universal equilibrium theory (1941) by *local isotropy* and *statistical equilibrium*, respectively. It must be stated that Kolmogorov's theory was postulated for turbulent flows at high Re numbers and, in this frame of reference, scales belonging to the *universal equilibrium range* possess a number of universal characteristics and are independent from the larger scales, and thus from the type of flow where they exist. The universal equilibrium range encompasses the inertial sub-domain and the dissipative scales of the energy spectrum.

1.2 Numerical simulations

The advent of digital computers on the second half of the twentieth century and the continuous growth in computer processing capacity that has taken place over the years has encouraged the use of numerical simulations of turbulence. In fact, numerical simulations have become increasingly employed to study a turbulent flow field or to predict its behaviour in engineering applications. Some of the advantages of performing numerical simulations are that we can

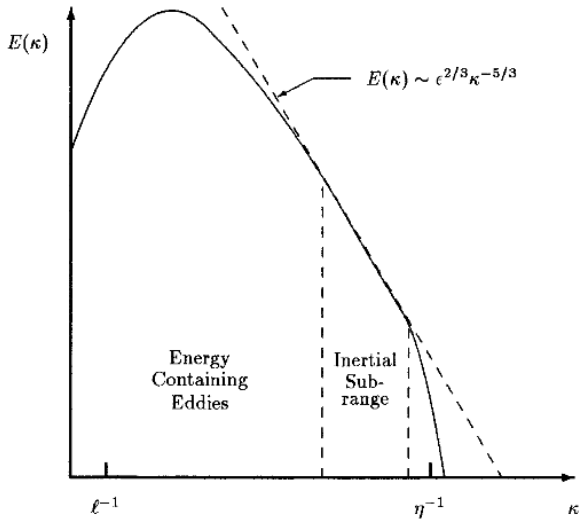

Figure 1.4: Sketch representing a typical energy spectrum of a turbulent flow field. Source: Wilcox [9].

recover a huge amount of computed data, for instance the values of the computed flow variables at each point of the computational mesh, and that the study of different flow configurations is enabled by a relatively simple modification of initial and boundary conditions.

A turbulent flow can be simulated according to different types of numerical computations. In some, only the mean fluid flow can be predicted and others can capture the instantaneous and chaotic essence of turbulence. However, the more of a turbulent flow we can predict, the more we pay in computer time. In this section, three numerical simulations used in the calculation of turbulent flows will be introduced: one where only the mean flow is computed while the effect of the entire turbulent fluctuating field is modelled, another one where all the scales of turbulence are calculated, and last one where some turbulent scales are directly calculated and the absence of the remaining scales is modelled.

1.2.1 Reynolds-averaged Navier-Stokes

By the end of the nineteenth century, physicist Osborne Reynolds suggested that any given turbulent flow variable could be interpreted as the sum of its ensemble average and a fluctuation from the average value, $\mathbf{u}(\mathbf{x}, \mathrm{t}) = \langle \mathbf{u}(\mathbf{x}, \mathrm{t}) \rangle + \mathbf{u}''(\mathbf{x}, \mathrm{t})$. If the flow variables present on the the Navier-Stokes equations are replaced by their Reynolds decomposition we end up with the Reynolds equations. The purpose of a Reynolds-averaged Navier-Stokes (RANS) simulation is to solve the Reynolds equations. The Reynolds equations are the equivalent of the Navier-Stokes equations for $\langle \mathbf{u}(\mathbf{x}, \mathrm{t}) \rangle$ with an additional term, the Reynolds stress tensor, which arises from the non-linearity of the Navier-Stokes equations and is given in terms of $\mathbf{u}''(\mathbf{x}, \mathrm{t})$. The Reynolds stress tensor represents the transport of momentum due to turbulent fluctuations and accounts for the effects of the entire turbulent field on the mean flow. This term has to be modelled in order to enable the computation of the mean flow field, $\langle \mathbf{u}(\mathbf{x}, \mathrm{t}) \rangle$, which is the aim

in Reynolds-averaged Navier-Stokes simulations.

There are considerable limitations to the RANS technique owing to the fact that turbulent flow features cannot be predicted, only time averaged flow calculations can be obtained. Nevertheless, RANS simulations are still widely used in engineering applications and the reason for their popularity is its low computational cost, which makes RANS the only possible solution for complex and highly demanding flow computations.

1.2.2 Direct numerical simulations

In the 1970s, Steve Orzag and Stu Patterson carried out the first direct numerical simulations. Direct numerical simulations (DNS) consist in computing directly the Navier-Stokes equations without any kind of modelling assumption. In order to get rid of any type of turbulence modelling, the computational mesh for a DNS has to account for all turbulent flow scales. However, the range of dynamically important scales in a turbulent flow is quite large, specially in high Reynolds number flows, and this implies a very high computational cost. High-accuracy discretization schemes can be employed, reducing the computational effort for a DNS and thus allowing for a higher Reynolds number calculation, but such discretization methods are restricted to simple flow geometries. As a result, DNS are limited to low-to-moderate Reynolds number and relatively simple flow configurations. Despite a clear inability to handle high Reynolds turbulent flows, which comprise many engineering flows, direct numerical simulations are a very important tool in fundamental research of turbulent flows or in the assessement of modelling premises employed in other types of numerical simulations.

1.2.3 Large eddy simulations

The concept of large eddy simulations is due to Smagorinsky circa 1963, but the first results from LES were obtained by Deardorff in early 1970s for a plane channel flow [13]. In large eddy simulations (LES) the large scale motions of a turbulent flow are directly calculated while the effect of the small unresolved scales is modelled via an additional term in the transport equations. A filtering operation is performed in order to be possible to solve adequately the resulting filtered velocity field on a coarser level[1]. The flow scales that can be captured by this new coarser level of description are the *grid scales (GS)*, while the turbulent scales whose characteristic dimension is smaller than the smallest possible computed flow motion are the *subgrid scales (SGS)*.

With LES, the larger scales of the flow that are of great relevance in many physical systems involving the transport and mixing of momentum, heat and pollutants are directly represented in the simulations and the smaller scales which are believed to possess a more 'universal' character (subsection 1.1.2) are modelled by a *subgrid model*. As a consequence, one can in principle expect to obtain more reliable results from LES than from RANS procedures, for which the whole range of turbulent scales has to be modelled. Moreover, since in DNS a vast part of the computational effort is dedicated to solve the dissipative scales [14], LES presents a lower

[1] A computational mesh in LES is allways coarser than the one used for DNS.

computational cost when compared with DNS, extending the range of applicability to flows of higher Reynolds numbers.

Some of the disadvantages of LES are its demanding computational effort when compared to RANS methodologies and the simulation of flows where small scales are extremelly relevant, which is the case of flows in the surroundings of solid walls.

1.3 Homogeneous isotropic turbulence

When a turbulent flow is statistically invariant under rotations about arbitrary axes and, in consequence, statistically invariant under translations, we are in presence of a homogeneous and isotropic turbulent flow. From the previous characterization it is possible to infere that, for a homogeneous isotropic turbulent flow, the average velocity is zero. Although this concept corresponds to an idealized type of turbulent flow, it can be approximated by grid-generated turbulence in a wind tunnel, as reported on figure 1.5.

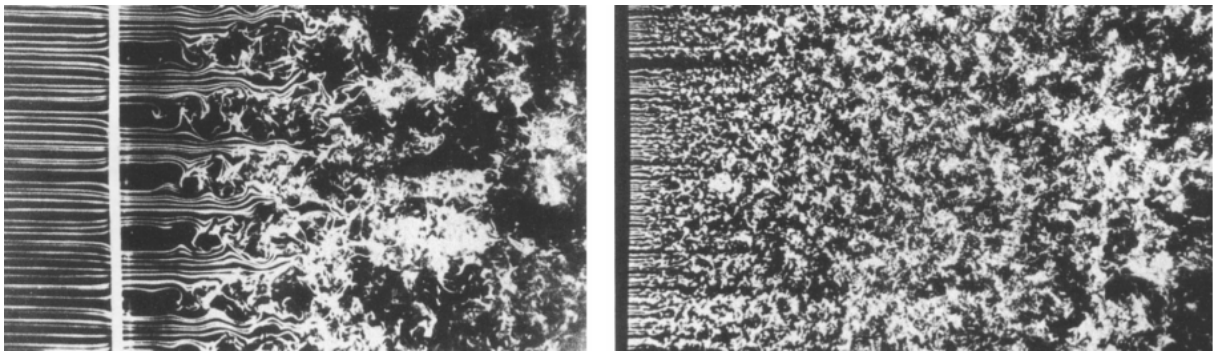

Figure 1.5: Turbulent flow past a grid. The left picture corresponds to the near field, while on the right we can observe the far field. Source: Tsinober [8].

Simulations of homogeneous isotropic turbulence Homogeneous isotropic turbulence is normally simulated using an unbounded cubical domain. This computational geometry is calculated assuming periodic boundary conditions in all three directions of the domain, an approach which enables the use of particularly efficient and fast numerical schemes, the pseudo-spectral methods. Because they are the simplest class of flows to study under numerical simulations and because they allow the use of pseudo-spectral methods, homogeneous isotropic turbulent flows are a popular case study in the numerical simulations frame of reference, allowing higher Reynolds number flow calculations.

Besides the fact that homogeneous turbulence can be computed in higher Reynolds number simulations, another important argument to study homogeneous isotropic turbulence is that it is the only type of flow where turbulent structures interact between themselves free from any external influences, as opposed with the remaining kinds of flows where the geometry of the problem also interacts with the turbulent field, affecting the shape of turbulent flow structures.

1.4 Objective of this work

The goal of this work is to analyse several models for the subgrid dissipation terms present in large eddy simulation models based on transport equations. The use of transport equations on subgrid models allows to incorporate some of the phenomenology of the small scales of motion that are not directly calculated, and thus are not explicitly represented, in large eddy simulations. Another advantage of SGS models based on transport equations is the possibility to bridge LES with RANS turbulenve models, enabling the computation of turbulent fluid flow in more complex scenarions.

A detailed study of the models for the subgrid-scale dissipation terms is hoped to provide the needed insight to understand their performance in LES or to help in the development of new models for these quantities.

1.5 Organization of the thesis

Following this introductory chapter on the basic issues regarding turbulence and its modelling, this thesis is outlined as follows:

Chapter 2 introduces the formalisms of large eddy simulations, including the filtering operation and the subgrid-scale models.

Chapter 3 describes the code employed to obtain the data bank by direct numerical simulations.

Chapter 4 explains how *a priori* tests are used to assess the models for the SGS dissipation terms along with the statisticall tools and spectral analysis.

Part II includes the paper published in the Journal of Turbulence: the discussion of the results from this work is included here, as well as the conclusions regarding the behaviour of the analysed models.

Chapter 2

Large eddy simulations

Reynolds-averaged Navier-Stokes simulations have been widely used and still remain the only option available to solve turbulent flows of engineering interest at high Reynolds numbers and with realistic geometries. However, and as the effect of turbulence is modelled, no one can expect to retrieve the instantaneous and chaotic behaviour of turbulent flows with RANS. No flow structures can be computed with RANS procedures. As a result, RANS simulations present serious limitations because those flow structures control much of the dynamics of turbulent flows.

Combustion flows provide an example where a better knowledge of the turbulent flow dynamics can strongly increase the accuracy of the simulations. In turbulent reacting flows the series of chain reactions which are part of the combustion process occur at a molecular level. As pointed out by Pitsch [15], there is a strong connection between the molecular diffusion responsible for the chemical reactions and the scalar variance which is related to the mixing of fuel and oxidizer on a macroscopic basis. Despite being more computationally expensive, large eddy simulations present better results in the prediction of the scalar variance when compared with RANS simulation techniques [15] and so LES is a more suitable alternative to compute turbulent reacting flows.

Modelling all turbulent scales in RANS is not straightforward. RANS models differ from one flow configuration to another and there is a constant need to tune the model in order to carry on with the simulation. On the other hand, models for the subgrid scales in LES are expected to be more universal as the range of modelled scales is smaller and theoretically more independent of the flow geometry (subsection 1.1.2).

While RANS does not attempt to resolve any turbulent flow structures, in direct numerical simulations all turbulent scales are computed. Because of a highly chaotic fluctuating velocity field, in turbulent flows there is a wide range of dinamically important scales that must be computed. This wide range of relevant scales spans from the integral scale l, characteristic of the largest coherent structures, to the Kolmogorov micro-scale η, standing for the smallest dissipative scales. In order to capture all the characteristic scales of a turbulent flow field with a proper resolution, the computational mesh must have a spacing factor of the order of the Kolmogorov scale, i.e. $\Delta x \sim \eta$.

Since the largest scales and the dissipative scales are related by $l/\eta = O\left(Re^{3/4}\right)$, where Re is based on the rms (root mean square) of the velocity fluctuation, $Re = u'' l/\nu$, a three-dimensional

simulation requires $O\left(Re^{9/4}\right)$ degrees of freedom [11]. In consequence, DNS simulations are restricted to flows at low to moderate Reynolds numbers, not being able to cope with the requirements of high Reynolds number flows.

As one can figure out, the computational effort for a DNS is larger than what nowadays high performance computers can endure and quickly escalates with the Reynolds number. Moreover, most of the computing power is targeted at resolving the dissipative scales [14]. If we still wish to capture the instantaneous flow structures of turbulent flows at higher Reynolds numbers and if we can neglect the importance of small scale features, the only option available resides in LES.

In this chapter, the mathematical formalisms related to large eddy simulations are introduced: the governing equations of turbulent flow (section 2.1) are subject to a filtering operation (section 2.2), and the unclosed terms arising by the filtering procedure have to be modelled by a subgrid model (section 2.3). This chapter ends with a description of subgrid models based on transport equations for the SGS kinetic energy, where three different approaches are presented to model the SGS dissipation terms (section 2.4).

2.1 Governing equations

Incompressible flows of Newtonian fluids are governed by the Navier-Stokes and continuity equations:

$$\frac{Du_i}{Dt} = \frac{\partial u_i}{\partial t} + \frac{\partial}{\partial x_j}\left(u_i u_j\right) = -\frac{\partial\left(p/\rho\right)}{\partial x_i} + \frac{\partial}{\partial x_j}\left(2\nu S_{ij}\right) \tag{2.1}$$

$$\frac{\partial u_i}{\partial x_i} = 0, \tag{2.2}$$

where ν is the kinematic viscosity of the fluid and $S_{ij} = \frac{1}{2}\left(\frac{\partial u_i}{\partial x_j} + \frac{\partial u_j}{\partial x_i}\right)$ is the strain-rate tensor.

Mixing rates of contaminants are dramatically enhanced under turbulent flow regimes. Scalar quantities are classified as active or passive depending on whether they influence the dynamics of turbulent flow fields or not, respectively. The transport of passive scalar fields is normally described by an advection-diffusion equation [7]:

$$\frac{D\theta}{Dt} = \frac{\partial\theta}{\partial t} + \frac{\partial}{\partial x_j}\left(\theta u_j\right) = \frac{\partial}{\partial x_j}\left(\alpha\frac{\partial\theta}{\partial x_j}\right), \tag{2.3}$$

where θ is a scalar quantity, smoke, dye or fuel concentration, for example, and α is the molecular diffusivity of θ.

An alternative and very popular perspective for isotropic turbulence is the analysis of turbulent flow motion in the Fourier space, as opposed with the analysis in physical space where the previous governing equations are built. By Fourier analysis, the turbulent flow motion can be interpreted as a sum of several motions, each one associated with a distinct wave number k. Many believe that the hierarchical description of different size eddies is better evidenced on Fourier space. The bridge between turbulent length scales and wave numbers is done by

associating a characteristic eddy lengthscale with the wavelength, $k = 2\pi/r$, where r is a scale for the eddy size.

Fourier space analysis is suited for flows with periodic boundary conditions. This presents no problem for isotropic flows as long as the size of the computational domain is sufficiently large when compared with the size of the largest computed flow structure.

The direct Fourier transform is used to describe a flow variable in the wave number domain. For a flow variable such as the velocity field, $\mathbf{u}(\mathbf{x}, t)$, the three-dimensional Fourier transform is given by:

$$\widehat{\mathbf{u}}(\mathbf{k}, t) = \left(\frac{1}{2\pi}\right)^3 \int_{-\infty}^{+\infty} \mathbf{u}(\mathbf{x}, t) e^{-\imath \mathbf{k}\cdot\mathbf{x}} d\mathbf{x}, \tag{2.4}$$

where $\widehat{\mathbf{u}}(\mathbf{k}, t)$ is the Fourier space representation of $\mathbf{u}(\mathbf{x}, t)$ and $\mathbf{k}$ is the wave number vector. Analogously, it is possible to retrieve the physical space description of a given flow variable from its spectral space representation through the inverse 3D Fourier transform:

$$\mathbf{u}(\mathbf{x}, t) = \int_{-\infty}^{+\infty} \widehat{\mathbf{u}}(\mathbf{k}, t) e^{\imath \mathbf{k}\cdot\mathbf{x}} d\mathbf{k}. \tag{2.5}$$

Within the flow equations context, some of the most interesting properties of the Fourier transform are:

1. Linearity:
$$\mathcal{F}_{\mathbf{k}}\{f(\mathbf{x}, t) + g(\mathbf{x}, t)\} = \widehat{f}(\mathbf{k}, t) + \widehat{g}(\mathbf{k}, t); \tag{2.6}$$

2. Derivative:
$$\mathcal{F}_{\mathbf{k}}\left\{\frac{\partial f}{\partial x_i}(\mathbf{x}, t)\right\} = \imath k_i \widehat{f}(\mathbf{k}, t); \tag{2.7}$$

3. Nonlinear terms:
$$\mathcal{F}_{\mathbf{k}}\{f(\mathbf{x}, t) g(\mathbf{x}, t)\} = \int_{\mathbf{k}=\mathbf{r}+\mathbf{s}} \widehat{f}(\mathbf{r}, t) \widehat{g}(\mathbf{k}-\mathbf{r}, t) d\mathbf{r}; \tag{2.8}$$

where $f(\mathbf{x}, t)$ and $g(\mathbf{x}, t)$ are two variables in the physical space, $\widehat{f}(\mathbf{k}, t)$ and $\widehat{g}(\mathbf{k}, t)$ are their equivalent in the spectral space, $\mathcal{F}_{\mathbf{k}}\{\ \}$ is an operator describing the Fourier transform and $\mathbf{k}$, $\mathbf{r}$ and $\mathbf{s}$ are wave number vectors. (2.7) is probably the most interesting property since it reflects the ability of the Fourier transform to convert linear ordinary differential equations into linear algebraic equations.

Incompressible flows of Newtonian fluids are governed by equations (2.1) and (2.2). The application of the Fourier transform to equations (2.1) and (2.2) yields to:

$$\left(\frac{d}{dt} + \nu k^2\right) \widehat{u}_i(\mathbf{k}, t) = -\imath k_i \widehat{p}(\mathbf{k}, t) - \imath k_j \int_{\mathbf{k}=\mathbf{r}+\mathbf{s}} \widehat{u}_i(\mathbf{r}, t) \widehat{u}_j(\mathbf{k}-\mathbf{r}, t) d\mathbf{r}, \tag{2.9}$$

$$\imath k_i \widehat{u}_i(\mathbf{k}, t) = 0, \tag{2.10}$$

where $k = |\mathbf{k}|$ is the wave number norm, $\imath$ is the imaginary unit and $\widehat{p}(\mathbf{k}, t) = \mathcal{F}_{\mathbf{k}}\left\{\frac{p(\mathbf{x}, t)}{\rho}\right\}$ for convenience. The local acceleration and viscous terms are represented on the left-hand

side of equation (2.9), while on the right-hand side we have the pressure and nonlinear terms. Multiplying (2.9) by $\imath k_i$ yields to an evolution equation for the pressure field:

$$\widehat{p}(\mathbf{k},t) = -\frac{k_i k_j}{k^2} \int_{\mathbf{k}=\mathbf{r}+\mathbf{s}} \widehat{u}_i(\mathbf{r},t)\widehat{u}_j(\mathbf{k}-\mathbf{r},t)d\mathbf{r}. \tag{2.11}$$

Replacing the pressure term in (2.9) by (2.11), the governing equation for the velocity field in wave number space becomes:

$$\left(\frac{d}{dt} + \nu k^2\right) \widehat{u}_i(\mathbf{k},t) = -P_{ij} \left(\imath k_k \int_{\mathbf{k}=\mathbf{r}+\mathbf{s}} \widehat{u}_j(\mathbf{r},t)\widehat{u}_k(\mathbf{k}-\mathbf{r},t)d\mathbf{r}\right), \tag{2.12}$$

in which P_{ij} is a projection tensor defined by [14]:

$$P_{ij} = \left(\delta_{ij} - \frac{k_i k_j}{k^2}\right).$$

The advection-diffusion equations in Fourier space are obtained in a similar way as (2.9). In the wave number domain, (2.3) become:

$$\left(\frac{d}{dt} + \alpha k^2\right) \widehat{\theta}(\mathbf{k},t) = -\imath k_j \int_{\mathbf{k}=\mathbf{r}+\mathbf{s}} \widehat{\theta}(\mathbf{r},t)\widehat{u}_j(\mathbf{k}-\mathbf{r},t)d\mathbf{r}. \tag{2.13}$$

2.2 Filtered equations

This section introduces the equations used in large eddy simulations. The fluid flow governing equations are subject to a filtering procedure in order to present fewer degrees of freedom and hence reduce the computational cost associated with the simulation of a turbulent flow. In the LES framework, the filtering operation is usually related to a convolution product. Subsection 2.2.1 presents the filtering operation and the most relevant properties concerned with the filters employed in large eddy simulations. The filter used in the present work in *a priori* tests is introduced in subsection 2.2.1 and the following subsection describes how the filtered equations are obtained from the governing equations and identifies a new term which needs to be addressed by a turbulence model in order to carry out a large eddy simulation.

2.2.1 The filtering procedure

In order to relief the computational effort found in direct numerical simulations of turbulent flows, large eddy simulations resort to a spatial filtering technique. This filtering approach is based on a low-pass filter in the frequency or wave number domain, or a high-pass filter on a length scale domain, and it establishes which turbulent scales are to be resolved and which ones are not. Turbulent scales larger than a characteristic length scale defined by the filter cutoff, the lower frequency motions, are directly computed.

Figure 2.1 illustrates how the filtering operation reduces the number of degrees of freedom in a large eddy simulation. As it is possible to observe, to obtain a reliable reproduction of the original and the filtered signal, the mesh resolution requirements are very different. Filtering a

turbulent flow variable allows it to be represented on a coarser level, lowering the computational cost associated with its calculation.

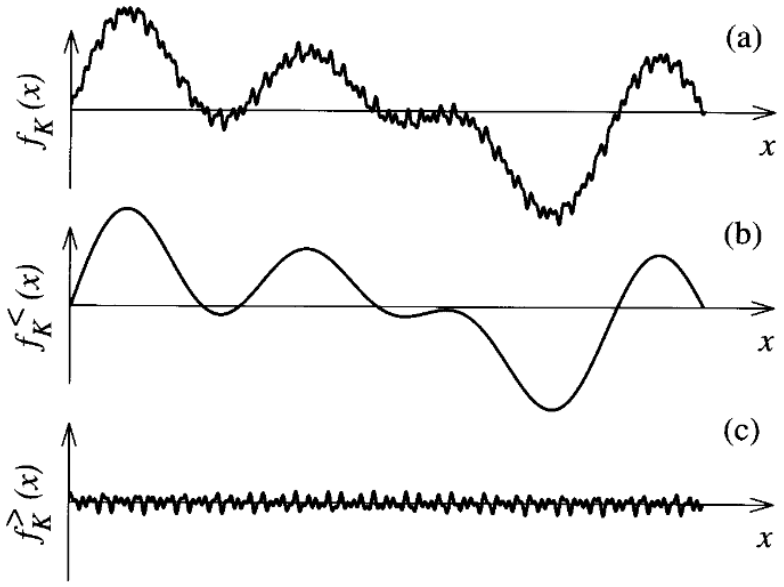

Figure 2.1: (a): Turbulent flow signal $f_K(x)$; (b) filtered signal $f_K^<(x)$ obtained by low-pass filtering in the frequency domain; (c) signal subjected to a high-pass filter $f_K^>(x)$. From Frisch [10].

Mathematically, a spatial filtering procedure can be defined by a convolution product [11]:

$$\overline{u}_i(\mathbf{x}) = \int_{-\infty}^{+\infty} u_i(\boldsymbol{\xi})\, G(\mathbf{x}-\boldsymbol{\xi})\, d^3\boldsymbol{\xi}, \tag{2.14}$$

where $\overline{u}_i$ is the filtered or resolved part of the i-th component of the velocity field and G is the convolution kernel. The unresolved part of u_i, also known as the subgrid part of u_i, u_i', can be recovered by:

$$u_i'(\mathbf{x}) = u_i(\mathbf{x}) - \overline{u}_i(\mathbf{x})$$

In the case of homogeneous isotropic turbulence, the filter used in large eddy simulations is an isotropic filter. This filter has to verify the following properties [11]:

1. Conservation of constants:

$$\overline{a} = a \quad \Leftrightarrow \quad \int_{-\infty}^{+\infty} G(\boldsymbol{\xi})\, d^3\boldsymbol{\xi} = 1;$$

2. Linearity:

$$\overline{u_i + u_j} = \overline{u}_i + \overline{u}_j;$$

3. Commutation with derivation:

$$\overline{\frac{\partial u_i}{\partial s}} = \frac{\partial \overline{u}_i}{\partial s}, \quad s = \mathbf{x}, t.$$

Generally, the spatial filters used in LES do not verify other properties belonging to so-called Reynolds operators, that is, the filtering technique defined by (2.14) usually verifies:

- $\overline{\overline{u}}_i \neq \overline{u}_i$;
- $\overline{u_i'} \neq 0$.

Different filters can be used in large eddy simulations. A description of some of the most popular filters employed in LES can be found in [14] and [11]. Here only the filter used in *a priori* tests will be characterised: the *box filter*. For the unidimensional case, the convolution kernel of a box filter is given by:

$$G(x - \xi) = \begin{cases} \frac{1}{\Delta} & \text{if } |x - \xi| \leqslant \frac{\Delta}{2}, \\ 0 & \text{otherwise.} \end{cases} \tag{2.15}$$

Figure 2.2 shows the graphical representation of the box filter.

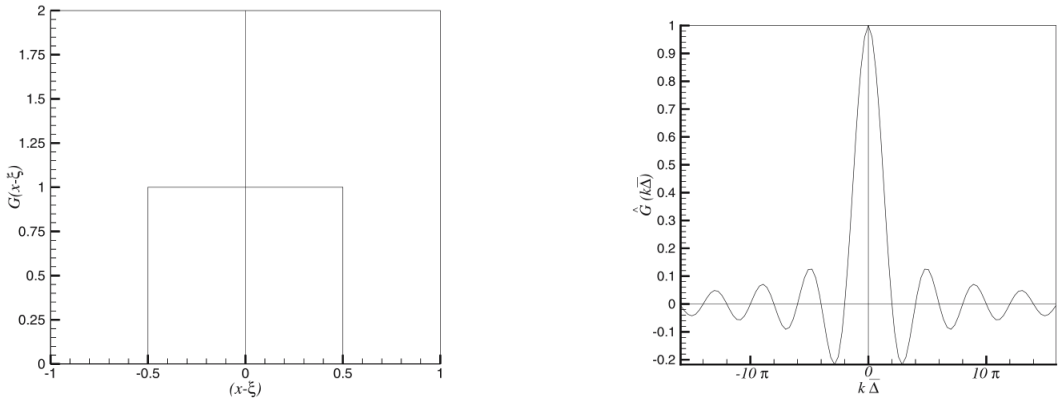

(a) (b)

Figure 2.2: Box filter: representation on physical space (a) and on the frequency domain (b). From Sagaut [11].

2.2.2 Application to the flow equations

Given the filter properties in 2.2.1, it is now possible to deduce the filtered equations solved in LES. The filtered equations come from the application of an isotropic filter to the flow's governing equations, the continuity and the Navier-Stokes equations. Application of an isotropic filter to

the momentum and continuity equations (2.1) and (2.2) yields to:

$$\frac{\partial \overline{u}_i}{\partial t} + \frac{\partial}{\partial x_j}\left(\overline{u_i u_j}\right) = -\frac{\partial\left(\overline{p}/\rho\right)}{\partial x_i} + \frac{\partial}{\partial x_j}\left(2\nu\overline{S}_{ij}\right) \tag{2.16}$$

$$\frac{\partial \overline{u}_i}{\partial x_i} = 0. \tag{2.17}$$

For the passive scalar case, equation (2.3) becomes:

$$\frac{\partial \overline{\theta}}{\partial t} + \frac{\partial}{\partial x_j}\left(\overline{\theta u_j}\right) = \frac{\partial}{\partial x_j}\left(\alpha\frac{\partial \overline{\theta}}{\partial x_j}\right). \tag{2.18}$$

The non-linear terms in the filtered momentum (2.16) and advection-diffusion (2.18) equations can be written according to a Leonard's triple decomposition [11, 16]:

$$\begin{aligned}\overline{u_i u_j} &= \overline{\left(\overline{u}_i + u_i'\right)\left(\overline{u}_j + u_j'\right)} \\ &= \overline{\overline{u}_i\overline{u}_j} + \overline{\overline{u}_i u_j'} + \overline{u_i'\overline{u}_j} + \overline{u_i' u_j'}.\end{aligned}$$

$$\begin{aligned}\overline{\theta u_j} &= \overline{\left(\overline{\theta} + \theta'\right)\left(\overline{u}_j + u_j'\right)} \\ &= \overline{\overline{\theta}\overline{u}_j} + \overline{\overline{\theta} u_j'} + \overline{\theta'\overline{u}_j} + \overline{\theta' u_j'}.\end{aligned}$$

Equations (2.16) and (2.18) can now be expressed as:

$$\frac{\partial \overline{u}_i}{\partial t} + \frac{\partial}{\partial x_j}\left(\overline{u}_i\overline{u}_j\right) = -\frac{\partial\left(\overline{p}/\rho\right)}{\partial x_i} + \frac{\partial}{\partial x_j}\left(2\nu\overline{S}_{ij}\right) - \frac{\partial \tau_{ij}}{\partial x_j} \tag{2.19}$$

$$\frac{\partial \overline{\theta}}{\partial t} + \frac{\partial}{\partial x_j}\left(\overline{\theta}\overline{u}_j\right) = \frac{\partial}{\partial x_j}\left(\alpha\frac{\partial \overline{\theta}}{\partial x_j}\right) - \frac{\partial \tau_j^{(\theta)}}{\partial x_j}. \tag{2.20}$$

Comparing equations (2.1) and (2.3) with (2.19) and (2.20), it is possible to assess that the implementation of a filtering operation produces additional terms, the *subgrid tensors* τ_{ij} and $\tau_j^{(\theta)}$. According to the Leonard's decomposition,

$$\begin{aligned}\tau_{ij} &= \overline{u_i u_j} - \overline{u}_i\overline{u}_j \\ &= \underbrace{\overline{\overline{u}_i\overline{u}_j} - \overline{u}_i\overline{u}_j}_{L_{ij}} + \underbrace{\overline{\overline{u}_i u_j'} + \overline{u_i'\overline{u}_j}}_{C_{ij}} + \underbrace{\overline{u_i' u_j'}}_{R_{ij}},\end{aligned} \tag{2.21}$$

$$\begin{aligned}\tau_j^{(\theta)} &= \overline{\theta u_j} - \overline{\theta}\overline{u}_j \\ &= \underbrace{\overline{\overline{\theta}\overline{u}_j} - \overline{\theta}\overline{u}_j}_{L_j^{(\theta)}} + \underbrace{\overline{\overline{\theta} u_j'} + \overline{\theta'\overline{u}_j}}_{C_j^{(\theta)}} + \underbrace{\overline{\theta' u_j'}}_{R_j^{(\theta)}},\end{aligned} \tag{2.22}$$

the subgrid tensors are the sum of three tensors: the Leonard tensors L_{ij} and $L_j^{(\theta)}$, the cross-stress tensors C_{ij} and $C_j^{(\theta)}$ and the Reynolds subgrid tensors R_{ij} and $R_j^{(\theta)}$. The Leonard tensors relate to interactions between the large resolved scales, while the cross-stress tensors account

for interactions between resolved and subgrid scales, and the Reynolds subgrid tensors describe the interactions among the small subgrid scales of motion.

Equations (2.19) and (2.20) reveal that the description of the large scale dynamics of turbulence is only complete if there is some information regarding the subgrid scales of motion. Such information is accounted by the subgrid tensors τ_{ij} and $\tau_j^{(\theta)}$ and, since the subgrid quantities involved in the definition of τ_{ij} and $\tau_j^{(\theta)}$ are not available in a large eddy simulation, this term has to be modelled to enable the large scales computation. Modelling closures for equations (2.19) and (2.20) are discussed on section 2.3.

2.3 Subgrid-scale models

The eddy viscosity concept dates back to 1877 when French mathematician and physicist Joseph Boussinesq related the effect of turbulence to an additional source of stress similar to the viscous stress caused by molecular viscosity. This concept applies straightforwardly to the time-averaged Navier-Stokes equations defined in the framework of RANS models since they are based on a decomposition of the turbulent flow into a mean and fluctuating fields, in which the fluctuating field accounts for the global effects of turbulence. Extension of the Boussinesq hypothesis to the subgrid-scale models results in:

$$\tau_{ij} - \frac{1}{3}\tau_{kk}\delta_{ij} = -2\nu_{sgs}\overline{S}_{ij}, \tag{2.23}$$

$$\tau_j^{(\theta)} = -\alpha_{sgs}\frac{\partial\overline{\theta}}{\partial x_j}. \tag{2.24}$$

SGS models based on Boussinesq's postulates are known as **eddy viscosity models**. The eddy viscosity and diffusivity assumptions defined by (2.23) and (2.24) translate the filtered equations (2.19) and (2.20) to:

$$\frac{\partial\overline{u}_i}{\partial t} + \frac{\partial}{\partial x_j}\left(\overline{u}_i\overline{u}_j\right) = -\frac{\partial\left(\overline{p}^{\dagger}/\rho\right)}{\partial x_i} + \frac{\partial}{\partial x_j}\left(2\left(\nu+\nu_{sgs}\right)\overline{S}_{ij}\right), \tag{2.25}$$

$$\frac{\partial\overline{\theta}}{\partial t} + \frac{\partial}{\partial x_j}\left(\overline{\theta}\overline{u}_j\right) = \frac{\partial}{\partial x_j}\left(\left(\alpha+\alpha_{sgs}\right)\frac{\partial\overline{\theta}}{\partial x_j}\right), \tag{2.26}$$

where $\overline{p}^{\dagger}$ is a modified pressure, $\overline{p}^{\dagger} = \overline{p} + \frac{1}{3}\rho\tau_{kk}$. The set of equations specified above remains unclosed since the problem of establishing a closure model for τ_{ij} and $\tau_j^{(\theta)}$ has now been replaced by the problem of prescribing a model for ν_{sgs} and α_{sgs}.

The spectral analogue of (2.25) and (2.26) introduces the definition of the spectral eddy viscosity and diffusivity coefficients. The analysis in Fourier space is based on a sharp cutoff filter designed to eliminate all wave numbers larger than the cutoff wave number $k_c = \pi/\Delta$. In

wave number space, equations (2.25) and (2.26) are replaced by:

$$\left(\frac{d}{dt}+\left(\nu+\nu_{sgs}\left(\mathbf{k}|k_c\right)\right)k^2\right)\widehat{u}_i\left(\mathbf{k},t\right)=-P_{ij}\left(\imath k_k\int_{\mathbf{k}=\mathbf{r}+\mathbf{s}}^{r,s<k_c}\widehat{u}_j\left(\mathbf{r},t\right)\widehat{u}_k\left(\mathbf{k}-\mathbf{r},t\right)d\mathbf{r}\right), \quad (2.27)$$

$$\left(\frac{d}{dt}+\left(\alpha+\alpha_{sgs}\left(\mathbf{k}|k_c\right)\right)k^2\right)\widehat{\theta}\left(\mathbf{k},t\right)=-\imath k_j\int_{\mathbf{k}=\mathbf{r}+\mathbf{s}}^{r,s<k_c}\widehat{\theta}\left(\mathbf{r},t\right)\widehat{u}_j\left(\mathbf{k}-\mathbf{r},t\right)d\mathbf{r}, \quad (2.28)$$

and the spectral eddy viscosity and diffusivity coefficients are expressed by:

$$\nu_{sgs}\left(\mathbf{k}|k_c\right)k^2\widehat{u}_i\left(\mathbf{k},t\right)=P_{ij}\left(\imath k_k\int_{\mathbf{k}=\mathbf{r}+\mathbf{s}}^{r\text{ or }s>k_c}\widehat{u}_j\left(\mathbf{r},t\right)\widehat{u}_k\left(\mathbf{k}-\mathbf{r},t\right)d\mathbf{r}\right),$$

$$\alpha_{sgs}\left(\mathbf{k}|k_c\right)k^2\widehat{\theta}\left(\mathbf{k},t\right)=\imath k_j\int_{\mathbf{k}=\mathbf{r}+\mathbf{s}}^{r\text{ or }s>k_c}\widehat{\theta}\left(\mathbf{r},t\right)\widehat{u}_j\left(\mathbf{k}-\mathbf{r},t\right)d\mathbf{r}.$$

In 1925, Prandtl suggested the first closure method for eddy viscosity models, the **mixing length model**. The mixing length model is based on the kinetic energy theory of gases, in which the kinematic viscosity of a fluid is proportional to a mean-free path length of the molecules and their rms speed [7]: $\nu \propto lV$. According to Prandtl, the eddy viscosity is related to a characteristic length and velocity scales, where the length scale is referred to as a mixing length. In large eddy simulations, Prandtl's mixing length hypothesis consists in estimating ν_{sgs} by:

$$\nu_{sgs}(\mathbf{x},t)=u^*(\mathbf{x},t)l^*(\mathbf{x},t), \quad (2.29)$$

where $u^*(\mathbf{x},t)$ is a characteristic velocity describing the speed of the SGS motions and $l^*(\mathbf{x},t)$ is the length scale usually taken as $C\Delta$, where C is a model constant and Δ is the length scale associated with the cutoff of the filter employed.

The role of subgrid models consists in establishing a relationship between the unresolved motions and the resolved scales of turbulence, that is, to provide a mathematical description for the subgrid tensors τ_{ij} and $\tau_j^{(\theta)}$ or for the eddy viscosity and diffusivity coefficients ν_{sgs} and α_{sgs}. These quantities are intrinsically connected to subgrid-scale motions but they have to be parametrized in terms of known variables accessible during LES. In large eddy simulations, a popular choice to bridge the subgrid and grid-scale motions resides in invoking the **local equilibrium assumption**. The local equilibrium assumption supposes that, at the small scales level and for statistically homogeneous turbulence, all the energy arriving from the large scales is instantaneously dissipated by molecular viscosity. Mathematically, the local equilibrium assumption translates into [11]:

$$\underbrace{-\tau_{ij}\overline{S}_{ij}}_{P}=\underbrace{\nu\left(\overline{\frac{\partial u_i}{\partial x_j}\frac{\partial u_i}{\partial x_j}}-\frac{\partial\overline{u}_i}{\partial x_j}\frac{\partial\overline{u}_i}{\partial x_j}\right)}_{\Sigma}, \quad (2.30)$$

where P represents the energy transfer from GS to SGS motions and Σ is the viscous dissipation of the kinetic energy associated with the subgrid scales.

The **Smagorinsky model** (1963) is an eddy viscosity model based upon the local equilib-

rium assumption and on the dissipation law. The dissipation law approximates the dissipation rate of the turbulent kinetic energy, ε, by:

$$\varepsilon \sim \frac{u^3}{l}, \tag{2.31}$$

where u and l are characteristic velocity and length scales of turbulence. In the Smagorinsky model, the characteristic scales are estimated by $u \sim l|\overline{S}|$ and $l \sim \Delta$, in which $|\overline{S}| = \sqrt{2\overline{S}_{ij}\overline{S}_{ij}}$ is the magnitude of the GS strain-rate tensor and Δ is the filter width used in LES. If term Σ on the local equilibrium law (2.30) is replaced by (2.31) and the Boussinesq hypothesis (2.23) is employed to characterize τ_{ij} on term P, the Smagorinsky model for ν_{sgs} can be given by:

$$\nu_{sgs} = (C_S\Delta)^2 |\overline{S}|, \tag{2.32}$$

where C_S is the model constant. An estimate for C_S can be obtained considering the case of homogeneous isotropic turbulence, a filter cutoff in the inertial range of the Kolmogorov kinetic energy spectrum, $E(k) = C_K\varepsilon^{2/3}k^{-5/3}$, and a equilibrium hypothesis, $P = \varepsilon$:

$$C_S \simeq \frac{1}{\pi}\left(\frac{2}{3C_K}\right)^{3/4} = 0.18, \tag{2.33}$$

in which C_K is the Kolmogorov constant. In practical calculations, C_S is flow-dependent [11].

A procedure to improve the computation of the Smagorinsky model constant C_S has been proposed by Germano *et al.* (1991). The **dynamic Smagorinsky approach** consists in adjusting the value of the Smagorinsky model constant C_S locally at each point in space and time. The dynamic algorithm can and has been extended to other modelling strategies involving model constants, but here the dynamic technique will be presented only for the Smagorinsky model.

The dynamic approach involves an additional filtering stage with a filter width larger than the filter employed in LES. This new filtering level is accomplished by the use of a "test filter" characterized by $\widetilde{\Delta} = m\Delta$ and $m > 1$, where m is usually taken as 2. Within the two filtering levels presented, one associated with the LES filter and another related to the test filter, two SGS tensors can be defined: $\tau_{ij} = \overline{u_i u_j} - \overline{u}_i\overline{u}_j$ and $T_{ij} = \widetilde{\overline{u_i u_j}} - \widetilde{\overline{u}}_i\widetilde{\overline{u}}_j$, respectively. The dynamic algorithm now makes use of an expression known as *Germano identity* given by:

$$\begin{aligned} L_{ij} &= T_{ij} - \widetilde{\tau}_{ij} \\ &= \widetilde{\overline{u_i u_j}} - \widetilde{\overline{u}}_i\widetilde{\overline{u}}_j. \end{aligned} \tag{2.34}$$

In (2.34), L_{ij} can be fully computed by applying a test filter to the resolved quantities from the LES velocity field, while both terms on the right-hand side of (2.34), T_{ij} and $\widetilde{\tau}_{ij}$, have to be

modelled. Supposing that they are both modelled by the Smagorinsky model:

$$\tau_{ij} - \frac{1}{3}\tau_{kk}\delta_{ij} = C_d\beta_{ij} = C_d\left(-2\Delta^2|\overline{S}|\overline{S}_{ij}\right),$$
$$T_{ij} - \frac{1}{3}T_{kk}\delta_{ij} = C_d\alpha_{ij} = C_d\left(-2\widetilde{\Delta}^2|\widetilde{\overline{S}}|\widetilde{\overline{S}}_{ij}\right),$$

in which $C_d = C_S^2$. The Germano identity, (2.34), can now be expressed by:

$$L_{ij} - \frac{1}{3}L_{kk}\delta_{ij} = C_d\alpha_{ij} - \widetilde{C_d\beta_{ij}}. \tag{2.35}$$

Assuming that C_d is constant over the interval determined by the test filter, $\widetilde{\Delta}$, it is possible to approximate the last term on the right-hand side of (2.35) by:

$$\widetilde{C_d\beta_{ij}} = C_d\widetilde{\beta}_{ij}. \tag{2.36}$$

Now C_d can be computed by a least-squares method suggested by Lilly (1992):

$$\frac{\partial E_{ij}E_{ij}}{\partial C_d} = 0,$$

where E_{ij} is the residual of (2.34) with the approximation (2.36):

$$E_{ij} = L_{ij} - \frac{1}{3}L_{kk}\delta_{ij} - C_d\alpha_{ij} + C_d\widetilde{\beta}_{ij}.$$

Another proposal to model the subgrid-scale stresses comes from Métais and Lesieur and their **structure function model** [17] which translates Kraichnan's eddy viscosity [18] defined on the wave number space into the physical space. Like the Smagorinsky model, the spectral eddy viscosity is based upon the eddy viscosity assumption and invokes the equilibrium hypothesis, but, as one shall see, Kraichnan's eddy viscosity is physically more consistent than the Smagorinsky model as it cancels out whenever the flow is well resolved, that is, whenever the simulation is a direct numerical simulation or the flow is laminar instead of turbulent.

In Fourier space, the total kinetic energy is expressed by:

$$\frac{1}{2}\sum_{\mathbf{k}}\widehat{u}_i(\mathbf{k},t)\,\widehat{u}_i^*(\mathbf{k},t) = \int_0^\infty E(k,t)\,dk,$$

where $\widehat{u}_i^*$ is the complex conjugate of $\widehat{u}_i$ and $E(k,t)$ is the kinetic energy spectrum. The evolution equation for $E(k,t)$ is:

$$\left(\frac{d}{dt} + 2\nu k^2\right)E(k,t) = T(k,t),$$

in which $T(k,t)$ is the energy transfer function representing the energy removal from large scales (small k) and the energy deposition at small scales (large k). [7]. A representation of $T(k)$ is illustrated on figure 2.3. $T(k)$ is negative for small k and positive for larger k. This is because, during the energy transfer process, turbulent scales associated with small wave numbers are

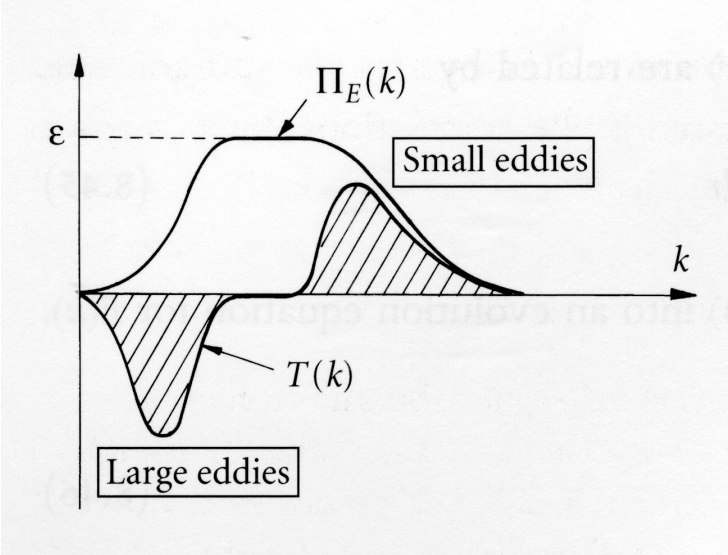

Figure 2.3: Energy transfer function in wave number space. Source: Davidson [7].

losing energy to smaller scales represented by larger wave numbers. Overall,

$$\int_0^\infty T(k)\,dk = 0.$$

The net rate of transfer of energy from scales with wave numbers smaller than k to all scales related to wave numbers greater than k is:

$$\Pi(k) = \int_k^\infty T(k)\,dk = -\int_0^k T(k)\,dk,$$

which is always positive since the net energy flux aims towards the small scales.

A spectral cutoff filter can be used to distinguish between the large flow scales, $k < k_C$, and the small scales $k > k_C$, where k_C is the cutoff associated with the filter. The spectral eddy viscosity is intended to describe the action resulting from the interactions between grid and subgrid-scales on the resolved, large flow scales. Kraichnan proposes:

$$\nu_{sgs}(k|k_C) = \frac{-T(k|k_C)}{2k^2E(k)}, \qquad k < k_C,$$

where $T(k|k_C)$ is the contribution to $T(k)$ from interactions between $k < k_C$ and other scales associated with wave numbers greater than k_C. $T(k|k_C)$ obeys a detailed conservation property [18] and thus:

$$\Pi(k_C) = -\int_0^{k_C} T(k|k_C)\,dk.$$

Assuming that k_C lies in the inertial range of an energy spectrum shaped according to Kolmogorov's law, $E(k) = C_K\varepsilon^{2/3}k^{-5/3}$, and invoking the equilibrium hypothesis $\Pi(k_C) = \varepsilon$, the

spectral eddy viscosity can be obtained through:

$$\int_0^{k_C} 2\nu_{sgs}\left(k|k_C\right) k^2 E\left(k\right) dk = \varepsilon,$$

whereby:

$$\nu_{sgs}\left(k|k_C\right) = \frac{2}{3} C_K^{-3/2} \sqrt{\frac{E\left(k_C\right)}{k_C}}. \tag{2.37}$$

The spectral eddy viscosity cancels out whenever the energy at cutoff is zero, yielding to a direct numerical simulation whenever the grid resolution is fine enough to capture all relevant turbulent scales.

So, how to translate the spectral eddy viscosity concept into physical space? Métais and Lesieur [17] suggested to use Batchelor's relation built for homogeneous flows [19] which relates the kinetic energy spectrum $E\left(k,t\right)$ to a second order structure function $F_2\left(\mathbf{x},\Delta,t\right)$ by:

$$\begin{aligned} F_2\left(\mathbf{x},\Delta,t\right) &= \langle \| \mathbf{u}\left(\mathbf{x}+\mathbf{r},t\right) - \mathbf{u}\left(\mathbf{x},t\right) \|^2 \rangle_{\|\mathbf{r}\|=\Delta} \\ &= 4\int_0^{\infty} E\left(k,t\right)\left(1-\frac{\sin\left(k\Delta\right)}{k\Delta}\right) dk. \end{aligned} \tag{2.38}$$

In large eddy simulations there is only access to filtered field variables and so the previous relationship (2.38) is written in terms of a filtered 2^{nd} order structure function, $\overline{F}_2\left(\mathbf{x},\Delta,t\right)$:

$$\begin{aligned} \overline{F}_2\left(\mathbf{x},\Delta,t\right) &= \langle \| \overline{\mathbf{u}}\left(\mathbf{x}+\mathbf{r},t\right) - \overline{\mathbf{u}}\left(\mathbf{x},t\right) \|^2 \rangle_{\|\mathbf{r}\|=\Delta} \\ &= 4\int_0^{k_C} E\left(k,t\right)\left(1-\frac{\sin\left(k\Delta\right)}{k\Delta}\right) dk. \end{aligned} \tag{2.39}$$

Assuming once again an inertial range Kolmogorov spectrum, $\nu_{sgs}\left(k|k_C\right)$ defined in (2.37) translates to:

$$\nu^{SF}\left(\mathbf{x},\Delta,t\right) = 0.105 C_K^{-3/2} \Delta \sqrt{\overline{F}_2\left(\mathbf{x},\Delta,t\right)}. \tag{2.40}$$

$\overline{F}_2\left(\mathbf{x},\Delta,t\right)$ is computed by a local statistical average involving the squares of the filtered velocity differences between $\mathbf{x}$ and the six closest points on the computational grid [16].

The models presented above rely on the local equilibrium assumption of the subgrid scales of motion. The problem is that this hypothesis fails even in homogeneous isotropic flows as found out by Borue and Orzag [20] and da Silva and Métais [21], the local imbalance increasing with Reynolds number and filter size [22]. This is particularly relevant for most of the flows found in Nature or in the engineering context where the Reynolds number is generally large and large eddy simulations must necessarily use coarser computational meshes.

Another flawed hypothesis that has been and still is used to develop subgrid-scale models is Boussinesq's eddy-viscosity. The approximation between the viscous stress originated by molecular viscosity and the SGS tensor accounting for the action resulting from interactions between larger and smaller motions of turbulence on the resolved scales is rather unphysical [14]. Non-local history effects are known to be an important part of the physics of turbulence and they are not represented on the simple and local relationship proposed by Boussinesq.

One subgrid-scale model that does not depend on the eddy viscosity hypothesis nor on the local equilibrium assumption is the **scale-similarity model**. Bardina *et al.* (1980) [23] proposed an alternative scale-similarity subgrid-scale model to discard the eddy viscosity assumption since it has been found that there is a poor correlation between the SGS stress and the large-scale strain rate tensors, τ_{ij} and $\overline{S}_{ij}$, respectively. The scale-similarity concept introduced by Bardina *et al.* assumes that the most important interactions between the grid and subgrid-scales occur between the smallest grid scales and the largest subgrid-scales. They resort to a double filtering procedure analogous to the one employed on the dynamic approaches presented above, only this time the second filtering operation applies a filter with the same filter width as the original filtering procedure used to separate scales in large eddy simulations. The resolved or grid scale part of a turbulent flow variable can now be described by:

$$\overline{u}_i = \overline{\overline{u}}_i + \overline{u}'_i. \tag{2.41}$$

The Leonard tensor in the definition of τ_{ij}, equation (2.21), is already written in terms of resolved quantities available during a large eddy simulation, but the cross-stress and Reynolds subgrid-stress tensors are not. Rewritting C_{ij} and R_{ij} as functions of the large and small scale parts of $\overline{u}_i$ according the additional filtering level expressed on (2.41):

$$\begin{aligned} C_{ij} &= \overline{\overline{u}}_i \left(\overline{u}_j - \overline{\overline{u}}_j\right) + \overline{\overline{u}}_j \left(\overline{u}_i - \overline{\overline{u}}_i\right) \\ R_{ij} &= \left(\overline{u}_i - \overline{\overline{u}}_i\right)\left(\overline{u}_j - \overline{\overline{u}}_j\right) \end{aligned}$$

$$C_{ij} + R_{ij} = \overline{u}_i\overline{u}_j - \overline{\overline{u}}_i\overline{\overline{u}}_j \tag{2.42}$$

The modelled SGS tensor is obtained by the sum of the Leonard tensor L_{ij} to (2.42):

$$\tau_{ij}^{SS} = \overline{\overline{u}_i\overline{u}_j} - \overline{\overline{u}}_i\overline{\overline{u}}_j. \tag{2.43}$$

As one can acknowledge, the scale-similarity model presented by (2.42) resembles the Germano identity expressed on (2.34).

The real and modelled subgrid-scale tensors, τ_{ij} and τ_{ij}^{SS}, are found to be very well correlated and the scale-similarity model can predict backscatter. However, this model does not dissipate enough energy and in practical computations the scale-similarity model is coupled with a more dissipative model, such as the Smagorinsky model, to ensure proper levels of dissipation, yielding to the well known **mixed-scale similarity models**:

$$\tau_{ij}^{model} = \tau_{ij}^{SS} + \tau_{ij}^{Smagor}.$$

Subgrid models described before belong to a class of **algebraic** or **zero-equation models**, since they do not require any additional transport equations to be solved besides the governing equations of fluid flow. More complex SGS models relying on the solution of n additional differential equations have been developed. The introduction of additional transport equations in the definition of SGS models allows to integrate non-local and history effects of the flow, and

so, the increased computational cost of n-equation models is expected to be rewarded by a more realistic description of turbulent SGS stresses.

Following the suggestion of Kolmogorov and Prandtl made in the 1940s, **one-equation models** introduce a transport equation for the subgrid-scale kinetic energy in order to provide a better estimate for the velocity length scale in the definition of the SGS eddy viscosity coefficient (2.29). In large-eddy simulations, one-equation models based on the transport of the SGS kinetic energy have been developed independently by different authors, including Schumann [1], Schmidt and Schumann [24], Yoshizawa [2], and Yoshizawa and Horiuti [25]. For these models, the subgrid viscosity is formulated by:

$$\nu_{sgs}(\mathbf{x},t) = C_m \Delta \sqrt{q^2_{sgs}(\mathbf{x},t)},$$

in which C_m is the model constant and $q^2_{sgs}(\mathbf{x},t)$ is the filtered subgrid kinetic energy, $q^2_{sgs}(\mathbf{x},t) = \frac{1}{2}\overline{(u_i(\mathbf{x},t) - \overline{u}_i(\mathbf{x},t))}$. The filtered subgrid kinetic energy is computed by an additional evolution equation presented on section 2.4. Apart from allowing to incorporate non-local effects into the definition of the eddy viscosity, which means that the eddy viscosity is influenced by the history of the flow, one-equation models based on the transport of the subgrid-scale kinetic energy do not use the local equlibrium assumption, as the SGS motions are characterised by a velocity scale directly related to them. As pointed out by Kajishima and Nomachi [26], another important advantage of one-equation models based on the SGS kinetic energy is that q^2_{sgs} cancels out in nonturbulent regions and on solid walls.

Differential subgrid stress models adopt a different perspective to estimate the SGS tensor. An evolution equation is solved for each component of the subgrid-scale tensor. This means that, for a three-dimensional flow, a set of six additional differential equations must be calculated. As underlined by Pope [14], very few authors employed this model in large eddy simulations. One of the exceptions is the work of Deardorff (1973) [27] in atmospheric turbulence. Similarly to what happens with other models based on transport equations, the additional evolution equations considered in subgrid differential SGS models include unclosed terms that need to be modelled in terms of quantities from the resolved turbulent field. The subgrid-scale kinetic energy is another variable often used to model the unclosed terms. In this case, a transport equation similar to the one employed in the one-equation models mentioned above has to be solved. More details regarding this modelling strategy can be found in Sagaut [11], Pope [14] and Deardorff [27].

Differential SGS models discard the Boussinesq and local equilibrium approximations and, by solving a considerable set of differential equations, they are expected to be physically more consistent. Dropping the subgrid viscosity concept and the local equilibrium hypothesis comes with a cost, since differential subgrid stress models are considerably much more demanding in terms of computer effort than the other previously mentioned models.

Despite the fact that the steady and continuous growth of computer power over the years has encouraged large eddy simulations to be used in increasingly more complex contexts, LES of near-wall flows is still impossible at very high-Reynolds-numbers. Recent attempts to solve this problem resort to **hybrid RANS/LES models**. Two main strategies exist: zonal and continuous hybrid RANS/LES models.

In zonal hybrid RANS/LES strategies, RANS is used in the near-wall region allowing for coarser grids in this subdomain, while LES is employed far from the walls where the flow dynamics is dominated by larger turbulent motions. This modelling method is interesting in the sense that both RANS and LES procedures are employed as formulated originally, but this approach poses a problem regarding how the turbulent flow quantities computed in each subdomain are to be shared through the interface between the RANS and LES zones. The zonal hybrid RANS/LES approach has been used by Hamba [28, 29] for channel flows and by Temmerman *et al.* [30] for separated flows inside a channel.

Nonzonal or continuous hybrid RANS/LES methods are based on a universal modelling technique which behaves like a subgrid-scale model far from the walls and reverts to a RANS turbulence model in the near-wall region. These models employ a computational mesh with continuous variation of the grid size. One atractive tecnique for continuous hybrid RANS/LES universal procedures relies on one-equation models which become transport equations for the subgrid-scale kinetic energy on the "LES zone" and evolution equations for the total turbulent kinetic energy on the "RANS zone".

2.4 One-equation models based on transport of SGS kinetic energy and scalar variance

2.4.1 Transport equation for the SGS kinetic energy

The subgrid-scale (SGS) kinetic energy is one half of the contracted subgrid tensor, $\frac{\tau_{ii}}{2} = \frac{\overline{u_i^2} - \overline{u_i}^2}{2}$. The transport equation for the subgrid kinetic energy is given by [31]:

$$\begin{aligned}\frac{D}{Dt}\left(\frac{\tau_{ii}}{2}\right) = &\underbrace{\frac{1}{2}\frac{\partial}{\partial x_j}\left(\overline{u_i u_i}\,\overline{u}_j - \overline{u_i u_i u_j}\right)}_{D_{turb}} + \underbrace{\frac{\partial}{\partial x_j}\left(\overline{p}\,\overline{u}_j - \overline{p u_j}\right)}_{D_{press}} \\ &+ \underbrace{\nu\frac{\partial^2}{\partial x_j^2}\left(\frac{\tau_{ii}}{2}\right)}_{D_{visc}} \underbrace{-\nu\left(\overline{\frac{\partial u_i}{\partial x_j}\frac{\partial u_i}{\partial x_j}} - \frac{\partial \overline{u}_i}{\partial x_j}\frac{\partial \overline{u}_i}{\partial x_j}\right)}_{\Sigma} \\ &+ \underbrace{\frac{\partial}{\partial x_j}\left(\tau_{ij}\overline{u}_i\right)}_{D_{gs/sgs}} \underbrace{-\tau_{ij}\frac{\partial \overline{u}_i}{\partial x_j}}_{P}\end{aligned} \tag{2.44}$$

On the right hand side of (2.44), terms D_{turb}, D_{press} and D_{visc} represent the diffusion of the SGS kinetic energy due to subgrid turbulent fluctuations, pressure-velocity interactions and molecular viscosity, respectively. The final dissipation of the SGS kinetic energy by the action of molecular viscosity is expressed by the viscous SGS dissipation term, term Σ. The last two terms on the right hand side of (2.44) also appear on the evolution equation for the grid-scale kinetic energy but with opposite sign. Therefore these terms account for energy transfers between the resolved and the subgrid scales of motion. Term $D_{gs/sgs}$ characterises the diffusion of the SGS kinetic energy due to interactions between the GS and the SGS motions, while term P represents

the net energy transfer from the resolved to the unresolved turbulent scales. If $P > 0$ energy is transferred from the grid scales to the subgrid scales (forward energy scatter). On the other hand, backward energy scatter occurs whenever $P < 0$.

2.4.2 Transport equation for the SGS scalar variance

For a scalar quantity θ, the evolution equation for subgrid-scale scalar variance, $\frac{q_\theta}{2} = \frac{\overline{\theta^2} - \overline{\theta}^2}{2}$, is [31]:

$$\begin{aligned}\frac{D}{Dt}\left(\frac{q_\theta}{2}\right) = &\underbrace{\frac{1}{2}\frac{\partial}{\partial x_j}\left(\overline{\theta^2}\overline{u}_j - \overline{\theta^2 u_j}\right)}_{D_{\theta turb}} + \underbrace{\gamma\frac{\partial^2}{\partial x_j^2}\left(\frac{q_\theta}{2}\right)}_{D_{\theta molec}} \\ &- \underbrace{\gamma\left(\overline{G_j G_j} - \overline{G}_j\overline{G}_j\right)}_{\Sigma_\theta} + \underbrace{\frac{\partial}{\partial x_j}\left(q_j\overline{\theta}\right)}_{D_{\theta gs/sgs}} \underbrace{-q_j\overline{G_j}}_{P_\theta}\end{aligned} \tag{2.45}$$

On (2.45), $q_j = \overline{\theta u_j} - \overline{\theta}\overline{u}_j$ represents the subgrid scalar fluxes, $\overline{G}_j = \frac{\partial\overline{\theta}}{\partial x_j}$ is the filtered scalar gradient and γ is the molecular diffusivity. Terms $D_{\theta turb}$, $D_{\theta molec}$ and $D_{\theta gs/sgs}$ account for the diffusion of the subgrid-scale scalar variance due to the subgrid fluctuations, molecular diffusivity and scalar interactions between the resolved and subgrid scales. Σ_θ is represents the molecular subgrid-scale dissipation of the SGS scalar variance, while P_θ is the transfer from the resolved scalar variance, $\overline{\Theta} = \frac{|\overline{\theta}|^2}{2}$.

2.4.3 Modelled transport equations for the SGS kinetic energy and SGS scalar variance

In order to solve the evolution equation for the subgrid-scale kinetic energy, equation (2.44) is modelled by:

$$\frac{\partial}{\partial t}\left(K_{sgs}\right) + \frac{\partial}{\partial x_j}\left(K_{sgs}\overline{u}_j\right) = D^\Delta + P^\Delta - \varepsilon^\Delta, \tag{2.46}$$

where K_{sgs} is the modelled subgrid-scale kinetic energy, D^Δ represents the modelled diffusion terms, P^Δ is the modelled production term and ε^Δ is the modelled viscous SGS dissipation.

The equation for the evolution of the SGS scalar variance can be modelled by:

$$\frac{\partial}{\partial t}\left(\Theta_{sgs}\right) + \frac{\partial}{\partial x_j}\left(\Theta_{sgs}\overline{u}_j\right) = D^\Delta_{sgs} + P^\Delta_{sgs} - \varepsilon^\Delta_{sgs}, \tag{2.47}$$

in which Θ_{sgs} is the modelled SGS scalar variance, D^Δ_{sgs} and P^Δ_{sgs} are the modelled diffusion and production terms and ε^Δ_{sgs} represents the modelled molecular SGS dissipation.

2.4.4 Models for the viscous and molecular SGS dissipation terms

In large eddy simulation models based on the transport of the SGS kinetic energy and the SGS scalar variance, the several terms existing on the evolution equations for the subgrid-scale kinetic energy and the subgrid-scale scalar variance, (2.44) and (2.45), are associated with

subgrid quantities not available during the simulation. Therefore, the transport equations for the SGS kinetic energy and the SGS scalar variance have to be replaced by the modelled equations introduced in (2.46) and (2.47). The modelled evolution equations present modelled terms for the diffusion, production and dissipation terms.

The diffusion terms are usually modelled using a gradient-diffusion hypothesis, by which the diffusion terms sum is proportional to the kinetic energy gradient. An analysis regarding the behaviour of models for the diffusion terms present in the SGS kinetic energy and the SGS scalar variance equations is presented in the work of da Silva and Pereira [6].

Here, the focus is on the modelling strategies used for the viscous and molecular SGS kinetic energy and the SGS scalar variance dissipation terms, represensented by ε^{Δ} and $\varepsilon_{\theta}^{\Delta}$ on equations (2.46) and (2.47), respectively. Several models for those terms were analysed in *a priori* tests: the classical models [1, 2], the model used in hybrid RANS/LES [3, 4] and a recent model proposed by Jiménez *et al.* [5].

Classical models

The classical model for the SGS dissipation used by Schumann [1] and Yoshizawa [2] replaces terms ε^{Δ} and $\varepsilon_{\theta}^{\Delta}$ on the modelled equations (2.46) and (2.47) by:

$$\varepsilon_{a}^{\Delta} = C_{\varepsilon}^{a} \frac{K_{sgs}^{3/2}}{\Delta}. \tag{2.48}$$

$$\varepsilon_{\theta a}^{\Delta} = C_{\varepsilon\theta}^{a} \frac{K_{sgs}^{1/2} \Theta_{sgs}}{\Delta}. \tag{2.49}$$

Models based on hybrid RANS/LES

Models for the subgrid-scale dissipation terms based on hybrid RANS/LES methodologies [3, 4]:

$$\varepsilon_{b}^{\Delta} = C_{\varepsilon}^{b} \frac{\overline{K}^{3/2}}{\Delta} \tag{2.50}$$

$$\varepsilon_{\theta b}^{\Delta} = C_{\varepsilon\theta}^{b} \frac{\overline{K}^{1/2} \overline{\Theta}}{\Delta} \tag{2.51}$$

Model by Jiménez *et al.*

The model for the dissipation of the subgrid-scale scalar variance proposed by Jiménez *et al.* [5] is given by:

$$\varepsilon_{\theta c}^{\Delta} = \frac{C_{\theta}^{c}}{2} \left(\frac{\Theta_{sgs}}{K_{sgs}} \right) \varepsilon^{\Delta} \tag{2.52}$$

Chapter 3

Data bank

3.1 Direct numerical simulations of homogeneous isotropic turbulence

The data bank used to assess the different modelling strategies presented on subsection 2.4.4 was generated by direct numerical simulations of statistically stationary isotropic turbulence. Statistically steady isotropic turbulence was computed considering an unbounded cubical domain with side $L = 2\pi$ discretized with 192 collocation points in each direction. Periodic boundary conditions were assumed in all three directions of the flow. In order to achieve statistically stationary turbulence, the largest flow scales were forced by a method described by Alvelius [32]. The evolution of the flow was computed using a pseudo-spectral code with temporal advancement made by explicit third-order Runge-Kutta. Figure 3.1 shows the computational box with the calculated turbulent flow structures.

In order to account for different velocity and scalar fields dynamics, three direct numerical simulations were carried on: in two of them, the Reynolds number based on the Taylor microscale was $Re_\lambda = 95.6$ and the Schmidt numbers were $Sc = 0.2$ and $Sc = 0.7$. The remaining simulation considered $Re_\lambda = 39.4$ and $Sc = 3.0$. For each simulation, ten instantaneous and stationary steady velocity and scalar fields were captured for further analysis. The kinetic energy and scalar variance spectrum for all the simulations mentioned are represented on figure 3.1.

The three DNS responsible for the data bank generation are validated, as reported on previous works using the same data bank [6, 22]: the size of the computational domain is large enough in order to not affect the large scale structures, important parameters are satisfied to ensure the small scales resolution and the statistics built around the stationary velocity and scalar fields are in accordance with results from validated DNS used by other authors in similar conditions. More information regarding the simulations and data bank used in the present work can be acquired in [6] and citations therein.

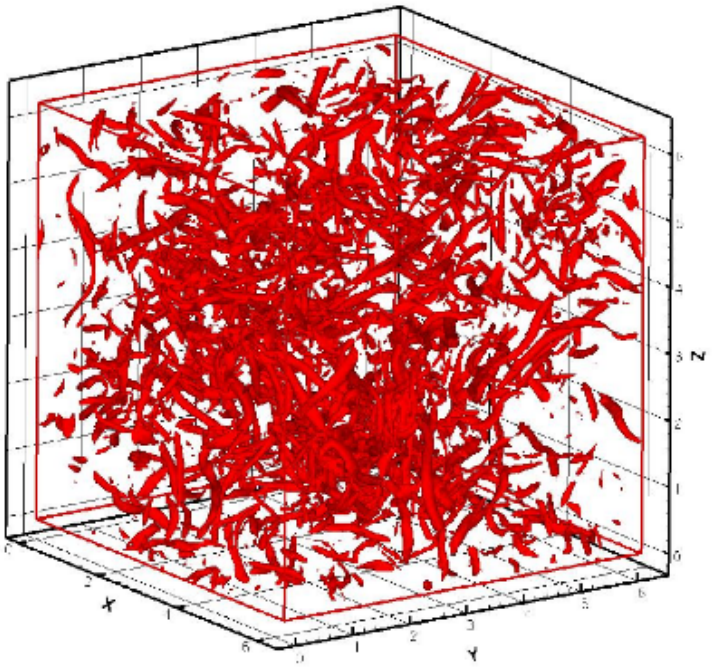

Figure 3.1: Computational domain and instantaneous turbulent field. Courtesy: C. Silva.

3.2 Numerical code

3.2.1 Pseudo-spectral methods

Spectral methods belong to a class of spatial discretization schemes used to compute ordinary differential equations with the aid of the the Fourier transform. This procedure simplifies the problem of transforming continuous differential equations into discrete equations, since a derivative in the physical space corresponds to a multiplication in the Fourier space. Due to the mathematical nature of the Fourier transform, the application of spectral methods to the flow equations is limited to problems where the boundary conditions are periodic. However, within their range of suitability and when compared with other spatial discretization techniques, spectral methods are highly accurate and extremelly fast, converging faster than any finite power of 1/N, N being the number of grid points in one direction, a property frequently referred to as *exponential convergence* (Canuto *et al.* [33]).

Homogeneous isotropic turbulence is statistically the most elementary case of turbulent flow. Usually, the computational domain used to simulate this type of flow consists in an unbounded cubical box and periodic boundary conditions are employed to approximate the flow in the unbounded domain (Geurts [34]). Because the existence of periodicity conditions is assured, the use of spectral methods is enabled.

Spectral methods make use of the governing equations in spectral space, equations (2.9), (2.10) and (2.13) on page 12.

The pseudo-spectral method is an adaptation of the pure spectral approach which has emerged to reduce the computational cost associated with convolution integral used to rep-

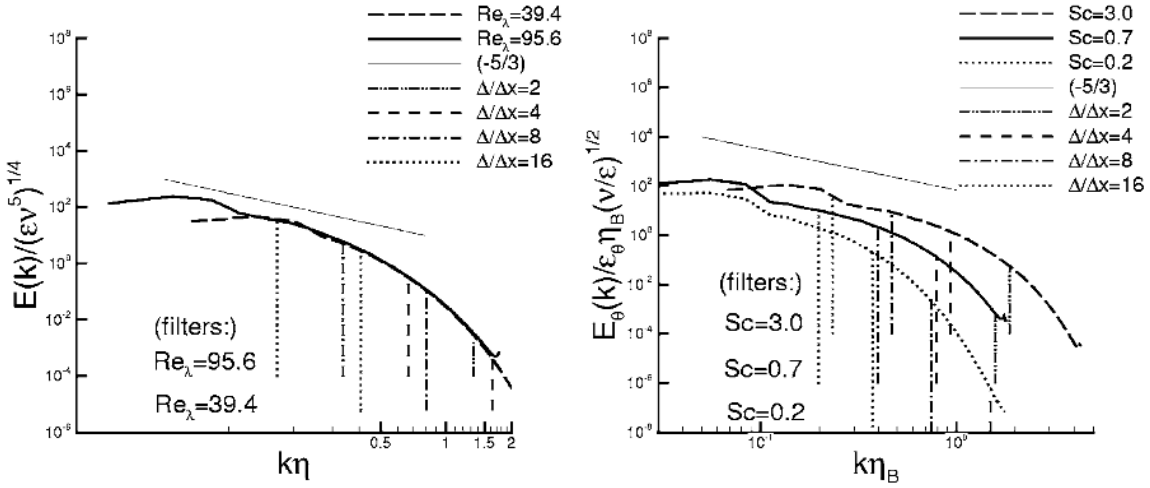

Figure 3.2: Kinetic energy and scalar variance spectra from all direct numerical simulations. From [6].

resent the convective non-linear terms in spectral space, the second term on the right-hand side of equations (2.9) and (2.13). The pseudo-spectral approach sets the problem in the physical space, where all mathematical operations are performed except the derivatives. Fourier transforms are employed to obtain the spatial derivatives and inverse Fourier transforms the result back to physical space (Geurts [34]).

3.2.2 Third-order Runge-Kutta method

Runge-Kutta methods are designed to solve partial differential equations written in the form $\frac{\partial y}{\partial x} = f(x, y(x))$. In this frame of reference, the Navier-Stokes equations can be expressed as:

$$\frac{\partial u_i}{\partial t} = f(t, u_i(t)).$$

The goal here is to compute u_i^{n+1} from the previous u_i^n, where $u_i^n = u_i(t^n)$ refers to the velocity field at the current computing time and $u_i^{n+1} = u_i\left(t^{n+1}\right)$ is the same quantity at the following time step, with step length $h = t^{n+1} - t^n$. The explicit 3$^{\text{rd}}$ order Runge-Kutta method defines three subsequential functions [35]:

$$\begin{aligned}
k_1 &= f(t^n, u_i^n); \\
k_2 &= f\left(t^n + \frac{h}{2}, u_i^n + \frac{h}{2}k_1\right); \\
k_3 &= f(t^n + h, u_i^n + h(-k_1 + 2k_2)).
\end{aligned}$$

And the velocity field at time step t^{n+1} is evaluated as:

$$u_i^{n+1} = u_i^n + \frac{h}{6}(k_1 + 4k_2 + k_3).$$

Chapter 4

A priori tests

The accuracy of SGS models can be assessed by reference to the exact solution of a turbulent flow, obtained either from an experiment or by direct numerical simulations, according to two different strategies: *a priori* and *a posteriori* testing. In *a priori* tests, the data from the exact solution is subject to an analytical filter leading to two known fields: the resolved and the subgrid fields. Because all the data concerning both the grid and the subgrid scales is available, it is possible to compute the exact and the modelled SGS tensors and further analysis is made to evaluate how well the modelled tensor relates to the actual SGS stresses. In *a posteriori* tests, a full large eddy simulation is carried out and the results are compared with the data obtained from the exact solution. *A priori* tests are important to assess modelling assumptions while *a posteriori* tests give a global picture of the performance of SGS models in LES.

Here, the study of the models' performance in *a priori* tests is made by statistical and spectral analysis. The goal is to assess how well the models for the SGS dissipation of the SGS kinetic energy and SGS scalar variance capture the statistical and spectral behaviour of the real SGS dissipation and how well the real and modelled variables are correlated.

4.1 *A priori* tests: setting up the variables

From the data bank generated by direct numerical simulations, the following quantities associated with the velocity and scalar fields are obtained for each mesh point of the computational domain:

- velocity field:

$$u_i, \quad u_i u_i, \quad \frac{\partial u_i}{\partial x_j}, \quad \frac{\partial u_i}{\partial x_j}\frac{\partial u_i}{\partial x_j};$$

- scalar field:

$$\theta, \quad \theta\theta, \quad \frac{\partial \theta}{\partial x_j}, \quad \frac{\partial \theta}{\partial x_j}\frac{\partial \theta}{\partial x_j}.$$

The previous instantaneous fields related to the velocity and scalar fields undergo four box-filtering operations, defined by equations (2.14) and (2.15), with filter width $\Delta_m = m\Delta x$, where $m = 2, 4, 8, 16$ and Δx is the grid spacing used in the DNS. For each filter width, one gets the filtered fields:

- velocity field:

$$\overline{u}_i, \quad \overline{u}_i\overline{u}_i, \quad \overline{u_i u_i}, \quad \frac{\partial \overline{u}_i}{\partial x_j}, \quad \frac{\partial \overline{u}_i}{\partial x_j}\frac{\partial \overline{u}_i}{\partial x_j}, \quad \overline{\frac{\partial u_i}{\partial x_j}\frac{\partial u_i}{\partial x_j}};$$

- scalar field:

$$\overline{\theta}, \quad \overline{\theta}\,\overline{\theta}, \quad \overline{\theta\theta}, \quad \frac{\partial \overline{\theta}}{\partial x_j}, \quad \frac{\partial \overline{\theta}}{\partial x_j}\frac{\partial \overline{\theta}}{\partial x_j}, \quad \overline{\frac{\partial \theta}{\partial x_j}\frac{\partial \theta}{\partial x_j}};$$

from which one can obtain the following variables:

- SGS kinetic energy:

$$\frac{\tau_{ii}}{2} = \frac{\overline{u_i u_i} - \overline{u}_i\overline{u}_i}{2}$$

- kinetic energy from the resolved scales:

$$\overline{K} = \frac{\overline{u}_i\overline{u}_i}{2}$$

- viscous dissipation of SGS kinetic energy:

$$\Sigma = \nu\left(\overline{\frac{\partial u_i}{\partial x_j}\frac{\partial u_i}{\partial x_j}} - \frac{\partial \overline{u}_i}{\partial x_j}\frac{\partial \overline{u}_i}{\partial x_j}\right) \tag{4.1}$$

- SGS scalar variance:

$$\frac{q_\theta}{2} = \frac{\overline{\theta\theta} - \overline{\theta}\,\overline{\theta}}{2}$$

- GS scalar variance:

$$\overline{\Theta} = \frac{\overline{\theta}\,\overline{\theta}}{2}$$

- molecular dissipation of the SGS scalar variance:

$$\Sigma_\theta = \gamma\left(\overline{\frac{\partial \theta}{\partial x_j}\frac{\partial \theta}{\partial x_j}} - \frac{\partial \overline{\theta}}{\partial x_j}\frac{\partial \overline{\theta}}{\partial x_j}\right) \tag{4.2}$$

And, finally, the models presented on subsection 2.4.4 are deduced by:

- Classical model

$$\varepsilon_a^\Delta = \frac{(\tau_{ii}/2)^{3/2}}{\Delta} \tag{4.3}$$

$$\varepsilon_{\theta a}^\Delta = \frac{(\tau_{ii}/2)^{1/2}\left(\frac{q_\theta}{2}\right)}{\Delta} \tag{4.4}$$

- Model for hybrid LES/RANS

$$\varepsilon_b^\Delta = \frac{\left(\overline{K}\right)^{3/2}}{\Delta} \tag{4.5}$$

$$\varepsilon_{\theta b}^\Delta = \frac{\left(\overline{K}\right)^{1/2}\left(\overline{\Theta}\right)}{\Delta} \tag{4.6}$$

- Model by Jiménez

$$\varepsilon_{\theta c}^\Delta = \frac{1}{2}\frac{q_\theta/2}{\tau_{ii}/2}\Sigma \tag{4.7}$$

The model constants are absent on the model formulations presented above. For each simulation and for each filter width considered, the model constants are computed according to:

$$\langle \varepsilon^{\Delta} \rangle = \langle C_{\varepsilon} \rangle \langle \Sigma \rangle \qquad (4.8) \qquad\qquad \langle \varepsilon_{\theta}^{\Delta} \rangle = \langle C_{\varepsilon\theta} \rangle \langle \Sigma_{\theta} \rangle, \qquad (4.9)$$

where $\langle \quad \rangle$ denotes the mean value involving all points from all the ten instantaneous fields captured.

4.2 *A priori* tests: analysis on the physical space

Given the high sensibility of turbulence to very small disturbances, turbulent flows possess a rather random and chaotic behaviour. As already evidenced on figure 1.1 on page 3, the measurement of a turbulent flow variable can be significantly different in two experiments carried out under nominally identical conditions. However, the statistics built around the turbulent flow signals are quite reproducible, for example, the mean value of a turbulent flow signal is likely to be the same or at least very similar for all experiments performed under the same conditions. Therefore, one of the most common ways to study the behaviour of turbulence relies upon statistical analysis.

Statistical analysis is very useful in *a priori* tests in order assess the performance of subgrid models. Several statistical tools such as the mean, variance or higher order moment coefficients can be computed for both the real and modelled variables and it is possible to understand whether or not the statistics of the modelled quantities are related to the exact flow quantities. Moreover, the relationship between the exact and modelled flow variables can be measured by the use of correlation factors or joint probability density functions.

Here the formulation for all statistical functions used to assess the models' behaviour are presented: correlation, variance, skewness and flatness factors along with the probability density and joint probability density functions.

The **probability density function (p.d.f.)** $f_U(u)$ of a turbulent random variable U associates all possible values of U to the probability of their occurence. If $P(a < U < b)$ denotes the probability of U being in the range $a \rightarrow b$, then the p.d.f. $f_U(u)$ has to verify:

1. $f_U(u) \geqslant 0$;
2. $\int_{-\infty}^{+\infty} f_U(u)du = 1$;
3. $P(a < U < b) = \int_a^b f_U(u)du$.

An important measure of central tendency of a random variable is its **mean** value, or expected value, defined by:

$$\mu = E(U) = \langle U \rangle = \int_{-\infty}^{+\infty} u f_U(u)du = \frac{1}{N}\sum_{i=1}^{N} U^{(i)}, \qquad (4.10)$$

where $U^{(i)}$ is a number from the set of N values of U, $\{U^{(1)}, U^{(2)}, \ldots, U^{(N)}\}$. The notation adopted on (4.10) is the same as the one presented for the Reynolds-averaged Navier-Stokes on

subsection 1.2.1 on page 6.

To characterize the variability or scatter of U around its mean value, the **variance** of a turbulent flow variable U is expressed by:

$$\begin{aligned}\sigma^2 = V(U) = \langle U''^2 \rangle &= \int_{-\infty}^{+\infty} (u - \langle U \rangle)^2 \, f_U(u) du \\ &= \frac{\sum_{i=1}^{N} \left(U^{(i)} - \langle U \rangle \right)^2}{N} = \frac{\sum_{i=1}^{N} U^{(i)2}}{N} - \left(\frac{\sum_{i=1}^{N} U^{(i)}}{N} \right)^2 \\ &= \langle U^2 \rangle - \langle U \rangle^2.\end{aligned} \tag{4.11}$$

In order to measure the variability of a random variable in the original units of the variable, the **standard deviation**, or root mean square (r.m.s.) of U is the positive square-root of $V(U)$: $\sigma = \text{r.m.s.}(U) = \sqrt{\langle U''^2 \rangle}$.

More generally, a **nth central moment** is defined by:

$$\mu_n \equiv \langle U''^n \rangle = \int_{-\infty}^{+\infty} (u - \langle U \rangle)^n \, f_U(u) du. \tag{4.12}$$

The variance is a 2^{nd} central moment and standardization of μ_2 results in the root mean square, $\sigma = \mu_2/\sigma$. Other important standardized moments are the skewness and flatness coefficients.

The **skewness factor** is the standardized 3^{rd} central moment:

$$\begin{aligned}S(U) = \frac{\langle U''^3 \rangle}{\sigma^3} &= \int_{-\infty}^{+\infty} (u - \langle U \rangle)^3 \, f_U(u) du \\ &= \frac{1}{\sigma^3} \left(\langle U^3 \rangle - 3 \langle U \rangle V(U) - \langle U \rangle^3 \right).\end{aligned} \tag{4.13}$$

$S(U)$ gives a measure of the assymmetry of the probability density function. If $S(U) = 0$ then the p.d.f. is symmetric about $U = \mu$, if $S(U) > 0$, the p.d.f. is distributed as pictured on figure 4.1.

A normalized version of the 4^{th} central moment is the **flatness coefficient** (also refered to as kurtosis):

$$\begin{aligned}F(U) = \frac{\langle U''^4 \rangle}{\sigma^4} &= \int_{-\infty}^{+\infty} (u - \langle U \rangle)^4 \, f_U(u) du \\ &= \frac{1}{\sigma^4} \left(\langle U^4 \rangle - 4 \langle U \rangle S(U) \left(\text{r.m.s.}(U) \right)^3 - 6 \langle U \rangle^2 V(U) - \langle U \rangle^4 \right).\end{aligned} \tag{4.14}$$

$F(U)$ is a measure of the flatness of the probability density function, figure 4.2. Larger values of $F(U)$ represent p.d.f.s with narrow peaks and broader skirts, which means that values of U near and far from $U = \mu$ have a higher probability of occurence, and hence high $F(U)$ turbulent signals are usually very intermitent.

As a consequence of the *central limit theorem*, in statistics theory a very important probability distribution is the Gaussian or **normal distribution.** The central limit theorem states that a

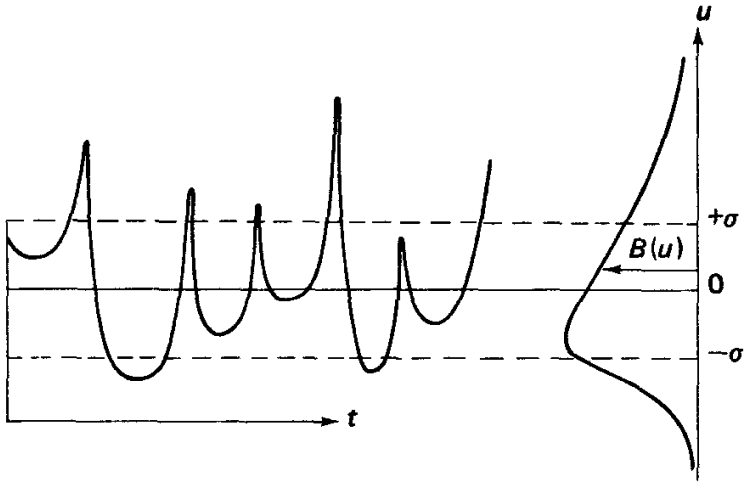

Figure 4.1: A function with positive skewness. Source: Tennekes and Lumley [12].

set of N samples of a random variable U obtained from a series of independent measurements is described by a normal probability distribution as the number of samples tends to the infinity, $N \to \infty$ [36]. For most random events, the p.d.f. is modelled using a normal distribution:

$$f(U) = \frac{1}{\sigma\sqrt{2\pi}} \exp^{\frac{-(U-\mu)^2}{2\sigma^2}}, \tag{4.15}$$

in which μ is the mean value of U and σ is its standart deviation.

The statistics defined by the set of equations (4.10) to (4.14) are used to determine the behaviour of one random variable U. To measure the relationship between two random variables U and V other tools are employed: the joint probability density function and correlation coefficients.

The simultaneous behaviour of two random variables U and V can be described by their **joint probability density function (j.p.d.f.).** If $P(a_1 < U < b_1, a_2 < V < b_2)$ is the probability of U being in the interval $[a_1, b_1]$ while V lies in the range $a_2 \to b_2$, their j.p.d.f. $f_{UV}(u, v)$ has the following properties:

1. $f_{UV}(u, v) \geqslant 0$;
2. $\int_{-\infty}^{+\infty} \int_{-\infty}^{+\infty} f_{UV}(u, v) du dv = 1$;
3. $P(a_1 < U < b_1, a_2 < V < b_2) = \int_{a_1}^{b_1} \int_{a_2}^{b_2} f_{UV}(u, v) dv du$.

The **covariance** is a measure of linear association between two random variables [36].

$$\sigma_{UV} = \langle U''V'' \rangle = \int_{-\infty}^{+\infty} \int_{-\infty}^{+\infty} (u - \langle U \rangle)(v - \langle V \rangle) f_{UV}(u, v) du dv. \tag{4.16}$$

Perhaps a more relevant quantity is the **correlation coefficient** obtained by scaling (4.16) by

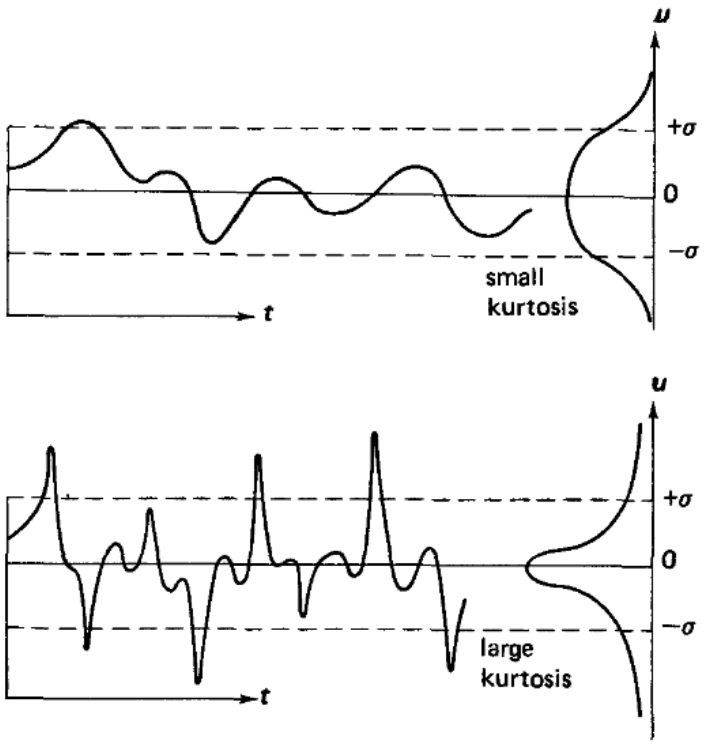

Figure 4.2: Functions with small and large kurtosis. Source: Tennekes and Lumley [12].

the standard deviation of each random variable:

$$\rho_{UV} = \frac{\langle U''V'' \rangle}{\sqrt{\langle U''^2 \rangle \langle V''^2 \rangle}}. \tag{4.17}$$

For two random variables U and V: $-1 \leqslant \rho_{UV} \leqslant 1$. If $\rho_{UV} = 0$, then U and V are independent and hence there is no correlation between them. When $\rho_{UV} > 0$, positive (negative) values of $U - \langle U \rangle$ are preferentially related with positive (negative) values of $V - \langle V \rangle$ and, conversely, a negative correlation coefficient ρ_{UV} corresponds to a preferential association between $(U - \langle U \rangle) > 0 \ (< 0)$ and $(U - \langle U \rangle) < 0 \ (> 0)$. The extreme scenarios $\rho_{UV} = 1$ and $\rho_{UV} = -1$ amount to situations where the random variables U and V are perfectly correlated and perfectly negatively correlated, respectively.

Because the correlation is a dimensionless quantity, it can be used to compare linear relationships between pairs of variables in different units and can be easier to interpret than the covariance.

All the statistics and probability density functions presented here were performed for each simulation, that is, for each Reynolds or Schmidt number, and for each filter width under consideration, $\Delta/\Delta x = 2, 4, 8, 16$.

4.3 *A priori* tests: analysis on the Fourier space

Spectral analysis allows one to study turbulent flow variables in terms of their dependence on the wave number. As already mentioned on subsection 2.1, the wave number can be interpreted as being proportional to l^{-1}, where l represents a characteristic eddy size. Here, the three-dimensional spectrum is computed for both the exact and modelled variables in order to express the variance of the variable as a function of the wave number k.

The spatial three-dimensional spectrum of a turbulent flow variable ϕ is defined by [7]:

$$\mathsf{E}_{\phi}(\mathsf{k})\delta\left(\mathbf{k}+\mathbf{k'}\right) = 2\pi\mathsf{k}^2\langle\widehat{\phi}\left(\mathbf{k}\right)\cdot\widehat{\phi}^{*}\left(\mathbf{k'}\right)\rangle,$$

where $\widehat{\phi}\left(\boldsymbol{\kappa}\right)$ is the Fourier transform of ϕ introduced in (2.4) on subsection 2.1 and $\mathbf{k} = (\mathsf{k}_1, \mathsf{k}_2, \mathsf{k}_3)$ is the 3D wave number with wave number norm $\mathsf{k} = \sqrt{\mathsf{k}_1^2 + \mathsf{k}_2^2 + \mathsf{k}_3^2}$. The variance of ϕ is related to $\mathsf{E}_{\phi}\left(\mathsf{k}\right)$ by:

$$\frac{1}{2}\langle\phi''^2\rangle = \int_0^{+\infty}\mathsf{E}_{\phi}\left(\mathsf{k}\right)\mathrm{d}\mathsf{k}.$$

$\mathsf{E}_{\phi}\left(\mathsf{k}\right)$ expresses the contribution of wave number k to the variance of ϕ, $\frac{1}{2}\langle\phi''^2\rangle$.

Part II

Results: Article published in the Journal of Turbulence

Journal of Turbulence
Vol. 9, No. 25, 2008, 1–36

Taylor & Francis
Taylor & Francis Group

Analysis of the viscous/molecular subgrid-scale dissipation terms in LES based on transport equations: *A priori* tests

C.B. da Silva,* S. Rego and J.C.F. Pereira

IDMEC/IST Technical University of Lisbon, Mecânica I, 1º andar (LASEF), Av. Rovisco Pais, 1049-001 Lisboa, Portugal

(*Received 9 October 2007; final version received 2 June 2008*)

One trend in large-eddy simulations (LES) involves the use of a transport equation for the subgrid-scale (SGS) kinetic energy. For problems involving active or passive scalar fields a SGS scalar variance transport equation is also used. The terms from these equations involve sub-filter scale quantities that are not accessible during LES and thus require modelling. By far the greatest challenge for modelling in these equations comes from the *viscous and the molecular SGS dissipation* terms that represent the final (dissipation) stages of the 'energy cascade mechanism' whereby the SGS kinetic energy and SGS scalar variance are dissipated through the action of the molecular viscosity and diffusivity, respectively. In this work direct numerical simulations (DNS) of statistically stationary (forced) homogeneous, isotropic turbulence are used to (i) analyse the topology and spatial localisation of the viscous and the molecular SGS dissipation terms, (ii) assess three models currently used for these terms and (iii) present some guidelines to improve or develop future models for these terms. The models analysed here are (a) the classical model used by e.g. Schumann [1] and Yoshizawa [2], (b) the model used in hybrid RANS/LES by Paterson and Peltier [3], and by Hanjalic [4], and (c) the model for the molecular SGS dissipation of SGS scalar variance from Jiménez et al. [5]. The classical models for the molecular SGS dissipation give very good results in terms of topology, spatial localisation (in the physical space), statistical behaviour and spectral characteristics. Moreover, the model constants approach asymptotically the theoretical values as the Reynolds number and filter sizes increase which supports the use of a constant value in engineering and geophysical applications, instead of using a dynamic procedure for their computation as in Ghosal et al. [6]. For the molecular SGS dissipation of SGS scalar variance the model from Jiménez et al. [5] performs even better than the classical model and should be the preferred model for this term when the Schmidt number is close to 1.0. Finally, all the tests showed that the models used in hybrid RANS/LES tested here give very poor results either in terms of their topological, statistical or spectral characteristics. The reason behind this is connected with the deficient spectral representation of the exact molecular SGS dissipation terms.

Keywords: subgrid-scale modelling; viscous/molecular SGS dissipation; isotropic turbulence, direct numerical simulations

1. Introduction

In large-eddy simulations (LES) the large-flow structures which are responsible for the most important transfers of mass, momentum and heat are explicitly calculated while the effect of the small scales is modelled by a subgrid-scale (SGS) model. In many-flow simulations the small scales of motion are statistically close to isotropic, carry a relatively small amount of the total

*Corresponding author. Email: Carlos.Silva@ist.utl.pt

ISSN: 1468-5248 online only

DOI: 10.1080/14685240802251525
http://www.tandf.co.uk/journals

kinetic energy, adjust almost immediately to the dynamics of the large scales and their major role is associated with the viscous dissipation of kinetic energy. These facts allowed the development of relatively simple SGS models possessing some degree of universality which makes them very attractive compared to other modelling strategies e.g. based on the Reynolds averaged Navier–Stokes equations—RANS (see [7, 8] for a review of LES).

However, it has been recognised early on that in some engineering and natural flows the design of universal and simple SGS models would be difficult to achieve for a number of reasons: (i) the isotropic assumption of the small-scale motions is not observed in many flows even at very high-Reynolds numbers, particularly for the passive scalar field [9, 10], (ii) in many LES the SGS motions do possess a significant part of the total kinetic energy [11] and, closely related to this, (iii) for high-Reynolds numbers and/or coarse meshes the SGS motions need a non-negligible time to adjust to local unsteadiness from the large scales, i.e. the *local equilibrium assumption* between the large and small scales of motion fails [12, 13].

In order to overcome these limitations numerous SGS models use a transport equation for the SGS kinetic energy, e.g. [1, 2, 6, 14–20]. The use of a transport equation for the SGS kinetic energy is interesting also to many hybrid RANS/LES and URANS/LES modelling strategies e.g. [21–25].

Similarly, in LES involving a passive or active scalar field several new unclosed terms arise. One way to deal with these unknown terms is to solve an additional SGS scalar variance transport equation [26]. For example, in LES of reacting flows the variance of the mixture fraction is very important [27]. Therefore, some combustion models use an additional transport equation for the variance of the SGS mixture fraction e.g. [5, 28, 29].

The study of transport equations for the SGS kinetic energy and SGS scalar variance is thus of great relevance to many fields, since in LES most of the terms from these equations are unknown and have to be modelled. In this context an exhaustive description of the role and topology of all the terms from the SGS kinetic energy equation was given by da Silva and Métais [12]. Recently, da Silva and Pereira [30] analysed the modelling of the diffusion terms from the SGS kinetic energy and the SGS scalar variance equations, which are usually lumped together and are modelled using a ‘gradient-diffusion’ hypothesis. It was shown that the classical ‘gradient-diffusion’ model gives poor results for the diffusion terms in both equations and a new model was proposed to improve this situation [30].

By far the greatest challenge when modelling the transport equations for the SGS kinetic energy and SGS scalar variance comes from the *viscous/molecular SGS dissipation* terms which represent the final dissipation of the SGS kinetic energy and SGS scalar variance caused by viscous/molecular effects, at the end of the energy cascade mechanism. Note that these dissipation terms are not to be confused with the transfer of kinetic energy and scalar variance between grid and subgrid-scales, which generally represent a production term in these transport equations.

Compared to the viscous dissipation of (total) kinetic energy and the molecular dissipation of (total) scalar variance for which much work was already undertaken (e.g. [31–35]) few works analysed the viscous/molecular SGS dissipation terms. For the SGS kinetic energy equation the viscous SGS dissipation term was analysed by Meneveau and O’Neil [36], Menon et al. [37], da Silva and Métais [12] and Chumakov [38]. Much less is known about the molecular SGS dissipation of the SGS scalar variance, although some works analysed a related quantity—the sub-filter scalar dissipation—due to its importance to combustion simulations (e.g. [28, 39, 40]).

The classical models used for the molecular SGS dissipation terms are based in the *self-similarity* of the *energy cascade*, but some new models have been proposed recently. For the SGS kinetic energy equation new models for the viscous SGS dissipation term were developed by Langhe et al. [23], Chaouat and Schiestel [41], and Chumakov and Rutland [42]. Concerning

the SGS scalar variance equation Jiménez et al. [5, 29], and Chumakov and Rutland [42, 43] proposed new models for the molecular SGS dissipation term.

The goal of the present work is threefold: (i) to provide a complete characterisation of the viscous/molecular SGS dissipation terms from the SGS kinetic energy and SGS scalar variance equations, respectively, concerning their topology and one-point statistics, (ii) to assess the performance of several models in *a priori* tests and (iii) to give practical advices for the modelling of the viscous/molecular SGS dissipation terms. It is expected that the present analysis will highlight the strengths and limitations of the present models, and will give new insights which will help the development of more accurate models for the viscous/molecular SGS dissipation terms. The analysis carried out here is made by applying a box filter to direct numerical simulations (DNS) of statistically stationary (forced) homogeneous isotropic turbulence [30] using correlation coefficients, joint probability density functions (PDFs), several one-point statistics such as the variance, skewness and the flatness factors, as well as spectra from the exact and modelled viscous/molecular SGS dissipations. Even if the models analysed here are to be used in much more complex turbulent flows than in isotropic turbulence, they have to show good results in this simple flow if they are to succeed in more complex situations.

This paper is organised as follows. In the following section, the equations governing the exact and modelled SGS kinetic energy and SGS scalar variance and each one of its terms are described. The classical as well as new models used for the viscous/molecular SGS dissipation terms are reviewed. In Section 3 we describe the DNS of isotropic turbulence used in this work. Section 4 focuses in the characterisation of the exact viscous/molecular SGS dissipation terms and Section 5 analyses the performance of some models using classical *a priori* tests. Finally, in Section 6 the paper ends with an overview of the main results, conclusions and perspectives for modelling the viscous/molecular SGS dissipation terms.

2. Governing equations

In this section we review the exact and modelled transport equations for the SGS kinetic energy and SGS scalar variance, and some of the models currently used for the viscous/molecular SGS dissipation terms are reviewed.

2.1. *Evolution of the SGS kinetic energy*

The SGS kinetic energy $\tau_{ii}/2$ is governed by the exact equation (see e.g. [12, 30, 44]),

$$\frac{\mathrm{D}}{\mathrm{D}t}\left(\frac{\tau_{ii}}{2}\right) = \underbrace{\frac{1}{2}\frac{\partial}{\partial x_j}\left[\overline{u_i u_i}\,\overline{u_j} - \overline{u_i u_i u_j}\right]}_{D_{\mathrm{turb}}} + \underbrace{\frac{\partial}{\partial x_j}\left[\overline{p}\,\overline{u_j} - \overline{p u_j}\right]}_{D_{\mathrm{press}}}$$
$$+ \underbrace{\nu\frac{\partial^2}{\partial x_j \partial x_j}\left(\frac{\tau_{ii}}{2}\right)}_{D_{\mathrm{visc}}} - \underbrace{\nu\left[\overline{\frac{\partial u_i}{\partial x_j}\frac{\partial u_i}{\partial x_j}} - \frac{\partial \overline{u_i}}{\partial x_j}\frac{\partial \overline{u_i}}{\partial x_j}\right]}_{\Sigma} + \underbrace{\frac{\partial}{\partial x_j}\left(\tau_{ij}\overline{u_i}\right)}_{D_{\mathrm{gs/sgs}}} - \underbrace{\tau_{ij}\frac{\partial \overline{u_i}}{\partial x_j}}_{P}, \tag{1}$$

where u_i is the velocity vector field, $\tau_{ij} = \overline{u_i u_j} - \overline{u_i}\,\overline{u_j}$ is the SGS stresses tensor, ν is the molecular viscosity and the overlay symbol $(\overline{\ })$ represents a spatial filtering operation. Note that here $\overline{p}$ means $\frac{\overline{p}}{\rho}$ for convenience, where p is the pressure field.

In Equation (1) D_{turb}, D_{press} and D_{visc} represent the diffusion of SGS kinetic energy through SGS turbulent fluctuations, pressure–velocity interactions and molecular viscosity, respectively. The final dissipation of SGS energy by molecular viscosity, associated with the 'end' of the energy cascade mechanism, is represented by term Σ—*the viscous SGS dissipation* term. The two last terms in Equation (1) also appear (with opposite sign) in the grid-scale (GS) kinetic energy equation $\bar{K} = (\overline{u_i})^2/2$, and thus represent exchanges between the GS and SGS kinetic energy equations. Term $D_{\text{gs/sgs}}$—GS/SGS diffusion—represents a redistribution due to GS/SGS interactions, whereas P—GS/SGS transfer—represents the net transfer of kinetic energy between GS and SGS. If $P > 0$ the term acts as a source in Equation (1) and describes the flow of energy from GS into SGS (forward scatter). Backscatter occurs whenever $P < 0$.

An exhaustive description of the dynamics and topology of each term in Equation (1) was given by da Silva and Métais [12]. Unlike the viscous dissipation of total kinetic energy $\varepsilon = 2\nu S_{ij} S_{ij}$ (where $S_{ij} = 1/2(\partial u_i/\partial x_j + \partial u_j/\partial x_i)$ is the rate-of-strain tensor), the viscous SGS dissipation Σ tends to be located at the core of the flow vortices [12]. Furthermore, in agreement with Meneveau and O'Neil [36] there is a strong correlation between this term and the local SGS kinetic energy. The physics and modelling of the diffusion terms from the SGS kinetic energy and SGS scalar variance transport equations were analysed recently by da Silva and Pereira [30].

2.2. *Evolution of the SGS scalar variance*

The exact equation for the evolution of the SGS scalar variance, $q_\theta/2 = [\overline{\theta^2} - \overline{\theta}^2]/2$, is given by Jiménez et al. [5, 29],

$$\frac{\mathrm{D}}{\mathrm{D}t}\left(\frac{q_\theta}{2}\right) = \underbrace{\frac{1}{2}\frac{\partial}{\partial x_j}\left[\overline{\theta^2}\,\overline{u_j} - \overline{\theta^2 u_j}\right]}_{D_{\theta\text{turb}}} + \underbrace{\gamma\frac{\partial^2}{\partial x_j \partial x_j}\left(\frac{q_\theta}{2}\right)}_{D_{\theta\text{molec}}} - \underbrace{\gamma\left[\overline{G_j G_j} - \overline{G_j}\,\overline{G_j}\right]}_{\Sigma_\theta} + \underbrace{\frac{\partial}{\partial x_j}\left(q_j\overline{\theta}\right)}_{D_{\theta\text{gs/sgs}}} - \underbrace{q_j\overline{G_j}}_{P_\theta}, \tag{2}$$

where $q_j = \overline{\theta u_j} - \overline{\theta}\,\overline{u_j}$ represents the SGS scalar fluxes, $\overline{G_j} = \partial\overline{\theta}/\partial x_j$ is the filtered scalar gradient and γ is the molecular diffusivity.

In Equation (2) terms $D_{\theta\text{turb}}$, $D_{\theta\text{molec}}$ and $D_{\theta\text{gs/sgs}}$ represent the diffusion due to SGS motions, molecular diffusivity and scalar GS/SGS interactions, respectively. The term Σ_θ is the *molecular SGS dissipation* and represents the molecular dissipation of SGS scalar variance, while P_θ is the net transfer from the GS scalar variance, $\overline{\Theta} = (\overline{\theta})^2/2$ (see Kang and Meneveau [45], Jiménez et al. [29]). Note that for cut-off filters the SGS kinetic energy is equal to $\tau_{ii}/2 = \overline{u_i^{''}\,u_i^{''}}/2$, where $u_i^{''}$ is the subgrid-scale part of the velocity vector, while the SGS scalar variance becomes $q_\theta/2 = (\overline{\theta^{''2}})/2$.

2.3. *Modelled equations for the SGS kinetic energy and SGS scalar variance*

The SGS kinetic energy transport equation is usually modelled replacing Equation (1) by [6, 19],

$$\frac{\partial}{\partial t}(K_{\text{sgs}}) + \frac{\partial}{\partial x_j}\left(K_{\text{sgs}}\overline{u_j}\right) = D^{\Delta} + P^{\Delta} - \varepsilon^{\Delta}, \tag{3}$$

where K_{sgs} is the modelled SGS kinetic energy $\tau_{ii}/2$, and the convective term in the lhs of the equation is written in conservative form. D^{Δ} represents the sum of the diffusion terms from Equation (1) D_{turb}, D_{press}, D_{visc} and $D_{\text{gs/sgs}}$. The second term on the rhs of Equation (3) is the modelled SGS energy production, $P^{\Delta} = -\tau_{ij}\partial\overline{u_i}/\partial x_j$, and ε^{Δ} is the modelled viscous SGS dissipation corresponding to term Σ in Equation (1).

For the SGS scalar variance the model equation is [14]

$$\frac{\partial}{\partial t}\left(\Theta_{\text{sgs}}\right) + \frac{\partial}{\partial x_j}(\Theta_{\text{sgs}}\overline{u_j}) = D_{\theta}^{\Delta} + P_{\theta}^{\Delta} - \varepsilon_{\theta}^{\Delta}, \tag{4}$$

where Θ_{sgs} is the modelled SGS scalar variance $q_{\theta}/2$, and the terms on the rhs of Equation (4) account for the diffusion terms in Equation (2) $D_{\theta\text{turb}}$, $D_{\theta\text{press}}$ and $D_{\theta\text{molec}}$, the production term P_{θ} and the molecular SGS dissipation Σ_{θ}, respectively.

2.4. *Modelling the viscous/molecular SGS dissipation terms*

Arguably, the biggest challenge for modelling in Equations (3) and (4) comes from the viscous and molecular dissipations of SGS kinetic energy and SGS scalar variance, respectively, represented by terms ε^{Δ} and $\varepsilon_{\theta}^{\Delta}$. These quantities are not to be confused with the all important viscous dissipation of total kinetic energy $\varepsilon = 2\nu S_{ij}S_{ij}$, and with the molecular dissipation of total scalar variance $\varepsilon_{\theta} = 2\gamma G_j G_j$. Numerous works addressed the topology, dynamics and statistical properties of these dissipations e.g. [31–35, 46].

The classical modelling used for ε^{Δ} and $\varepsilon_{\theta}^{\Delta}$ is based on the *self-similarity of the energy cascade* and on the *dissipation law* [47],

$$\varepsilon \sim \frac{u_0^3}{l_0}, \tag{5}$$

where u_0 and l_0 are velocity and length scales characteristic of the large-scale flow motions. Invoking the self-similarity of the energy cascade and supposing that at the subgrid-scale level the characteristic velocity and length scales are the square root of the SGS kinetic energy $u(l) \sim K_{\text{sgs}}^{1/2}$, and the implicit filter width $l \sim \Delta$, respectively, we obtain the classical model for ε^{Δ} [1, 2, 6, 17, 19],

$$\varepsilon_a^{\Delta} = C_{\varepsilon}^{a}\frac{K_{\text{sgs}}^{3/2}}{\Delta}, \tag{6}$$

whereas for the SGS scalar variance equation the dissipation term is modelled by Schmidt and Schumann [14],

$$\varepsilon_{\theta a}^{\Delta} = C_{\varepsilon\theta}^{a}\frac{K_{\text{sgs}}^{1/2}\Theta_{\text{sgs}}}{\Delta}, \tag{7}$$

where C_{ε}^{a} and $C_{\varepsilon\theta}^{a}$ are model constants. Considering an inertial range kinetic energy spectrum $E(k) = C_K \langle\varepsilon\rangle^{2/3} k^{-5/3}$, and an inertial-convective range scalar variance spectrum $E_{\theta}(k) = C_{\theta K}\langle\varepsilon_{\theta}\rangle\langle\varepsilon\rangle^{-1/3}k^{-5/3}$, the definitions of the subgrid-scale kinetic energy

$$K_{\text{sgs}} = \int_{\pi/\Delta}^{\infty} E(k)\mathrm{d}k, \tag{8}$$

and of the subgrid-scale scalar variance,

$$\Theta_{\rm sgs} = \int_{\pi/\Delta}^{\infty} E_\theta(k){\rm d}k, \tag{9}$$

together with Equations (6) and (7), lead to the following expressions for the model constants C_ε^a and $C_{\varepsilon\theta}^a$ [1, 14],

$$C_\varepsilon^a = \pi \left(\frac{2}{3C_K}\right)^{3/2} \tag{10}$$

and

$$C_{\varepsilon\theta}^a = \frac{2\pi}{3C_{\theta K}} \left(\frac{2}{3C_K}\right)^{1/2}, \tag{11}$$

where C_K and $C_{\theta K}$ are the Kolmogorov and Obukhov–Corrsin constants, respectively, and the implicit grid filter Δ is taken from the inertial and inertial-convective range, where $\langle\varepsilon\rangle = \langle\varepsilon_a^\Delta\rangle$ and $\langle\varepsilon_\theta\rangle = \langle\varepsilon_{\theta a}^\Delta\rangle$. Using $C_K = 1.6$ and $C_{\theta K} = 1.34$ we get $C_\varepsilon^a = 0.845$ and $C_{\varepsilon\theta}^a = 2.02$, respectively. In most models, these model constants are either chosen as constants for the whole flow (e.g. [1, 14, 18]), or calculated dynamically (e.g. [6, 19, 17]).

New models for ε^Δ and $\varepsilon_\theta^\Delta$ have been proposed recently. In hybrid continuous RANS/LES turbulence modelling it is sometimes advantageous to model the viscous SGS dissipation by replacing $K_{\rm sgs}$ by $\overline{K}$ in Equation (6), which leads to the following model for ε^Δ [3, 4],

$$\varepsilon_b^\Delta = C_\varepsilon^b \frac{\overline{K}^{3/2}}{\Delta}. \tag{12}$$

A similar equation for the molecular SGS dissipation of SGS scalar variance would be

$$\varepsilon_{\theta b}^\Delta = C_{\varepsilon\theta}^b \frac{\overline{K}^{1/2}\overline{\Theta}}{\Delta}. \tag{13}$$

These formulations are particularly useful to switch between the RANS and the LES modes in the so-called detached-eddy simulations (DES).

Recently, Chumakov and Rutland [43, 42] proposed a new model for the viscous SGS dissipation and for the molecular SGS dissipation, through,

$$\varepsilon^\Delta \sim \nu \left[\frac{2K_{\rm sgs}}{L_{kk}}\right]^\alpha \left[\frac{\partial\widehat{\overline{u_i}}}{\partial x_j}\frac{\partial\overline{u_i}}{\partial x_j} - \frac{\widehat{\partial\overline{u_i}}}{\partial x_j}\frac{\widehat{\partial\overline{u_i}}}{\partial x_j}\right], \tag{14}$$

and

$$\varepsilon_\theta^\Delta \sim \gamma \frac{2q_\theta}{L_\theta} \left[\frac{\partial\widehat{\overline{\theta}}}{\partial x_j}\frac{\partial\overline{\theta}}{\partial x_j} - \frac{\widehat{\partial\overline{\theta}}}{\partial x_j}\frac{\widehat{\partial\overline{\theta}}}{\partial x_j}\right], \tag{15}$$

respectively, where $L_{ij} = \widehat{\overline{u_i}\,\overline{u_j}} - \widehat{\overline{u_i}}\,\widehat{\overline{u_j}}$ is the Leonard tensor, $L_\theta = \widehat{\overline{\theta}\,\overline{\theta}} - \widehat{\overline{\theta}}\,\widehat{\overline{\theta}}$, and the symbol $\widehat{(\,)}$ represents a test filtering operation with a filter size equal to $\widehat{\Delta} = 2\Delta$. The power α is usually set to $1/2$ although in numerical simulations of isotropic turbulence Chumakov [38] observed that the optimal value for α changes appreciably with the filter size.

Some new modelling strategies emerged recently where the viscous dissipation of SGS kinetic energy ε^Δ, is governed by an additional (new) transport equation (e.g. [21, 23, 41, 48, 49]). For instance, Schiestel and Dejoan [21], and Chaouat and Schiestel [41] developed the so-called *PITM* approach where a transport equation for ε^Δ is derived from the following relation (inspired by Equation (6)),

$$k_\mathrm{d} - k_\mathrm{c} = \zeta \frac{\varepsilon}{K_\mathrm{sgs}^{3/2}}, \tag{16}$$

where k_c is the implicit cut-off wave number associated with the LES filtering and k_d is a wave number in the dissipative region where the kinetic energy is negligible (ζ is a model constant).

Some models are based on the SGS mechanical-to-thermal time scale ratio

$$r_\mathrm{sgs} = \frac{K_\mathrm{sgs}/\varepsilon^\Delta}{\Theta_\mathrm{sgs}/\varepsilon_\theta^\Delta}, \tag{17}$$

which appears as a SGS version of the (total) mechanical-to-thermal time scale ratio defined as

$$r = \frac{K/\varepsilon}{\Theta/\varepsilon_\theta}, \tag{18}$$

where $K = (u_i)^2/2$ is the (total) kinetic energy and $\Theta = \theta^2/2$ is the (total) scalar variance. Note that there is now substantial evidence that, at least the mechanical-to-thermal time scale ratio defined in Equation (18) is not universal as attested by Overholt and Pope [32] in numerical simulations of isotropic turbulence.

In LES involving turbulent combustion some authors prefer to model the 'sub-filter scalar dissipation' term defined by $\gamma\overline{G_j G_j}$ since the term $\gamma\overline{G_j}\;\overline{G_j}$ in the definition of Σ_θ can be obtained explicitly from the filtered scalar fields e.g. [5, 28, 39, 40].

In particular Jiménez et al. [5] derived a new model for the sub-filter scalar dissipation based on Equation (17), and on the Smagorinsky [50] and the Yoshizawa [51] models. The model equation is

$$\gamma\overline{G_j G_j} = \frac{C_\theta^c}{2}\left(\frac{\Theta_{sgs}}{K_{sgs}}\right)\overline{\frac{\partial u_i}{\partial x_j}\frac{\partial u_i}{\partial x_j}}. \tag{19}$$

Tests in isotropic turbulence suggest that the model constant is approximately equal to $C_\theta^c \sim 1/Sc$. A similar model for the molecular SGS dissipation $\varepsilon_\theta^\Delta$ would be given by

$$\varepsilon_{\theta c}^\Delta = \frac{C_\theta^c}{2}\left(\frac{\Theta_{sgs}}{K_{sgs}}\right)\varepsilon^\Delta. \tag{20}$$

3. Direct numerical simulations of isotropic turbulence

3.1. *Numerical code and data bank description*

The numerical code used in the present simulations is a standard pseudo-spectral code in which the temporal advancement is made with an explicit third-order Runge–Kutta scheme. The physical domain consists in a periodic box of sides 2π and the simulations were fully dealiased using the 3/2 rule. Both the velocity and scalar large scales were forced in order to sustain the turbulence using the method described by Alvelius [52]. The same code was recently used by da Silva and Pereira [13, 30].

Three DNS of statistically steady (forced) homogeneous isotropic turbulence using $N = 192$ collocation points in each direction were carried out. The Taylor-based Reynolds number and Schmidt numbers for the three simulations are equal to $Re_\lambda = 95.6$ and $Sc = 0.7$; $Re_\lambda = 95.6$ and $Sc = 0.2$; and $Re_\lambda = 39.4$ and $Sc = 3.0$, respectively.

The ratio between the box size and the integral scale is $L/L_{11} > 4$ and we have $k_{\max}\eta > 1.5$ and $k_{\max}\eta_B > 1.5$ in all simulations, where $\eta = (\nu^3/\varepsilon)^{1/4}$ and $\eta_B = \eta/Sc^{1/2}$ are the Kolmogorov and Batchelor micro-scales, respectively. For the case $Re_\lambda = 95.6$ and $Sc = 0.7$ the velocity and scalar spectra display a $-5/3$ range which shows the existence of an inertial range region. Full details are given in [30].

The separation between grid and subgrid scales was made using a spatial filtering operation defined by the integral,

$$\overline{\phi}(\vec{x}) = \int_{-\Delta/2}^{+\Delta/2}\int_{-\Delta/2}^{+\Delta/2}\int_{-\Delta/2}^{+\Delta/2} \phi(\vec{x}')G_\Delta(\vec{x}-\vec{x}')\mathrm{d}\vec{x}', \tag{21}$$

where $\overline{\phi}(\vec{x})$ represents the spatially filtered variable $\phi(\vec{x})$, and $G_\Delta(\vec{x})$ is the filter kernel. Only box filtering is used in this work, whose filter kernel is defined by

$$G_\Delta(\vec{x}-\vec{\xi}) = \begin{cases} \dfrac{1}{\Delta}, \text{ if } |\vec{x}-\vec{\xi}| < \dfrac{\Delta}{2}, \\ 0, \quad \text{otherwise.} \end{cases}$$

Using the box and the Gaussian filters the results are practically independent of the filter type [30, 53, 54], while the use of the cut-off filter raises both theoretical and practical problems in the context of transport equations for LES (see Vreman et al. [55] and da Silva and Pereira [30]). Moreover, the box filter corresponds to the filter implicitly associated with the discretization using centred finite difference [56] or finite volume [1] codes, which are used more often in large-eddy simulations of engineering and geophysical flows.

Four different filter widths were used with $\Delta_m = m\Delta x$, with $m = 2, 4, 8, 16$. Their locations in the energy and scalar variance spectrum is shown in [30], where one can see that the implicit cut-off wave number for the filter with $\Delta/\Delta x = 16$ is within the inertial range region.

4. Analysis of the exact viscous and molecular SGS dissipations Σ and Σ_θ

In this section the 'real' or exact viscous and molecular SGS dissipations Σ and Σ_θ, respectively, are analysed using visualisations, correlation coefficients and probability density functions. All the results from this section were obtained using a single instantaneous field of the DNS with $Re_\lambda = 96$ and $Sc = 0.7$. For convenience these results were obtained in the DNS grid i.e. filtering without sampling was used in this section. It is well known that the absence of sampling tends

to slightly increase the correlation levels observed between variables, however the overall picture remains the same.

4.1. *Topology of the turbulent field: vorticity norm, Q and total dissipations of kinetic energy and scalar variance*

Before starting with the analysis of Σ and Σ_θ it is important to recall some of the well known 'topological properties' of turbulence using the present DNS of isotropic turbulence. The vorticity norm is given by $|\vec{\Omega}| = (\Omega_i \Omega_i)^{1/2}$, where Ω_i is the vorticity vector defined as the curl of the velocity $\Omega_i = \varepsilon_{ijk} \partial u_j / \mathrm{d}x_k$. In agreement with numerous works e.g. [57, 58], we observed that intense vorticity is concentrated in tube-like structures and also in some (less-frequent) sheet-like structures (not shown). These tube structures are commonly described as the 'worms' of homogeneous isotropic turbulence and have been the subject of much research since the pioneering work of Siggia [59].

The worms can also be observed using iso-surfaces of $Q > 0$, as in Figure 1(a), where Q is the second invariant of the velocity gradient tensor $A_{ij} = \partial u_i / \partial x_j$,

$$Q = \frac{1}{2} \left(\Omega_i \Omega_i - 2 S_{ij} S_{ij} \right), \tag{22}$$

and $S_{ij} = 1/2(\partial u_i / \partial x_j + \partial u_j / \partial x_i)$ is the rate-of-strain tensor. From its definition it follows that $Q > 0$ identifies flow regions where vorticity is higher than strain product, whereas $Q < 0$ is associated with regions of intense strain and comparatively low vorticity [60]. As in [61] the iso-surfaces of $Q > 0$ are dominated by tubular structures with few, if any, examples of the sheet-like structures that are present in the iso-surfaces of vorticity norm. On the other hand the iso-surfaces of $Q < 0$, which are shown in Figure 1(b) display a fragmentary sheet-like shape.

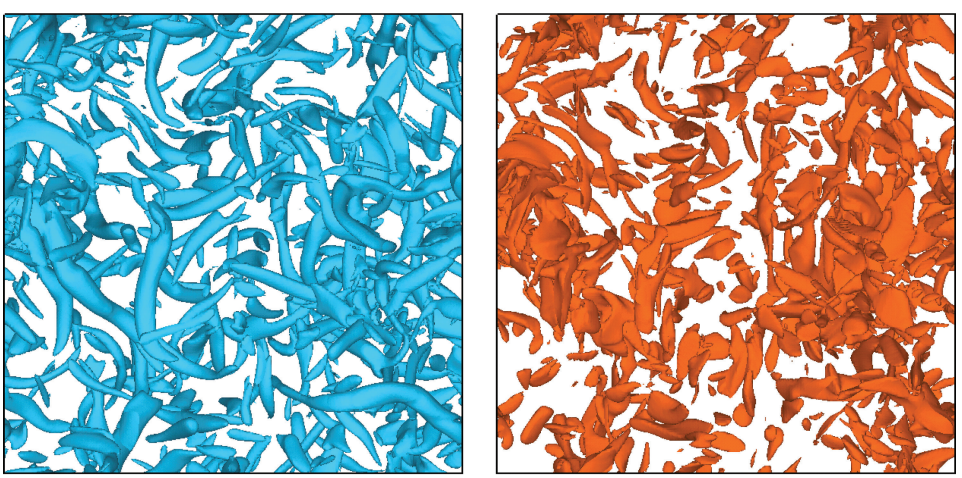

(a) (b)

Figure 1. Iso-surfaces of (a) $Q > 0$, and (b) $Q < 0$, where Q is the second invariant of the velocity gradient tensor for the DNS of isotropic turbulence with $Re_\lambda = 96$. The thresholds are $Q = 70$ and $Q = -60$, respectively.

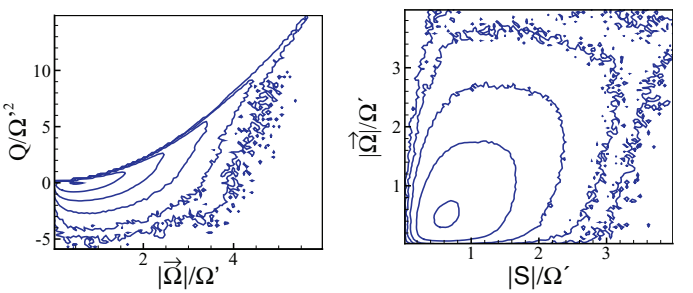

Figure 2. Joint probability density functions of (a) vorticity norm $|\vec{\Omega}|$ and Q and, (b) vorticity norm $|\vec{\Omega}|$ and strain rate norm $|S| = (2S_{ij}S_{ij})^{1/2}$. The PDFs are nomalised by $\Omega' = \langle \Omega_i \Omega_i \rangle^{1/2}$ and the contour lines are logarithmic and spaced by a factor of 10. The PDFs were obtained with a single instantaneous field for the DNS of isotropic turbulence with $Re_\lambda = 96$.

In agreement with this the joint probability density function of vorticity norm $|\vec{\Omega}|$ and Q displayed in Figure 2(a) shows that these quantities are strongly correlated for $Q > 0$, but not for $Q < 0$. The correlation coefficient between these two quantities was also computed using a single instantaneous field from the DNS with $Re_\lambda = 96$. The correlation coefficient between two variables u and v is defined by

$$\mathrm{Corr}(u, v) = \frac{< u'v' >}{\sqrt{< u'^2 >}\sqrt{< v'^2 >}}, \tag{23}$$

and we obtained $\mathrm{Corr}(|\vec{\Omega}|, Q) \approx 0.64$.

The joint PDF of vorticity norm $|\vec{\Omega}|$ and strain rate norm $|S| = (2S_{ij}S_{ij})^{1/2}$ shown in Figure 2(b) demonstrates that the correlation between strain and vorticity is low and exists mainly for strong values of both strain and vorticity (their correlation coefficient is $\mathrm{Corr}(|\vec{\Omega}|, |S|) \approx 0.45$). A similar joint PDF for these quantities was obtained by Jiménez et al. [57].

Finally, Figures 3(a) and (b) show iso-surfaces of the viscous and molecular dissipations of total kinetic energy ε and total scalar variance ε_θ, respectively. Both quantities exhibit a sheet-like structure, as shown in numerous previous works (e.g. [33, 34]). The sheet structure is less fragmentary for the scalar variance dissipation ε_θ, than for the kinetic energy dissipation ε, i.e. it seems that the sheets for ε_θ are 'thinner' than the sheets for ε. This is also in agreement with previous observations made by Vedula et al. [33]. Moreover, note that ε and ε_θ are very poorly correlated as attested by their correlation coefficient which is $\mathrm{Corr}(\varepsilon, \varepsilon_\theta) \approx 0.14$. The small correlation between ε and ε_θ was also observed in the numerical simulations of Overholt and Pope [32], Schumacher et al. [34] and Vedula et al. [33]. In particular, Vedula et al. [33] obtained 0.16 for the correlation coefficient between the logarithms of ε and ε_θ.

4.2. *Topology of the exact viscous and molecular SGS dissipations* Σ *and* Σ_θ

This section describes the topology of the 'real' or exact viscous dissipation of SGS kinetic energy Σ, and of the molecular dissipation of SGS scalar variance Σ_θ, respectively. Few works analysed in detail the topology of these quantities, in particular the molecular SGS dissipation Σ_θ, was seldom, if ever, analysed in this respect. On the other hand the topology of the viscous

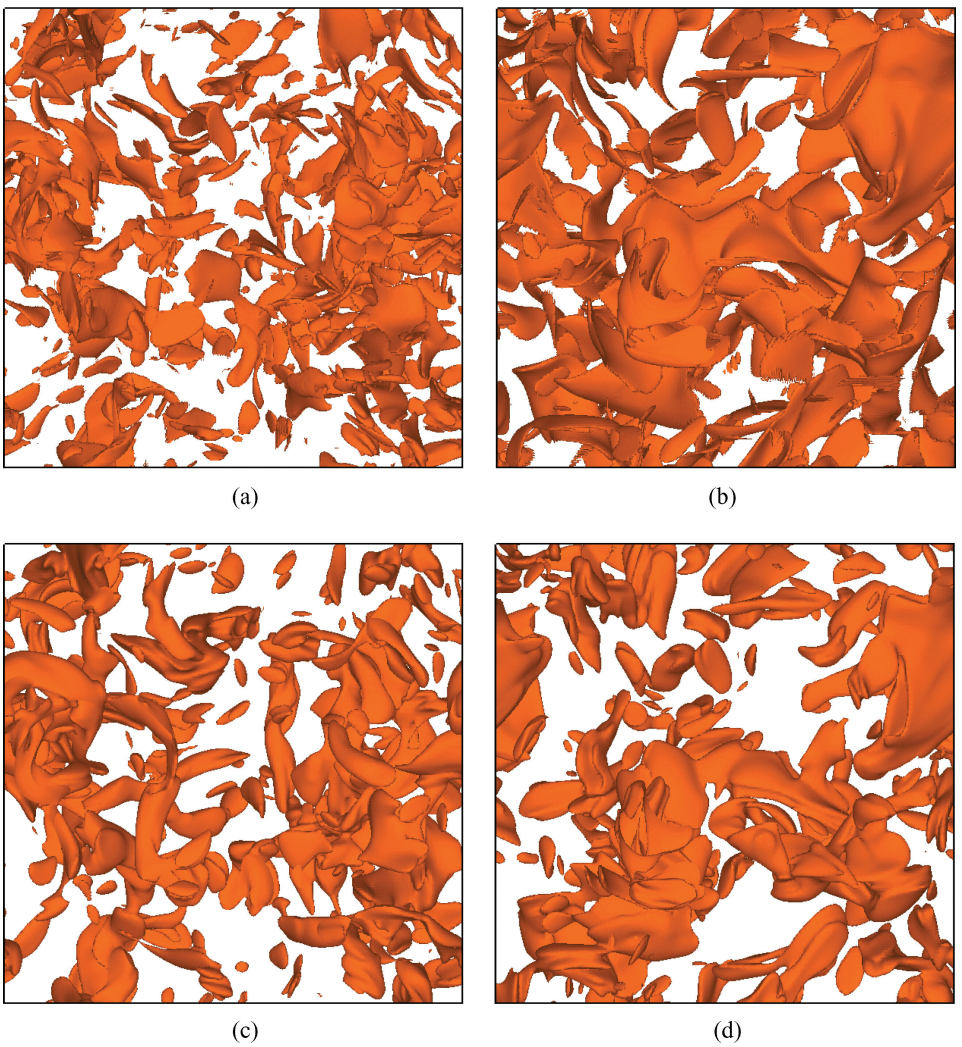

Figure 3. Iso-surfaces of (a) viscous dissipation rate of kinetic energy ε, (b) molecular dissipation rate of scalar variance ε_θ, (c) viscous dissipation rate of SGS kinetic energy Σ and, (d) molecular dissipation rate of SGS scalar variance Σ_θ. The visualisations were obtained for the DNS of isotropic turbulence with $Re_\lambda = 96$ and $Sc = 0.7$, and correspond to the same instant as in Figure 1. The molecular SGS dissipations were obtained with a filter width $\Delta/\Delta x = 8$, and the thresholds are: $\varepsilon/\langle\varepsilon\rangle = 3.7$; $\varepsilon_\theta/\langle\varepsilon_\theta\rangle = 4.8$; $\varepsilon^\Delta/\langle\varepsilon^\Delta\rangle = 2.8$ and; $\varepsilon_\theta^\Delta/\langle\varepsilon_\theta^\Delta\rangle = 3.1$.

SGS dissipation Σ, was already analysed before, although briefly, using DNSs of turbulent plane jets by da Silva and Métais [12].

Figures 3(c) and (d) show iso-surfaces of viscous SGS dissipation Σ, and molecular SGS dissipation Σ_θ, respectively, for filter width $\Delta/\Delta x = 8$. Starting with Σ we see that this variable has a sheet structure with some similarities with ε, particularly for the small-scale structures (compare Figures 3(a) and (c)). On the other hand, the large scales of Σ seem to have a tube-like structure which reminds the vorticity field (not shown) and also the field of $Q > 0$ (compare

Figures 2(a) and 3(c). Thus the topology of Σ seems to be characterised by a mixed tube/sheet structure.

To elucidate this point further we computed the correlation coefficients between Σ and $|\vec{\Omega}|$, and between Σ and ε. The correlation coefficient between $|\vec{\Omega}|$ and Σ increases with the filter size, from $\mathrm{Corr}(|\vec{\Omega}|, \Sigma) = 0.30$ for $\Delta/\Delta x = 2$ to about $\mathrm{Corr}(|\vec{\Omega}|, \Sigma) = 0.47$ for $\Delta/\Delta x = 16$. This is slightly less than the value of 0.65 observed by da Silva and Métais [12] for the correlation between the Σ and the field of fluctuating vorticity, which may be justified by the differences between the coherent structures in jets and in isotropic turbulence. The joint PDF between these two quantities for filter sizes equal to $\Delta/\Delta x = 2$ and $\Delta/\Delta x = 8$ are shown in Figure 4(a). No correlation can be seen to exist for the smaller filter size, while for $\Delta/\Delta x = 8$ it is difficult to see where from comes the (small) correlation existing between $|\vec{\Omega}|$ and Σ. It appears to be linked both with the intermediate and intense values from both variables.

On the other hand, we observed that the correlation coefficient between Σ and ε does not change appreciably with the filter size and is about $\mathrm{Corr}(\varepsilon, \Sigma) \approx 0.50$–$0.60$. The joint PDF between Σ and ε is shown in Figure 4(b) for $\Delta/\Delta x = 2$ and $\Delta/\Delta x = 8$. Here we see that the correlation between Σ and ε comes mainly from the small (and more frequent) values of these quantities. Thus we conclude that the viscous SGS dissipation Σ has a mixed tube/sheet structure, where the tube structures are associated with medium and intense values of vorticity norm, while the sheet structures are associated with small and medium values of kinetic energy dissipation rate.

At this point it is noteworthy to say something about the differences between ε and Σ. For isotropic turbulence at sufficiently high-Reynolds number and considering an implicit filter placed at the inertial range region $\langle\Sigma\rangle = \langle\varepsilon\rangle$, as observed by da Silva and Pereira [13], however the statistical and topological nature of these quantities is somehow different. A first indication of this fact is given by Figure 4(b) and by $\mathrm{Corr}(\Sigma, \varepsilon) \approx 0.60$.

The viscous SGS dissipation is given by $\Sigma = \nu[\overline{\frac{\partial u_i}{\partial x_j}\frac{\partial u_i}{\partial x_j}} - \frac{\partial \overline{u_i}}{\partial x_j}\frac{\partial \overline{u_i}}{\partial x_j}]$. Now, $\nu\frac{\partial \overline{u_i}}{\partial x_j}\frac{\partial \overline{u_i}}{\partial x_j}$ represents the viscous dissipation affecting the evolution of the resolved scales of motion [12]. Therefore, for high-Reynolds number the second term in the definition of Σ is of course much smaller than the first term, and the viscous SGS dissipation is $\Sigma \sim \nu\overline{\frac{\partial u_i}{\partial x_j}\frac{\partial u_i}{\partial x_j}}$. This reminds the pseudo-dissipation $\varepsilon_0 = \nu\frac{\partial u_i}{\partial x_j}\frac{\partial u_i}{\partial x_j}$, and since both $\overline{\frac{\partial u_i}{\partial x_j}\frac{\partial u_i}{\partial x_j}}$ and $\frac{\partial u_i}{\partial x_j}\frac{\partial u_i}{\partial x_j}$ are clearly dominated by similar (small) scales

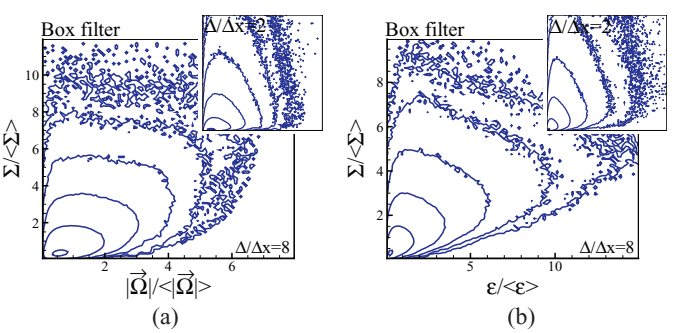

Figure 4. Joint probability density functions of (a) vorticity norm $|\vec{\Omega}|$ and SGS kinetic energy viscous dissipation Σ, and (b) kinetic energy viscous dissipation rate ε and SGS kinetic energy viscous dissipation Σ. The PDFs were obtained with a single instantaneous field for the DNS of isotropic turbulence with $Re_\lambda = 96$ and filter widths $\Delta/\Delta x = 2$ and 8.

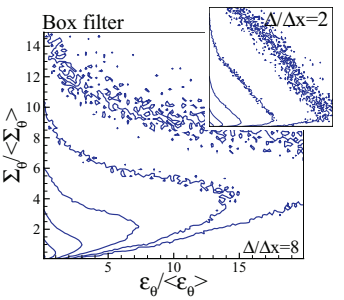

Figure 5. Joint probability density function of scalar fluctuations molecular dissipation rate ε_θ and SGS scalar fluctuations molecular dissipation Σ_θ.

of motion, arguably much smaller than the implicit cut-off scale from the LES filter, we expect the nature of Σ to be somehow closer to ε_0 than to ε. These aspects should be investigated in a future study.

For the molecular SGS dissipation Σ_θ the visualisations displayed in Figure 3(d) show a predominance of sheet-like structures. As with ε and ε_θ the visualisations show that the sheets for Σ_θ are 'thinner' than the sheets for Σ, and again the two quantities are very poorly correlated as attested by their correlation coefficient. We obtained $\mathrm{Corr}(\Sigma, \Sigma_\theta) \approx 0.14$ irrespective of the filter size. Moreover, there is almost no correlation between Σ_θ and either $|\vec{\Omega}|$ or ε: both $\mathrm{Corr}(|\vec{\Omega}|, \Sigma_\theta)$ or $\mathrm{Corr}(\varepsilon, \Sigma_\theta)$ are always smaller than 20% for $\Delta/\Delta x = 2$–16. There is however, some correlation with ε_θ, since we obtain $\mathrm{Corr}(\varepsilon_\theta, \Sigma_\theta) \approx 0.50$ for large filter widths. This result can also be understood from the joint PDF of ε_θ and Σ_θ which is displayed in Figure 5 for $\Delta/\Delta x = 2$ and 8. Again, no correlation can be observed for $\Delta/\Delta x = 2$, but for $\Delta/\Delta x = 8$ the existing correlation comes from medium to intense values of both quantities. Thus we conclude that Σ_θ has a

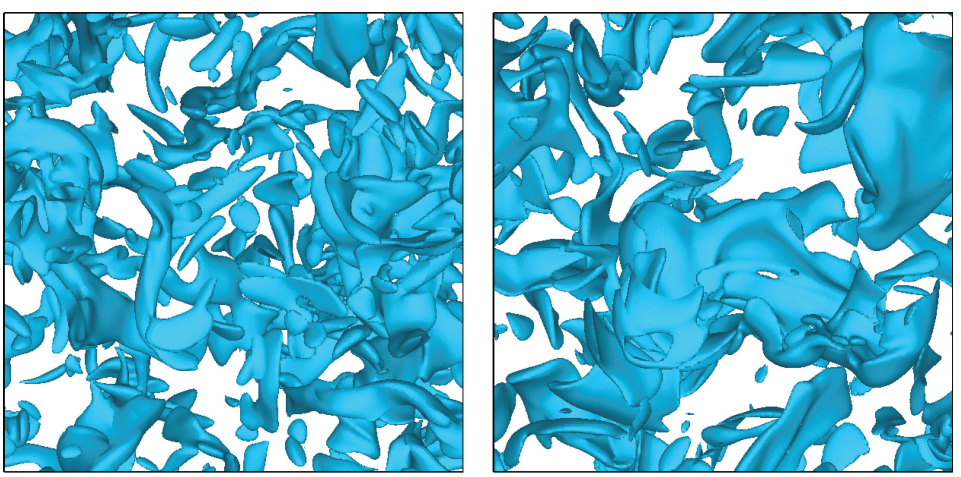

(a) (b)

Figure 6. Iso-surfaces of (a) SGS kinetic energy $\tau_{ii}/2$, and (b) SGS scalar fluctuations q_θ, for the DNS of isotropic turbulence with $Re_\lambda = 96$ and $Sc = 0.7$ and filter width $\Delta/\Delta x = 8$. The visualisations correspond to the same instant as in Figure 1 and the thresholds are: $\tau_{ii}/\langle\tau_{ii}\rangle = 2.3$ and; $q_\theta/\langle q_\theta\rangle = 3.2$.

Table 1. Summary of the spatial localisation results for the viscous and molecular SGS dissipations Σ and Σ_θ, respectively, for the simulation with $Re_\lambda = 95.6$ and $Sc = 0.7$.

Correlation	Σ	Σ_θ
$\|\vec{\Omega}\|$; $Q \geq 0$ (tube-like structure)	Yes	No
ε; $Q \leq 0$ (sheet-like structure)	Yes	No
ε_θ (sheet-like structure)	No	Yes

sheet-like structure with some, although not strong, similarity with ε_θ. Table 4.1 summarises these results.

An interesting issue to analyse which is closely linked with the main focus of this work concerns the topology of the regions of concentrated SGS kinetic energy τ_{ii} and SGS scalar variance q_θ. Indeed, Equation (6) supposes the existence of a strong level of correlation between Σ and τ_{ii}. Similarly, Equation (7) also implies a strong correlation between Σ_θ and both τ_{ii} and q_θ. Note that there is virtually no correlation between τ_{ii} and q_θ: we obtained $\mathrm{Corr}(\tau_{ii}, q_\theta) \approx 0.06$ irrespective of the filter size. Concerning the topology of the SGS kinetic energy τ_{ii} da Silva and Métais [12] showed that intense values of this quantity are located at the centre of the flow coherent vortices in the far field of turbulent plane jets. It is interesting to see whether this result is confirmed in the present data and also to see if this result is affected by changes in the filter size.

Figures 6(a) and (b) show iso-surfaces of τ_{ii} and q_θ, respectively, for $\Delta/\Delta x = 8$. For the SGS kinetic energy τ_{ii} (Figure 6(a)) the resemblance with the iso-surfaces of vorticity norm is striking (not shown). The same is true, although maybe to a lesser extent, between the fields of τ_{ii} and $Q > 0$ (compare Figures 1(a) and 6(a)). Thus it seems that τ_{ii} has a mixed tube/sheet structure where the tube structures dominate.

In order to investigate this issue we analysed the influence of the filter size in the level of correlation between $|\vec{\Omega}|$ and τ_{ii}: we obtain $\mathrm{Corr}(|\vec{\Omega}|, \tau_{ii}) = 0.82$, 0.83, 0.79 and 0.62, for filter widths equal to $\Delta/\Delta x = 2$, 4, 8 and 16, respectively, i.e. the correlation decreases slightly with the filter size, but remains always very high. Recall that da Silva and Métais obtained $\mathrm{Corr}(|\vec{\Omega}|, \tau_{ii}) = 0.74$ in turbulent plane jets. The joint PDF between τ_{ii} and $|\vec{\Omega}|$ is shown in Figure 7(a), for filter widths $\Delta/\Delta x = 2$ and $\Delta/\Delta x = 8$. The contour lines of the joint PDFs show that the correlation is obtained for all values of both quantities. However we observed that part of the intense SGS kinetic energy is also to be found in the sheet region surrounding the intense vorticity structures, as attested by the correlation coefficient between τ_{ii} and ε. Indeed we have $\mathrm{Corr}(\varepsilon, \tau_{ii}) = 0.76$, 0.75, 0.68 and 0.55, for filter widths equal to $\Delta/\Delta x = 2$, 4, 8 and 16, respectively. Consistently with this the joint PDFs between ε and τ_{ii} displayed in Figure 7(b) show that τ_{ii} is associated with the sheet regions defined by ε mainly for small and intermediate values of ε and τ_{ii} i.e. for the most intense values of these quantities there is no clear correlation between them. In conclusion, we see that the SGS kinetic energy τ_{ii} tends to be associated both with the regions of high vorticity norm, in the form of tubes, as with the regions of high-kinetic energy dissipation, in the form of sheets. However, the correlation with the tubes is higher.

Concerning the scalar field Figure 6(b) shows that the SGS scalar variance q_θ is clearly sheet like. Again we remark that the sheet structures associated with scalar field quantities, i.e. q_θ and Σ_θ, are quite different from the sheet-like structure associated with the velocity field, i.e. τ_{ii} and Σ. In particular, the area of the iso-surfaces seems to be much higher, for a similar given thickness. Furthermore, we observed that there is no correlation between q_θ with either the vorticity norm $|\vec{\Omega}|$ or the viscous dissipation of kinetic energy ε: $\mathrm{Corr}(|\vec{\Omega}|, q_\theta) \approx 0.02$ and $\mathrm{Corr}(\varepsilon, q_\theta) \approx 0.01$.

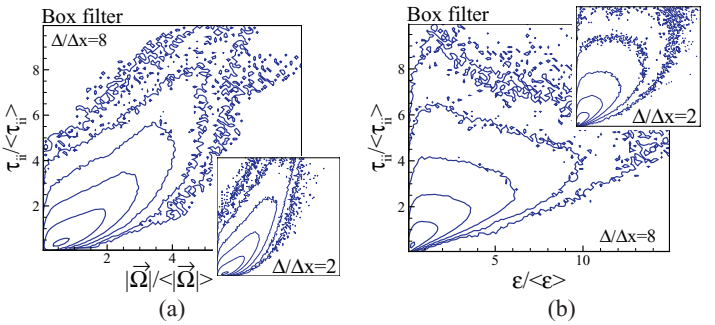

Figure 7. Joint probability density functions of (a) vorticity norm $|\vec{\Omega}|$ and SGS kinetic energy $\tau_{ii}/2$, and (b) viscous dissipation rate of kinetic energy ε and SGS kinetic energy $\tau_{ii}/2$. The PDFs were obtained with a single instantaneous field for the DNS of isotropic turbulence with $Re_\lambda = 96$ and filter widths $\Delta/\Delta x = 2$ and 8.

However, a very strong correlation exists with the scalar variance dissipation rate ε_θ, since we obtain $\mathrm{Corr}(\varepsilon_\theta, q_\theta) = 0.94$, 0.93, 0.83 and 0.60, for filter widths equal to $\Delta/\Delta x = 2$, 4, 8 and 16, respectively. Finally, Figure 8 displays the joint PDF between ε_θ and q_θ, for $\Delta/\Delta x = 2$ and 8, where we see that the strong correlation between these variables exists for all range of their values. Table 2 summarises these results.

To end this section we analyse quantities which are directly linked to the classical models used for Σ and Σ_θ defined in Equations (6) and (7). The previous results showed that regions of strong viscous SGS dissipation Σ are associated with both the tube regions where the vorticity norm is concentrated, as with the sheet regions where the most intense viscous dissipation of kinetic energy takes place (see Figures 4(a) and (b)). On the other hand, regions of strong SGS kinetic energy also tend to be concentrated inside the vortex tubes, as well as in the sheet regions defined by strong viscous dissipation of kinetic energy ε (see Figures 7(a) and (b)). It is therefore expected to find a good correlation between Σ and τ_{ii} as required by the model dissipation defined in Equation (6).

To analyse this, Figure 9(a) shows the joint PDF of Σ and τ_{ii} for the simulation with $Re_\lambda = 95.6$ and filter widths $\Delta/\Delta x = 2$ and 8. As can be seen for $\Delta/\Delta x = 8$ the two quantities

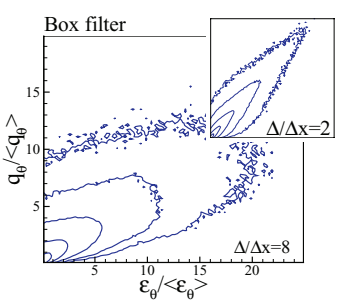

Figure 8. Joint probability density functions of scalar variance molecular dissipation ε_θ and SGS scalar variance q_θ. The PDFs were obtained with a single instantaneous field for the DNS of isotropic turbulence with $Re_\lambda = 96$ and $Sc = 0.7$, and filter widths $\Delta/\Delta x = 2$ and 8.

Table 2. Summary of the spatial localisation results for the SGS kinetic energy and SGS scalar variance τ_{ii} and q_θ, respectively, for the simulation with $Re_\lambda = 95.6$ and $Sc = 0.7$.

Correlation	τ_{ii}	q_θ
$\|\vec{\Omega}\|$; $Q \geq 0$ (tube like-structure)	Yes	No
ε; $Q \leq 0$ (sheet-like structure)	Yes	No
ε_θ (sheet-like structure)	No	Yes

are strongly correlated for all the range of their values, while for $\Delta/\Delta x = 2$ this correlation seems to be non-existent. The correlation coefficients obtained support this idea with $\mathrm{Corr}(\Sigma, \tau_{ii}) = 0.43$, 0.54, 0.65 and 0.73 for $\Delta/\Delta x = 2$, 4, 8 and 16, respectively, i.e. the level of the correlation increases with the filter size. Since the SGS models involving a transport equation for τ_{ii} are likely to be used with coarse meshes the relatively low level of correlation obtained between Σ and τ_{ii} for small filter sizes is not relevant. However, the fact that $\mathrm{Corr}(\Sigma, \tau_{ii})$ is high for large filter sizes does seem promising for the classical model defined in Equation (6). Note that the existence of a strong correlation between Σ and τ_{ii} had already been observed in an experimental plane wake by Meneveau and O'Neil [36] and in a DNS of a turbulent plane jet by da Silva and Métais [12]. Here we show that this correlation increases with the filter size Δ and is actually quite low for small values of Δ. Moreover, we show that $\mathrm{Corr}(\Sigma, \tau_{ii})$ is connected with the presence of regions of concentrated vorticity i.e. the vortex tubes, as well as with the sheet region associated with intense viscous dissipation of kinetic energy ε.

It is interesting to see whether something similar occurs between Σ_θ and q_θ. Recalling the previous results we saw that regions of intense molecular SGS dissipation Σ_θ tend to form in the sheet region associated with the molecular dissipation of total scalar variance ε_θ (see Figure 5). Furthermore, we also observed that the most intense values of SGS scalar variance q_θ also lie in the sheet region associated with ε_θ (see Figure 8). Therefore, one would be tempted to also infer that $\mathrm{Corr}(\Sigma_\theta, q_\theta)$ is high.

Figure 9(b) shows the joint PDF between Σ_θ and q_θ for the simulation with $Re_\lambda = 95.6$, $Sc = 0.7$ and filter sizes $\Delta/\Delta x = 2$ and 8. As expected we see that the two quantities are strongly correlated for all their values for large filter sizes. Again, no correlation can be observed for $\Delta/\Delta x = 2$. We computed the correlation coefficients for these variables and obtained $\mathrm{Corr}(\Sigma_\theta, q_\theta) = 0.37$, 0.52, 0.68 and 0.77 for increasing filter sizes, respectively. Thus we conclude that Σ_θ and q_θ are well correlated and attain their most intense values in the sheet region associated with high values of molecular dissipation of (total) scalar variance ε_θ. Thus we conclude that for large filter sizes, which are important for LES based on transport equations, both $\mathrm{Corr}(\Sigma, \tau_{ii})$ and $\mathrm{Corr}(\Sigma_\theta, q_\theta)$ are high, as required by the classical models.

This ends the assessment of the topology of the relevant terms for the dynamics of the 'real' or exact molecular dissipations of SGS kinetic energy Σ and SGS scalar variance Σ_θ. In the following section, we assess the performance of several models used for these quantities.

5. Assessment of models for the viscous/molecular dissipation of SGS kinetic energy and SGS scalar gradient, $\boldsymbol{\varepsilon^\Delta}$ and $\boldsymbol{\varepsilon_\theta^\Delta}$

Having made an analysis of the spatial localisation and topology of the 'real' or exact SGS kinetic energy and SGS scalar variance viscous/molecular dissipations (Σ and Σ_θ) in the previous section, we now proceed into the analysis of some models for these terms using classical *a priori* tests. In

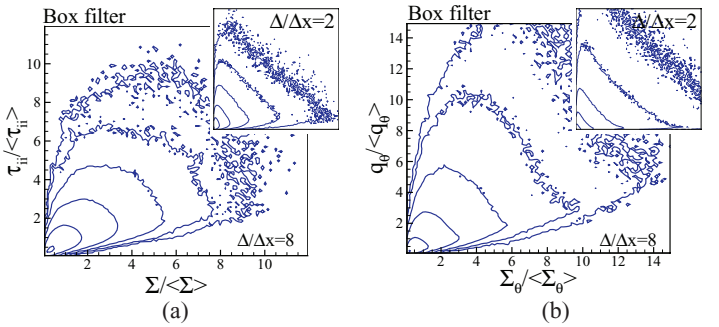

Figure 9. Joint probability density functions of (a) viscous SGS dissipation Σ and SGS kinetic energy $\tau_{ii}/2$, and (b) molecular SGS dissipation Σ_θ and SGS scalar variance q_θ. The PDFs were obtained with a single instantaneous field for the DNS of isotropic turbulence with $Re_\lambda = 96$, $Sc = 0.7$ and filter widths $\Delta/\Delta x = 2$ and 8.

recent years the limitations of *a priori* tests have been recognised e.g. [8]. However, these tests are still regarded as an important tool to assess the physical hypothesis behind the existing SGS models. The goal here is to assess several models for the molecular SGS dissipation terms.

The exact or 'real' viscous/molecular dissipations of SGS kinetic energy and SGS scalar variance are defined in Equations (1) and (2), respectively, while we denote by ε_m^Δ and $\varepsilon_{\theta m}^\Delta$ the modelled values of these quantities using a given model m. Three models were analysed here which we denote by $m = a, b, c$. The symbol $m = a$ represents the classical models defined in Equations (6) and (7). The new models used in hybrid RANS/LES defined by Equations (12) and (13) are denoted by $m = b$. Finally, we also analyse the model proposed by Jiménez et al. [5] for the molecular dissipation of SGS scalar variance $\varepsilon_{\theta c}^\Delta$.

Note that unlike in the previous section, all the *a priori* tests carried out here were made with the data in the LES grid i.e. both filtering and sampling were used. The results were obtained using several (10) instantaneous fields from the three DNS described before and also used in da Silva and Pereira [13, 30] i.e. with (i) $Re_\lambda = 39.4$ and $Sc = 3.0$, (ii) $Re_\lambda = 95.6$ and $Sc = 0.7$ and (iii) $Re_\lambda = 95.6$ and $Sc = 0.2$. Moreover, note that in order to conduct the *a priori* tests the constants appearing in the equations defining each model e.g. Equations (6) and (7) for the classical model, were set to $C_\varepsilon^a = 1$ and $C_{\varepsilon\theta}^a = 1$, respectively, before being evaluated from the data.

5.1. *Analysis of the classical models ε_a^Δ and $\varepsilon_{\theta a}^\Delta$*

In this section using classical *a priori* tests we analyse the results for the classical model for the viscous/molecular dissipation of SGS kinetic energy and SGS scalar variance ε_a^Δ and $\varepsilon_{\theta a}^\Delta$, defined in Equations (6) and (7), respectively. We look into correlations, joint probability density functions, classical one-point statistics and spectra from the exact and modelled quantities.

5.1.1. *Correlation coefficients and joint probability density functions*

Figure 10 shows the correlation coefficients between the exact and the modelled viscous/molecular SGS dissipations—Corr($\Sigma, \varepsilon_a^\Delta$) and Corr($\Sigma_\theta, \varepsilon_{\theta a}^\Delta$)—as functions of the filter size, for all the simulations used in this work. For small filter sizes, characteristic of the dissipative range, the correlations between Σ and ε_a^Δ, and between Σ_θ and $\varepsilon_{\theta a}^\Delta$ are low or moderate: we have

$\mathrm{Corr}(\Sigma, \varepsilon_a^\Delta) = 0.40$, and $\mathrm{Corr}(\Sigma_\theta, \varepsilon_{\theta a}^\Delta) = 0.50$ for $Re_\lambda = 95.6$, $Sc = 0.7$ and $\Delta/\Delta x = 2$. However, all the correlations increase with the filter size and become actually very high for large i.e. inertial range filter sizes: for the simulation with $Re_\lambda = 95.6$ and $Sc = 0.7$ the correlations are $\mathrm{Corr}(\Sigma, \varepsilon_a^\Delta) = 0.85$ and $\mathrm{Corr}(\Sigma_\theta, \varepsilon_{\theta a}^\Delta) = 0.82$ for $\Delta/\Delta x = 16$. An encouraging result which is apparent from the figure is that the correlations tend to be higher for higher Reynolds numbers.

The high correlation observed between the exact and modelled viscous SGS dissipation (Σ and ε_a^Δ) agrees with the results obtained in Section 4.2, where the *a priori* tests were made without sampling. Moreover, we confirm here the trend previously observed of increasing correlation with increasing filter size.

Concerning the scalar field we see here for the first time that the correlation between the exact and modelled molecular SGS dissipation (Σ_θ and $\varepsilon_{\theta a}^\Delta$) is also quite high. At first glance this result seems a bit surprising. Recall that in Section 4.2 it was observed that Σ_θ and q_θ are also strongly correlated, however the classical model defined by Equation (7) assumes that $\Sigma_\theta \propto K_{\mathrm{sgs}}^{1/2}\Theta_{\mathrm{sgs}}$, i.e. $\Sigma_\theta \propto \tau_{ii}^{1/2} q_\theta$, and as described before τ_{ii} and q_θ are not correlated at all. Indeed, the most intense SGS scalar variance q_θ, like the most intense molecular SGS dissipation Σ_θ, were observed to lie in the sheet region associated with high dissipation of (total) scalar variance ε_θ, whereas the SGS kinetic energy $\tau_{ii}/2$ tends to be stronger in regions dominated by the presence of vortex tubes i.e. with no correlation with the sheet regions associated with the scalar field. Thus one might suppose that the presence of $K_{\mathrm{sgs}}^{1/2}$ in Equation (7) would decrease the correlation between Σ_θ and $K_{\mathrm{sgs}}^{1/2}\Theta_{\mathrm{sgs}}$, as compared to the correlation between Σ and $K_{\mathrm{sgs}}^{3/2}$. However, this is not the case since, as can be seen from the present results, the presence of the term $K_{\mathrm{sgs}}^{1/2}$ in Equation (7) does not degrade the correlation level between both sides of Equation (7).

To have a more detailed picture the results described above Figures 11(a) and (b) show the joint probability density functions between Σ and ε_a^Δ, and between Σ_θ and $\varepsilon_{\theta a}^\Delta$, for the simulation with $Re_\lambda = 95.6$ and $Sc = 0.7$, and filter widths $\Delta/\Delta x = 4$ and $\Delta/\Delta x = 16$. For the smaller filter no correlation can be observed from the shape of the joint PDFs between both Σ and ε_a^Δ, and between Σ_θ and $\varepsilon_{\theta a}^\Delta$. However, in agreement with the correlation coefficients described above, for $\Delta/\Delta x = 16$ one observes a strong correlation between the variables. Moreover, we see that this strong correlation comes from all the range of values of the variables. Similar results were observed for the simulations with $Re_\lambda = 95.6$ and $Sc = 0.2$, and for $Re_\lambda = 39.4$ and $Sc = 3.0$.

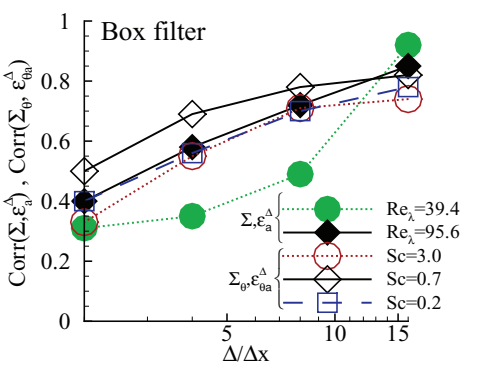

Figure 10. Correlation coefficients between the exact molecular SGS dissipations (Σ and Σ_θ) and their classical models (ε_a^Δ and $\varepsilon_{\theta a}^\Delta$) defined by Equations (6) and (7). The correlations were obtained with filter widths $\Delta/\Delta x = 2$, 4, 8, and 16, and were computed using the data in the LES mesh *i.e.* both filtering and sampling were used in the *a-priori* tests.

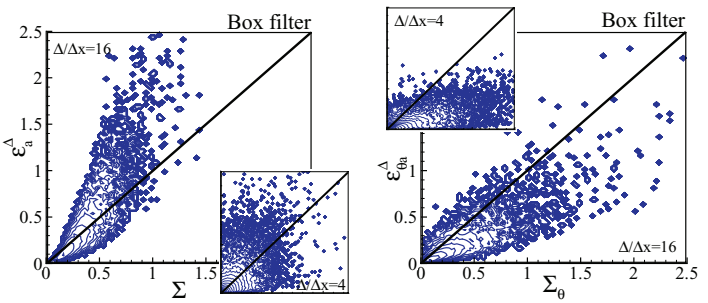

Figure 11. Joint PDFs between (a) the exact (Σ) and modelled (ε_a^Δ) viscous SGS dissipation and; (b) between the exact (Σ_θ) and modelled ($\varepsilon_{\theta a}^\Delta$) molecular SGS dissipation, for the simulations with $Re_\lambda = 95.6$, and $Sc = 0.7$, and for filter widths $\Delta/\Delta x = 4$ and $\Delta/\Delta x = 16$. The classical models for the molecular SGS dissipations ε_a^Δ and $\varepsilon_{\theta a}^\Delta$ are given by equations (6) and (7), respectively.

To conclude, the analysis of the joint PDFs confirms the previous results in terms of the correlation coefficients i.e. for the classical models for the molecular dissipation of SGS kinetic energy ε_a^Δ, and SGS scalar variance $\varepsilon_{\theta a}^\Delta$ defined in Equations (6) and (7), respectively, the results indicate that in terms of spatial localisation these models give good results, particularly for large filter sizes. It is important to proceed into the detailed characterisation of the statistical behaviour of the models which can be analysed through several one-point statistics. This is the subject of the following section.

5.1.2. *Constants C_ε^a and $C_{\varepsilon\theta}^a$*

Before analysing the behaviour of high order moments of Σ, Σ_θ, ε_a^Δ and $\varepsilon_{\theta a}^\Delta$ it is important to analyse the dependence of the Reynolds and Schmidt numbers and of the implicit filter size on the mean values of these quantities. Note that, as shown in da Silva and Pereira [13] for $Re_\lambda = 95.6$ and $Sc = 0.7$, as the filter size tends to the inertial range $\Delta/\Delta x \to 16$, the ratio of the mean SGS production and total viscous/molecular dissipation tends to a plateau where the *global equilibrium assumption* holds [12, 62] i.e. both $\langle P \rangle / \langle \varepsilon \rangle \to 1$ and $\langle P_\theta \rangle / \langle \varepsilon_\theta \rangle \to 1$.

Similarly, to observe the dependence the mean values of Σ and Σ_θ on Re_λ, Sc, and Δ we analyse the evolution of the model constants C_ε^a and $C_{\varepsilon\theta}^a$ defined in Equations (6) and (7). These can be computed from the present data with the following equations,

$$\left\langle C_\varepsilon^a \right\rangle = \left\langle \nu \left[\overline{\frac{\partial u_i}{\partial x_j} \frac{\partial u_i}{\partial x_j}} - \frac{\partial \overline{u_i}}{\partial x_j} \frac{\partial \overline{u_i}}{\partial x_j} \right] \right\rangle \Bigg/ \left\langle \frac{K_{\mathrm{sgs}}^{3/2}}{\Delta} \right\rangle, \tag{24}$$

and

$$\left\langle C_{\varepsilon\theta}^a \right\rangle = \left\langle \gamma \left[\overline{G_j G_j} - \overline{G_j}\, \overline{G_j} \right] \right\rangle \Bigg/ \left\langle \frac{K_{\mathrm{sgs}}^{1/2} \Theta_{\mathrm{sgs}}}{\Delta} \right\rangle, \tag{25}$$

where we took $K_{sgs} = \tau_{ii}/2$, and $\Theta_{sgs} = q_\theta/2$.

Figure 12 displays $\langle C_\varepsilon^a \rangle$ and $\langle C_{\varepsilon\theta}^a \rangle$ obtained with the above equations for all the simulations and filter sizes used in this work. For $Re_\lambda = 95.6$ and $Sc = 0.7$ the constant $C_{\varepsilon\theta}^a$ associated

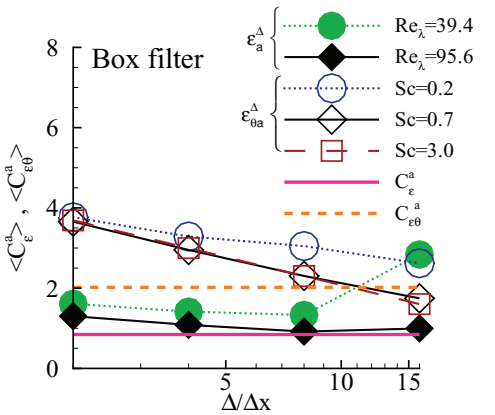

Figure 12. Constants C^a_ε and $C^a_{\varepsilon\theta}$ defined in Equations (6) and (7), respectively, for all the simulations and filter sizes used in the present work. The constants were computed with equations (24) and (25). The theoretical values for C^a_ε and $C^a_{\varepsilon\theta}$ given by Equations (10) and (11), respectively, are also shown in the figure.

with the scalar field displays a slightly larger variation with the filter size than the constant C^a_ε associated with the velocity field: we have $0.995 < C^a_\varepsilon < 1.301$ against $1.746 < C^a_{\varepsilon\theta} < 3.657$. In particular the constant C^a_ε is higher for the smaller Reynolds number case, in agreement with Menon et al. [37] who analysed the value of C^a_ε in direct numerical simulations of decaying isotropic turbulence.

Table 3 lists the values of C^a_ε and $C^a_{\varepsilon\theta}$ used in several previous works. For the constant C^a_ε values between $0.84 < C^a_\varepsilon < 1.9$ have been used in the literature. Note that the present values of $C^a_\varepsilon = 0.995$ and $C^a_{\varepsilon\theta} = 1.746$ for $Re_\lambda = 95.6$ and $\Delta/\Delta x = 16$ (inertial range), are very close to the theoretical values of $C^a_\varepsilon = 0.845$ and $C^a_{\varepsilon\theta} = 2.02$ given by Equations (10) and (11), respectively, and are also well within the values used in previous works.

Despite its Reynolds and Schmidt number dependence, for the higher Reynolds number case the constants C^a_ε and $C^a_{\varepsilon\theta}$ seem to display an asymptotic behaviour, and tend to the theoretical values as the filter size increases. Therefore, as a first approximation for geophysical or engineering applications i.e. for high-Reynolds numbers and coarse meshes, the use of a single (constant) value for C^a_ε and $C^a_{\varepsilon\theta}$, given by Equations (10) and (11), respectively, instead of using a dynamic procedure as done by Ghosal et al. [6], seems justifiable. For other situations e.g. for small-Reynolds numbers and/or finer to intermediate grids the use of the dynamic procedure for the computation of C^a_ε is supported by the data since this procedure assumes that the constant is equal at two consecutive filter widths.

The computation of $C^\Delta_{\varepsilon\theta}$ is more difficult to reconcile with this assumption since the results seem to show a linear dependence of $C^\Delta_{\varepsilon\theta}$ from the filter size. Thus, even if the variation of $C^\Delta_{\varepsilon\theta}$ with the filter size is rather small, the application of the dynamic procedure for the computation of $C^\Delta_{\varepsilon\theta}$ should be used with care since the present results indicate that the use of the dynamic procedure might not be correct here. The problem of the determination of the model constant $C^\Delta_{\varepsilon\theta}$ is complex [38, 42, 43] and should be pursued in another work.

5.1.3. *One-point statistics: variance, skewness and flatness*

The variance, skewness and flatness of the viscous and molecular SGS dissipation terms are analysed now. The variance of a given quantity expresses its local 'intensity' and therefore is

Table 3. Constants C_ε^a and $C_{\varepsilon\theta}^a$ from Equations (6) and (7), respectively, used in several works. '(dyn.)' means that either the "dynamic procedure" of Germano et al. [66] or some other relation based on it was used to obtain the model constant, and '(equ.)' means that an additional transport equation is used to compute the molecular SGS dissipation rate. The values shown as 'Present work' correspond to the DNS with $Re_\lambda = 95.6$, $Sc = 0.7$ and filter size $\Delta/\Delta x = 16$.

Source	C_ε^a	$C_{\varepsilon\theta}^a$
Schumann [1]	0.845	–
Yoshizawa [2]	1.900	–
Yoshizawa [51]	0.910	–
Yoshizawa and Horiuti [15]	1.000	–
Schmidt and Schumann [14]	0.845	2.020
Wong [17]	(dyn.)	–
Ghosal et al. [6]	(dyn.)	–
Fureby et al. [67]	1.050	–
Hamba [68, 69]	1.640	–
Dejoan and Schiestel [18]	0.850	–
Schiestel and Dejoan [21]	(equ.)	–
Langhe et al. [23]	(equ.)	–
Kajishima and Nomachi [25]	0.835	–
Horiuti [16]	1.000	–
Davidson and Peng [22]	1.050	–
Krajnović and Davidson [20]	(dyn.)	–
Present work	0.995	1.746

useful in order to characterise the local 'activity' of the SGS dissipation terms. The variance of the exact (Σ and Σ_θ) and modelled (ε_a^Δ and $\varepsilon_{\theta a}^\Delta$) molecular SGS dissipations are shown in Figures 13(a) and (b). As can be seen the exact and modelled variances increase with the filter size, implying that the classical models get the correct trend, which reflects the increasing importance of the molecular SGS dissipation terms when more SGS production—P and P_θ—contribute to it as the filter size increases. Comparing Σ and ε_a^Δ (Figure 13(a)) we see that the agreement between the two curves is quite good, particularly for the lower-Reynolds number case. A similar

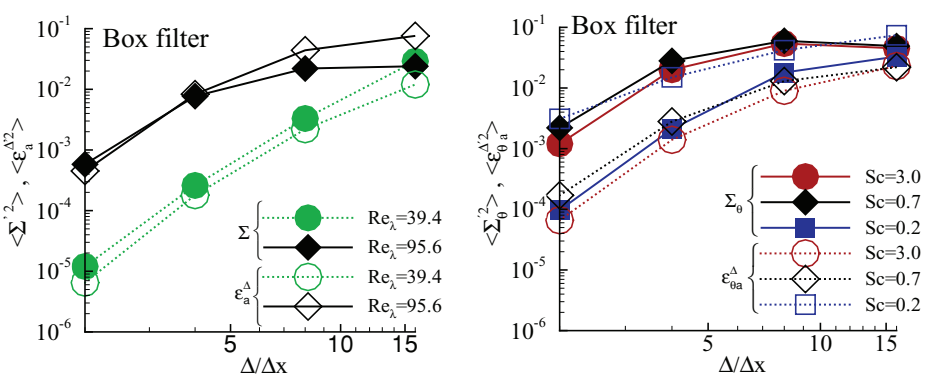

Figure 13. Variance of the exact and modelled molecular SGS dissipation terms for all the simulations and filter sizes used in the present work: (a) variance of Σ and ε_a^Δ, (b) variance of Σ_θ and $\varepsilon_{\theta a}^\Delta$. The classical models for the molecular SGS dissipations ε_a^Δ and $\varepsilon_{\theta a}^\Delta$ are given by Equations (6) and (7), respectively.

comparison between Σ_θ and $\varepsilon^\Delta_{\theta a}$ (Figure 13(b)) shows that the agreement is also reasonable, although not as good. In particular, note that no model constant could be chosen in order to obtain a perfect agreement between Σ_θ and $\varepsilon^\Delta_{\theta a}$ for all filter sizes. Moreover, the influence of the Schmidt number is not well reproduced by the model as can be attested by comparing Σ_θ and $\varepsilon^\Delta_{\theta a}$ for a given filter size for the simulation with $Re_\lambda = 95.6$, $Sc = 0.7$ and the simulation with $Re_\lambda = 95.6$, $Sc = 0.2$: although the exact molecular SGS dissipation Σ_θ decreases with the Schmidt number, its modelled values $\varepsilon^\Delta_{\theta a}$ increase with Sc.

Figures 14(a) and (b) show the values of the skewness for the (exact and modelled) viscous and molecular SGS dissipation terms, respectively. Note that the skewnesses are always positive and, for $Re_\lambda = 95.6$ and $\Delta/\Delta x = 16$ we have $S(\Sigma) \approx 6 - 7$ which is close to the values obtained by da Silva and Métais [12] in turbulent plane jets. For the viscous SGS dissipation term (Figure 14(a)) we see that the agreement between the exact Σ and modelled ε^Δ_a quantities is quite good. In particular for the largest filter size the exact and modelled skewnesses are almost the same. Furthermore, the classical model captures again the correct trend in terms of Reynolds number and filter size, i.e. the skewness of both Σ and ε^Δ_a decreases as the Reynolds number and filter size increases. For the molecular SGS dissipation term (Figure 14(b)) again the results are not as good: once more the influence of the Schmidt number is not well captured, even if the skewness of both Σ_θ and $\varepsilon^\Delta_{\theta a}$ seem to be relatively insensitive to changes in the Schmidt number.

The flatness factors for the (exact and modelled) viscous and molecular SGS dissipations terms (not shown) decrease with increasing filter size for all simulations, which indicates a decrease in the intermitency of the dissipation for large filter sizes (as expected) and are again close to the values from da Silva and Métais [12]. However, the results showed again that the classical model ε^Δ_a exhibits the correct trend with the Reynolds number, while $\varepsilon^\Delta_{\theta a}$ does not show the correct trend with the Schmidt number.

To summarise, in contrast with the analysis of the correlation coefficients and joint probability density functions, where the results of the classical model for both ε^Δ_a and $\varepsilon^\Delta_{\theta a}$ are equally very good, the study of several one-point statistics shows that the classical model works better for the viscous SGS dissipation ε^Δ_a than for the molecular SGS dissipation $\varepsilon^\Delta_{\theta a}$.

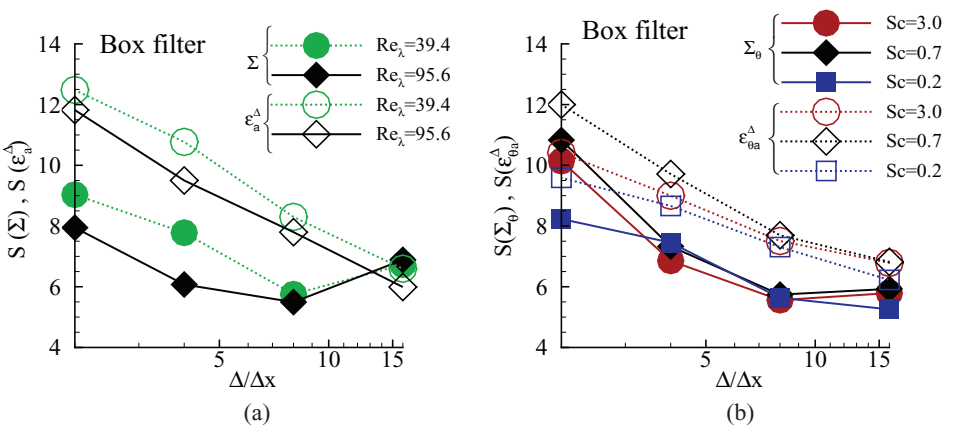

Figure 14. Skewness of the exact and modelled molecular SGS dissipation terms for all the simulations and filter sizes used in the present work: (a) skewness of ε^Δ and ε^Δ_a, (b) skewness of $\varepsilon^\Delta_\theta$ and $\varepsilon^\Delta_{\theta a}$. The classical models for the molecular SGS dissipations ε^Δ_a and $\varepsilon^\Delta_{\theta a}$ are given by Equations (6) and (7), respectively.

5.1.4. *Comparison in the Fourier space: spectra of the molecular SGS dissipation terms*

It is interesting to analyse the spatial 3D spectrum of the molecular SGS dissipation terms from Equations (1) and (2), and to compare these with the classical models defined in Equations (6) and (7). For example, for the modelled viscous SGS dissipation term Σ, we define its spatial 3D spectrum $E_\Sigma(K)$ by

$$\langle \widehat{\Sigma}(\vec{K}')\widehat{\Sigma}(\vec{K})\rangle = \frac{E_\Sigma(K)}{2\pi K^2}\delta(\vec{K}+\vec{K}'), \tag{26}$$

where $\widehat{\Sigma}(\vec{K})$ is the Fourier transform of $\Sigma(\vec{x})$,

$$\widehat{\Sigma}(k_1,k_2,k_3) = \frac{1}{(2\pi)^3}\int_{-\infty}^{+\infty}\int_{-\infty}^{+\infty}\int_{-\infty}^{+\infty}\Sigma(x,y,z)\mathrm{e}^{-\mathrm{i}(xk_1+yk_2+zk_3)}\mathrm{d}k_1\mathrm{d}k_2\mathrm{d}k_3, \tag{27}$$

and $\vec{K}=(k_1,k_2,k_3)$ is the wave number vector, of norm $K=|\vec{K}|=\sqrt{k_1^2+k_2^2+k_3^2}$. The spectra $E_\Sigma(K)$ relates to the variance of the viscous SGS dissipation term through

$$\frac{1}{2}\langle \Sigma'^2\rangle = \int_0^\infty E_\Sigma(K)\mathrm{d}K. \tag{28}$$

Similar definitions apply to the other viscous/molecular SGS dissipation terms. We denote by $E_\Sigma(K)$ and $E_{\Sigma\theta}(K)$ the spectra of the exact viscous/molecular SGS dissipation terms, and by $E_a(K)$ and $E_{\theta a}(K)$ the spectra of the modelled viscous/molecular SGS dissipation terms using the models defined in Equations (6) and (7), respectively.

Figures 15(a) and (b) show $E_\Sigma(K)$, $E_{\Sigma\theta}(K)$, $E_a(K)$ and $E_{\theta a}(K)$ for filter sizes $\Delta/\Delta x=4$ and $\Delta/\Delta x=16$, where each spectrum results from averaging over several (10) spectra/instantaneous fields. Note that since the *a priori* tests are done in the LES grid there are more wave numbers to describe spectra for the smaller filter size.

Comparing the exact and modelled viscous/molecular SGS dissipations in the Fourier space we see that the agreement between the spectra is generally very good. This is particularly true for the smaller filter size $\Delta/\Delta x=4$, where, apart from a constant we do have $E_\Sigma(K)\approx E_a(K)$, and $E_{\Sigma\theta}(K)\approx E_{\theta a}(K)$ for almost all wave number range. Moreover, the good agreement between the exact and the modelled spectra exists mainly for small and intermediate wave numbers i.e. the differences arise particularly for high wave numbers, where there is more 'energy' in the exact than in the modelled viscous/molecular SGS dissipations. Another result that becomes apparent from these plots is that the agreement between the exact and modelled spectra is better for the velocity than for the scalar field, as can be seen by comparing the spectra for $\Delta/\Delta x=16$: $E_\Sigma(K)\approx E_a(K)$ until $K\approx 3$, while for the scalar field we have $E_{\Sigma\theta}(K)\approx E_{\theta a}(K)$ until $K\approx 1$. Qualitatively similar results were obtained with the other filter sizes (not shown).

In summary, the analysis of the spectra from the exact and modelled molecular SGS dissipation concurs with the previous results: the classical models do give good results, in terms of spatial localisation, statistical behaviour, model constant behaviour and spectral characteristics. Moreover, the results tend to be better for large filter sizes, which are encouraging for practical applications of LES. Finally, remark that the classical model for the viscous SGS dissipation term ε_a^Δ is always better than the molecular SGS dissipation $\varepsilon_{\theta a}^\Delta$. Probably, this has to do with the factor K_{sgs} in the definition of $\varepsilon_{\theta a}^\Delta$, as discussed during the analysis of the topology of this quantity.

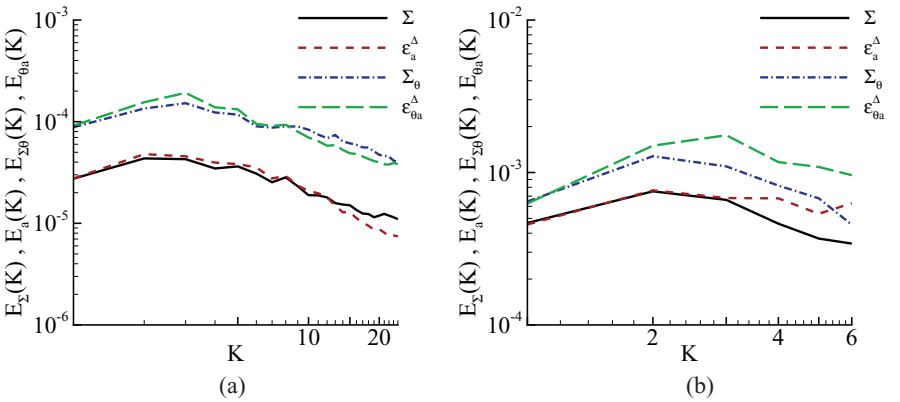

Figure 15. Spectrum of the exact (Σ and Σ_θ) and modelled (ε_a^Δ and $\varepsilon_{\theta a}^\Delta$) molecular SGS dissipation terms for filter widths $\Delta/\Delta x = 4$ (a) and, $\Delta/\Delta x = 16$ (b), for the simulation with $Re_\lambda = 95.6$ and $Sc = 0.7$. Each spectrum results from averaging over several (10) spectra/instantaneous fields, and in order to facilitate the comparison between the exact and modelled spectra the model constants were modified to have $E_\Sigma(K = 0) = E_a(K = 0)$ and $E_{\Sigma\theta}(K = 0) = E_{\theta a}(K = 0)$.

5.2. *Analysis of the hybrid RANS/LES models ε_b^Δ and $\varepsilon_{\theta b}^\Delta$*

In hybrid continuous RANS/LES turbulence modelling it is sometimes advantageous to model the viscous/molecular dissipations of SGS kinetic energy and SGS scalar variance using Equations (12) and (13), respectively (e.g. [3, 4]). This is due to the need to switch between the RANS and the LES modes in hybrid RANS/LES models. However, as anticipated by an inspection of these equations it is unlikely that these models will lead to good results. Indeed, one of the premisses of high-Reynolds number turbulence is the existence of a 'separation' of scales between the large scales of motion associated with most energy, and the small scales of motion associated with the process of viscous dissipation. In agreement with this, and as shown in many works, the grid-scale (GS) and SGS kinetic energy are very poorly correlated. For instance, da Silva and Métais observed that $\mathrm{Corr}(\overline{u_i}\ \overline{u_i}, \tau_{ii}) \approx 0.22$. The problem with Equation (12) is that the (exact) viscous dissipation of SGS kinetic energy Σ takes place at small scales, whereas the modelled SGS dissipation ε_b^Δ is proportional to the GS kinetic energy $\bar{K}$ which is clearly associated with the large scales of motion. Therefore, we expect the model defined by Equation (12) to lead to poor results, both in terms of its topology and its statistics. A similar problem is expected to exist with the molecular SGS dissipation term $\varepsilon_{\theta b}^\Delta$ defined by Equation (13).

We computed the correlation between the two terms of each side of Equations (12) and (13) and confirmed that the local correlation is indeed very small for all the Reynolds and Schmidt numbers and all the filter sizes considered in this work. All the correlation coefficients are displayed in Figure 16: we obtained $\mathrm{Corr}(\Sigma, \varepsilon_b^\Delta) \leq 0.16$ and $\mathrm{Corr}(\Sigma_\theta, \varepsilon_{\theta b}^\Delta) \leq 0.09$. Moreover, the correlations between Σ and ε_b^Δ tend to decrease as the Reynolds number and the filter size increases, while for $\mathrm{Corr}(\Sigma_\theta, \varepsilon_{\theta b}^\Delta)$ it is difficult to identify a clear trend on Re_λ, Sc and Δ. Finally, note that the correlations for the dissipation of SGS scalar variance tend to be smaller than those for the SGS kinetic energy equation.

The joint PDF between Σ and ε_b^Δ, and between Σ_θ and $\varepsilon_{\theta b}^\Delta$ are shown in Figures 17(a) and (b), respectively. The absence of correlation between the exact and modelled quantities can be observed for all the range of their values. Note that no discernible difference can be seen between the joint PDFs for $\Delta/\Delta x = 4$ and 16. The same occurs for the other filter sizes (not shown).

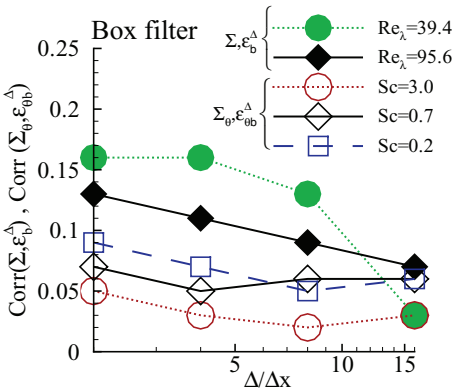

Figure 16. Correlation coefficients between the exact molecular SGS dissipations (Σ and Σ_θ) and their hybrid models (ε_b^Δ and $\varepsilon_{\theta b}^\Delta$) defined by Equations (12) and (13). The correlations were obtained with filter widths $\Delta/\Delta x = 2$, 4, 8, and 16, and were computed using the data in the LES mesh *i.e.* both filtering and sampling were used in the *a-priori* tests.

Finally, the computation of the model constants $C_{\varepsilon b}^\Delta$ and $C_{\varepsilon\theta b}^\Delta$ defined in Equations (12) and (13) was carried out as before, i.e. using equations similar to (24) and (25). Results are shown in Figure 18 and show that the values assumed by the constants change by about three orders of magnitude as the filter size varies between $2 \leq \Delta/\Delta x \leq 16$: $0.0002 \leq C_{\varepsilon b}^\Delta \leq 0.227$ and $0.000\,6 \leq C_{\varepsilon\theta b}^\Delta \leq 0.271$. Moreover, the values of the constants tend to increase dramatically with the filter size, without any tendency to reach an asymptotic value. Therefore, the use of a new procedure for the computation of the model constants $C_{\varepsilon b}^\Delta$ and $C_{\varepsilon\theta b}^\Delta$ defined in Equations (12) and (13), respectively, seems to be absolutely essential for the hybrid models i.e. no constant value for $C_{\varepsilon b}^\Delta$ and $C_{\varepsilon\theta b}^\Delta$ should in principle be used in any application. Note that, as remarked by a referee, the use of the 'dynamic procedure' to compute the model constants $C_{\varepsilon b}^\Delta$ and $C_{\varepsilon\theta b}^\Delta$ is not expected to solve the problem, since this procedure assumes that the constant at two different filter widths is the same and this assumption is clearly inconsistent with the results displayed in Figure 18.

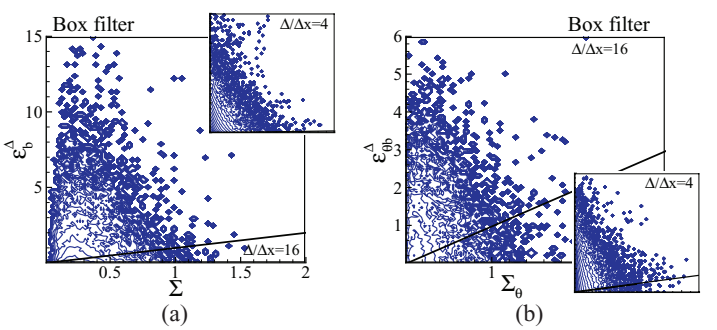

Figure 17. Joint PDFs between (a) the exact (Σ) and modelled (ε_b^Δ) viscous SGS dissipation and, (b) between the exact (Σ_θ) and modelled ($\varepsilon_{\theta b}^\Delta$) molecular SGS dissipation, for the simulations with $Re_\lambda = 95.6$, and $Sc = 0.7$, and for filter widths $\Delta/\Delta x = 4$ and $\Delta/\Delta x = 16$. The hybrid models for the molecular SGS dissipations ε_b^Δ and $\varepsilon_{\theta b}^\Delta$ are given by Equations (12) and (13), respectively.

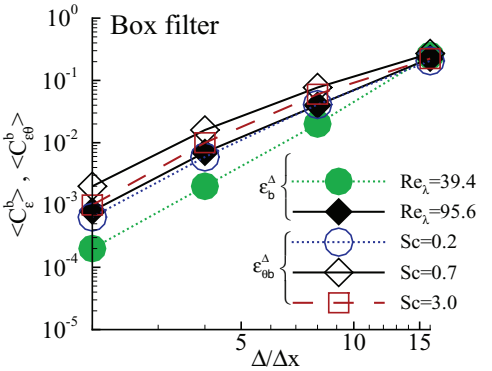

Figure 18. Constants C_ε^b and $C_{\varepsilon\theta}^b$ defined in Equations (12) and (13), respectively, for all the simulations and filter sizes used in the present work. The constants were computed using equations similar to Equations (24) and (25).

We suggest here a simple way to compute the model constant $C_{\varepsilon b}^\Delta$ using the dissipation law $\varepsilon = C_\varepsilon u'^3/L_{11}$, where L_{11} is the integral scale, and C_ε is the normalised energy dissipation rate [63]. Unfortunately, the constant C_ε is not universal [64] and presents a wide scatter $0.5 < C_\varepsilon < 2.5$ for $Re_\lambda > 50$ [65]. However, for isotropic turbulence at sufficiently high-Reynolds number ($Re_\lambda > 100$–200) C_ε tends to $C_\varepsilon \approx 0.5$.

For high-Reynolds numbers and inertial range filter sizes it is reasonable to assume that the total and the GS kinetic energies are similar i.e. $K \approx \bar{K}$, therefore, since $\langle\varepsilon\rangle = \langle\varepsilon_b^\Delta\rangle$, we can write

$$C_\varepsilon \frac{\left(2\bar{K}/3\right)^{3/2}}{L_{11}} = C_{\varepsilon b}^\Delta \frac{\bar{K}^{3/2}}{\Delta}, \tag{29}$$

which leads to

$$C_{\varepsilon b}^\Delta = C_\varepsilon \left(\frac{2}{3}\right)^{3/2} \left(\frac{\Delta}{L_{11}}\right). \tag{30}$$

Thus, according to this relation the constant C_ε increases (linearly) with the filter size Δ. This agrees reasonably well with the values of C_ε obtained for the larger filter sizes ($\Delta = 4, 8, 16$) in Figure 18. In particular using Equation (30) for $\Delta = 8$ and 16 we obtain $C_{\varepsilon b}^\Delta = 0.057$ and 0.115, respectively, which are not far from the values of $C_{\varepsilon b}^\Delta = 0.04$ and 0.227, respectively, that we obtain from the present data (plotted in Figure 18), particularly taking into consideration the relatively small inertial range from the present simulation, as well as the variability of C_ε with the Reynolds number discussed above.

The analysis of other one-point statistics such as the variance, skewness and flatness also showed the existence of big differences in terms of statistical characteristics of the exact (Σ and Σ_θ) and modelled (ε_b^Δ and $\varepsilon_{\theta b}^\Delta$) viscous/molecular SGS dissipation terms (not shown). In particular, the modelled quantities do not display the correct trend with the filter size e.g. the variances of Σ and Σ_θ decrease as the filter size increases, while the modelled variance ε_b^Δ and $\varepsilon_{\theta b}^\Delta$ increase with the filter size. Moreover, the influence of the Reynolds and Schmidt numbers is not well recovered.

In order to visualise the reason behind these discrepancies between the exact and modelled quantities, Figure 19 shows spectra of the viscous/molecular SGS dissipation terms for all the simulations used in the present work. Unlike in the classical model discussed before, the spectral shape of the hybrid models for the viscous/molecular SGS dissipation terms defined by Equations (12) and (13) is very different from the spectral shape of the real or exact terms. As expected, the 'energy' associated with the fluctuations of the modelled viscous SGS dissipation term ε_b^Δ falls fast as the wave number increases, since it is associated with the resolved kinetic energy and scalar variance, which are clearly large-scale dominated quantities, whereas the exact viscous SGS dissipation term Σ falls at a much slower rate – compare the shapes of $E_\Sigma(K)$ and $E_b(K)$ for $\Delta/\Delta x = 4$ shown in Figure 19(a). For this reason, it is impossible to find a constant C_ε^b such that $E_\Sigma(K) = E_a(K)$ for all $0 \leq K \leq K_{\max}$.

Concerning the exact and modelled molecular SGS dissipation Σ_θ and $\varepsilon_{\theta b}^\Delta$, respectively, a similar limitation exists. Particularly, for $\Delta/\Delta x = 4$ we see that the spectrum of the modelled molecular SGS dissipation $E_{\theta b}(K)$ also falls much faster than the spectrum of the exact molecular SGS dissipation Σ_θ – see Figure 19(a). Furthermore, remark that as with the classical model, the model for the viscous SGS dissipation ε_b^Δ performs better than the model for the molecular SGS dissipation $\varepsilon_{\theta b}^\Delta$.

In summary, the model equations based on Equations (12) and (13) give poor results and are unlikely to lead to accurate models for Σ and Σ_θ. The present results agree with the results from Grimaji et al. [28].

5.3. *Analysis of the model from Jiménez* $\boldsymbol{\varepsilon_{\theta c}^\Delta}$

In this section, we analyse the model from Jiménez et al. [5] for the molecular SGS dissipation term $\varepsilon_{\theta c}^\Delta$ defined by Equation (20). As described in Section 2 the model uses the SGS mechanical-to-thermal time scale ratio r_{sgs} which is supposed to be only a function of the Schmidt number. We start by assessing this hypothesis before embracing the analysis of the correlation functions, joint probability functions and one-point statistics and spectra.

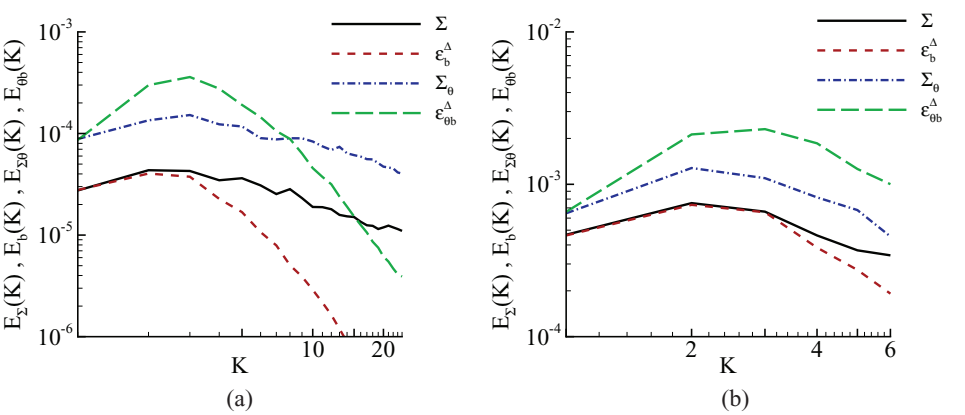

Figure 19. Spectrum of the exact (Σ and Σ_θ) and modelled (ε_b^Δ and $\varepsilon_{\theta b}^\Delta$) SGS kinetic energy/scalar variance molecular dissipation terms for filter widths $\Delta/\Delta x = 4$ (a) and $\Delta/\Delta x = 16$ (b), for the simulation with $Re_\lambda = 95.6$ and $Sc = 0.7$. Each spectrum shown results from averaging over several (10) spectra/instantaneous fields, and in order to facilitate the comparison between the exact and modelled spectra the model constants were modified to have $E_\Sigma(K=0) = E_b(K=0)$ and $E_{\Sigma\theta}(K=0) = E_{\theta b}(K=0)$.

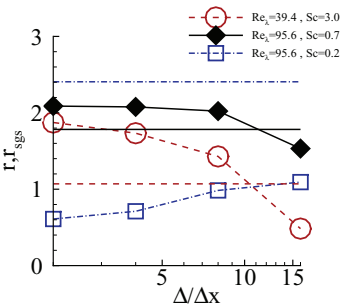

Figure 20. Mechanical-to-thermal time scale ratio defined by Equation (18) (lines without symbols), and SGS mechanical-to-thermal time scale ratio defined by Equation (17) (lines with symbols) for all the Reynolds and Schmidt numbers and all the filter sizes used in the present work.

5.3.1. *SGS mechanical-to-thermal time scale ratio*

Jiménez et al. [5] define a SGS mechanical-to-thermal time scale ratio r_{sgs} (see Equation (17)) that is invoked in the derivation of the model for ε_c^{Δ}. Specifically, the model by Jiménez et al. [5] implicitly assumes that

$$r_{\text{sgs}} \sim \frac{1}{Sc}. \tag{31}$$

In order to test this hypothesis r_{sgs} was computed from the present data from its definition given by Equation (17). The results are shown in Figure 20. The values for the (total) mechanical-to-thermal time scale ratio r defined in Equation (18) are also shown.

Starting with r the present results show that r tends to increase with the Reynolds number in agreement with Overholt and Pope [32]. Moreover, by comparing the values of r for $Sc = 0.2$ ($r = 2.41$) and $Sc = 0.7$ ($r = 1.78$) at the same Reynolds number ($Re_\lambda = 95.6$) we see that r decreases as the Schmidt number increases. The value of $r \approx 1.78$ obtained for $Re_\lambda = 95.6$ and $Sc = 0.7$ is in good agreement with the values obtained by Overholt and Pope [32] at similar Reynolds and Schmidt numbers. Thus we observe that r is not a universal variable, since it depends on both the Reynolds and Schmidt numbers in agreement with the results from Overholt and Pope [32].

Concerning the SGS mechanical-to-thermal time scale ratio r_{sgs} the results displayed in Figure 20 show that in addition to its expected dependence on the Reynolds and Schmidt numbers, r_{sgs} also varies with the filter size. The influence of the filter size is difficult to assess with the present data. For $Re_\lambda = 95.6$ and $Sc = 0.7$, as for $Re_\lambda = 39.4$ and $Sc = 3.0$, r_{sgs} decreases as the filter size increases, while for $Re_\lambda = 95.6$ and $Sc = 0.2$ the opposite occurs.

We used the present data also to assess whether $r_{\text{sgs}} \sim \frac{1}{Sc}$, as supposed by Jiménez et al. [5]. As can be seen this is a poor approximation for some cases, while it seems to work reasonably well for others. For instance, for the simulation with $Re_\lambda = 95.6$ and $Sc = 0.2$, we have $r_{\text{sgs}} = 1.09$ (for $\Delta/\Delta x = 16$) while $1/Sc = 5.0$ i.e. the assumption fails for this case. On the other hand, for $Re_\lambda = 95.6$ and $Sc = 0.7$, we have $r_{\text{sgs}} = 1.09$ (for $\Delta/\Delta x = 16$) and $1/Sc = 1.43$ which is reasonably close. Similarly, for $Re_\lambda = 39.4$ and $Sc = 3.0$, we have $r_{\text{sgs}} = 0.48$ (for $\Delta/\Delta x = 16$) which is again quite near $1/Sc = 0.33$. Therefore, we conclude that r_{sgs}, like r is not a universal parameter i.e. in addition to depending on the Reynolds and Schmidt numbers, the value of r_{sgs}

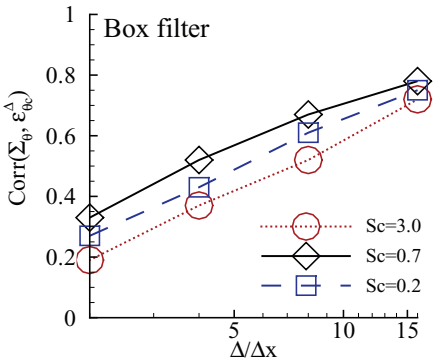

Figure 21. Correlation coefficients between the exact molecular SGS dissipation term (Σ_θ) and the model by Jiménez et al. [5] ($\varepsilon^\Delta_{\theta c}$) defined by Equation (20). The correlations were obtained with filter widths $\Delta/\Delta x = 2, 4, 8$, and 16, and were computed using the data in the LES mesh i.e. both filtering and sampling were used in the *a-priori* tests.

varies with the filter size. However, the approximation $r_{\text{sgs}} \sim \frac{1}{Sc}$ used by Jiménez et al. [5] works well at least for $Sc \geq 0.7$.

5.3.2. *Correlation coefficients and joint probability density functions*

The correlation coefficients between the exact (Σ_θ) and modelled ($\varepsilon_{\theta c}$) molecular SGS dissipation using the model by Jiménez et al. [5] are shown in Figure 21 as functions of the Reynolds and Schmidt numbers, and of the filter size for all the simulations used in the present work. As can be seen all the correlations increase fast as the filter size increases, which is a first good indication. Moreover, the correlations are higher for the most important case, i.e. $Re_\lambda = 95.6$, $Sc = 0.7$ and $\Delta/\Delta x = 16$ (inertial range).

The joint probability density functions between the exact (Σ_θ) and the modelled ($\varepsilon_{\theta c}$) molecular SGS dissipation displayed in Figure 22 complement information from the analysis of Corr(Σ_θ, $\varepsilon^\Delta_{\theta c}$). For small filter sizes ($\Delta/\Delta x = 4$) there is no correlation between the exact and modelled molecular SGS dissipation, while for large (inertial range) filter sizes $\Delta/\Delta x = 16$ the

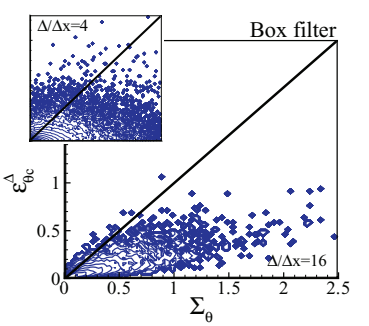

Figure 22. Joint PDFs between the exact (Σ_θ) and modelled ($\varepsilon^\Delta_{\theta c}$) molecular SGS dissipation, for the simulations with $Re_\lambda = 95.6$, and $Sc = 0.7$, and for filter widths $\Delta/\Delta x = 4$ and $\Delta/\Delta x = 16$.

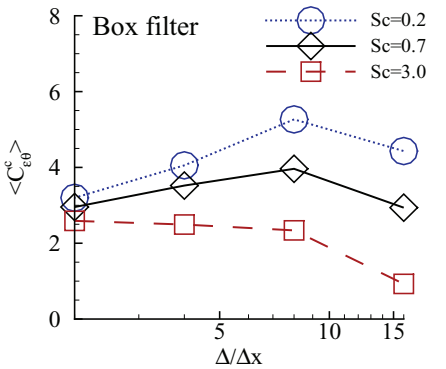

Figure 23. Constant $C^c_{\varepsilon\theta}$ defined in Equation (20) for all the simulations and filter sizes used in the present work. The constants were computed with an equation similar to Equation (25).

correlation is high. The joint probability density functions also show that this high correlation between Σ_θ and $\varepsilon_{\theta c}$ comes from all the range of their values.

To conclude, these first results show that in terms of spatial localisation the model from Jiménez et al. [5] defined in Equation (20) consists in a good representation of the exact molecular SGS dissipation, at least for large filter sizes.

5.3.3. *Constant* $C^c_{\varepsilon\theta}$

The model constant $C^c_{\varepsilon\theta}$ defined by Equation (20) was computed from the present data using equations similar to Equations (25) used to compute the constants for classical model $\varepsilon^\Delta_{\theta a}$. The results are displayed in Figure 23 and show that the constant assumes values between $0.93 \leq C^c_{\varepsilon\theta} \leq 5.27$ and shows a tendency to increase with the Schmidt number. The range is slightly larger but comparable to that found for the classical model $\varepsilon^\Delta_{\theta a}$. In contrast with the other models there is no clear trend with the filter size for this model. Note that the model constant for this model is related to the SGS mechanical-to-thermal scale ratio r_{sgs} through $C^c_{\varepsilon\theta} = 2r_{\text{sgs}}$. As discussed previously, the model from Jiménez et al. [5] assumes that $r \sim 1/Sc$,

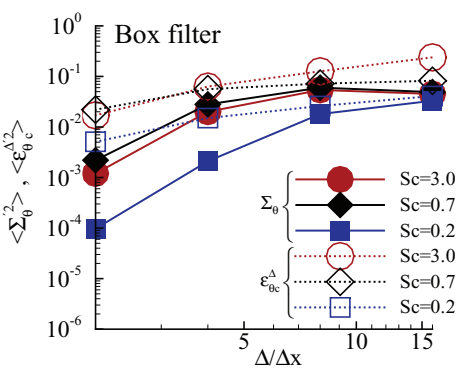

Figure 24. Variance of the exact (Σ_θ) and modelled ($\varepsilon^\Delta_{\theta c}$) molecular SGS dissipation term for all the simulations and filter sizes used in the present work, with the model defined by Equation (20).

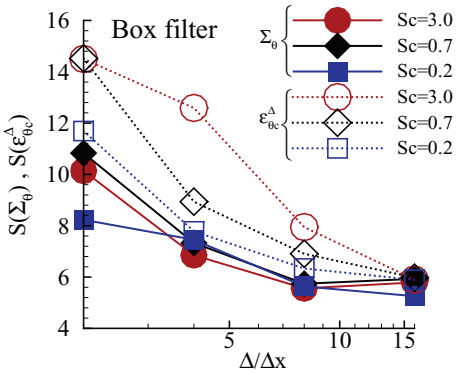

Figure 25. Skewness of the exact (Σ_θ) and modelled ($\varepsilon^{\Delta}_{\theta c}$) molecular SGS dissipation term for all the simulations and filter sizes used in the present work, with the model defined by Equation (20).

which is reasonably well observed for Schmidt numbers $Sc = 0.7$, but not for $Sc = 0.2$. In agreement with this the constant $C^c_{\varepsilon\theta} = 2.938$ for $Re_\lambda = 95.6$ and $Sc = 0.7$ ($\Delta/\Delta x = 16$), which is close to $2r_{\text{sgs}} \sim 2/Sc \sim 2.856$. However, for $Re_\lambda = 95.6$ and $Sc = 0.2$ ($\Delta/\Delta x = 16$) we have $C^c_{\varepsilon\theta} = 4.431$ which is quite far from $2r_{\text{sgs}} \sim 2/Sc \sim 10$, as assumed by the model. Therefore, we conclude that the determination of the constant $C^c_{\varepsilon\theta}$ in the model from Jiménez et al. [5] should be improved for other Schmidt numbers, i.e. other than $Sc \approx 1.0$.

5.3.4. *One-point statistics: variance, skewness and flatness*

In order to assess the statistical behaviour of the model $\varepsilon^{\Delta}_{\theta c}$ we computed the variance, skewness and flatness of the exact and modelled quantities for all the filter sizes and all the simulations

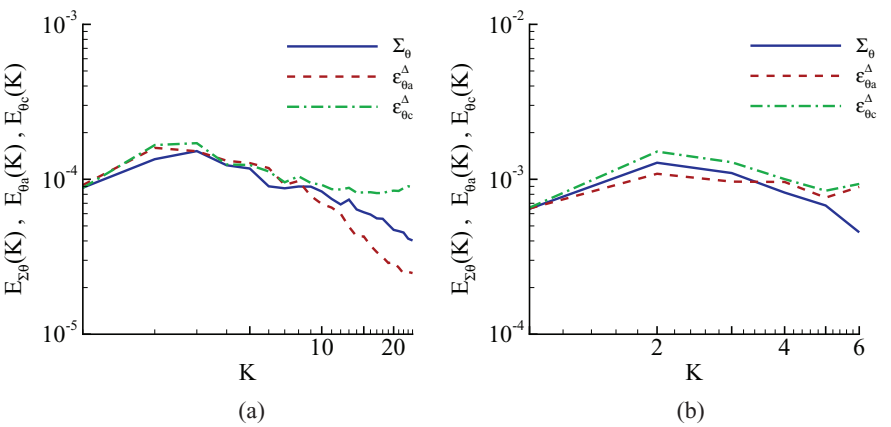

Figure 26. Spectrum of the exact ($\varepsilon^{\Delta}_{\theta}$) and modelled ($\varepsilon^{\Delta}_{\theta c}$) SGS scalar variance molecular dissipations for filter widths (a) $\Delta/\Delta x = 4$ and (b) $\Delta/\Delta x = 16$, for the simulation with $Re_\lambda = 95.6$ and $Sc = 0.7$. Each spectrum shown results from averaging over several (10) spectra/instantaneous fields, and in order to facilitate the comparison between the exact and modelled spectra the model constants were modified to have $E_\Sigma(K = 0) = E_c(K = 0)$ and $E_{\Sigma\theta}(K = 0) = E_{\theta c}(K = 0)$. Moreover, the spectra for the classical models—$E_a(K)$, $E_{\theta a}(K)$—is also shown.

used in this work. The results for the variance and skewness are shown in Figures 24 and 25, respectively. As in the classical model, the variance of Σ_θ is well captured by the model $\varepsilon_{\theta c}^{\Delta}$ i.e. the modelled variance increases with the filter size. In the present case, however, the agreement between the exact and modelled variances is better than in the classical model (compare Figures 13(b) and 24).

Concerning the skewness factor (see Figure 25) we see that the model from Jiménez et al. [5] also provides the correct result of decreasing skewness with increasing filter size, and is generally in good agreement with the exact skewness. Note that for the higher filter sizes (i.e. $\Delta/\Delta x = 8$ and $\Delta/\Delta x = 16$) the results are also better than as with the classical model (compare Figures 14(b) and 25). The same can be said about the evolution of the flatness factor (not shown).

To summarise, comparing results from several one-point statistics of the exact and modelled molecular SGS dissipations we see that the model from Jiménez et al. [5] defined by Equation (20) gives good results in *a priori* tests, and works even better than the classical model defined by Equation (7). The behaviour of the model in the wave number space is analysed next.

5.3.5. *Comparison in the Fourier space: spectra of the molecular SGS dissipation terms*

To assess the model for the molecular SGS dissipation from Jiménez et al. [5] $\varepsilon_{\theta c}^{\Delta}$ in the wave number space Figures 26(a) and (b) show spatial three-dimensional spectra of the exact and modelled molecular SGS dissipation for the simulation with $Re_\lambda = 95.6$ and $Sc = 0.7$, and for filter sizes $\Delta/\Delta x = 4$ and $\Delta/\Delta x = 16$, respectively. As before we denote the spectra of the exact molecular SGS dissipation by $E_{\Sigma\theta}(K)$ while $E_{\theta c}(K)$ represents the spectra of the modelled molecular SGS dissipation. The spectra $E_{\theta a}(K)$ from the classical model is also shown.

By comparing the spectra of the exact and modelled molecular SGS dissipation terms we see that the agreement obtained with the model from Jiménez et al. [5] is very good for almost all wave number range i.e. $E_{\Sigma\theta}(K) \approx E_{\theta c}(K)$ for all K, except near the end of the wave number range, where $E_{\Sigma\theta}(K) < E_{\theta c}(K)$. Moreover, note that the results from the model from Jiménez et al. [5] are very similar to the results from the classical model i.e. $E_{\theta c}(K) \approx E_{\theta a}(K)$, again almost everywhere, except near the end of the wave number range.

To summarise, the analysis of the model from Jiménez et al. [5] for the molecular SGS dissipation $\varepsilon_{\theta c}^{\Delta}$ in the Fourier space shows that this model, like the classical model, reproduces very well the exact molecular SGS dissipation Σ_θ. Moreover, the analysis of one-point statistics shows that this model performs even better than the classical model $\varepsilon_{\theta a}^{\Delta}$. The only limitation of the model is the determination of the model constant $C_{\varepsilon\theta}^{c}$ for which a more accurate procedure should be pursued.

6. Conclusions

In the present work DNS of statistically stationary (forced) homogeneous, isotropic turbulence with Reynolds and Schmidt numbers ranging from $39.4 \leq Re_\lambda \leq 95.6$ and $0.2 \leq Sc \leq 3.0$, respectively, were used to investigate the viscous and the molecular SGS dissipation terms (Σ and Σ_θ) from the SGS kinetic energy and SGS scalar variance transport equations, representing the final (dissipative) stages of the energy cascade mechanism.

It was observed that Σ and Σ_θ are not correlated. The viscous SGS dissipation Σ has a mixed tube/fragmented sheet structure where regions of intense Σ displaying a sheet-like structure tend to be associated with medium and intense values of viscous dissipation of (total) kinetic energy ε, while the regions of Σ displaying a tube-like structure are also characterised by intense values of vorticity norm. The molecular SGS dissipation Σ_θ on the other hand, displays a thin sheet structure, which is correlated with the molecular dissipation of total scalar variance ε_θ.

Moreover, it was observed that the regions of intense SGS kinetic energy τ_{ii} also display a mixed tube/sheet structure which is also correlated both with regions of intense vorticity norm and with regions of intense viscous dissipation of kinetic energy ε. Furthermore, important values of SGS scalar variance q_θ also exist in zones of strong molecular dissipation of total scalar variance ε_θ. Consistently, and with implications for the classical models used for Σ and Σ_θ, it was observed that Σ is strongly correlated with the regions of SGS kinetic energy τ_{ii}, while Σ_θ is associated with the regions of intense SGS scalar variance q_θ, and moreover, these correlations tend to increase as the filter size increases.

Using classical *a priori* tests three models for the molecular dissipation of SGS kinetic energy and SGS scalar variance were analysed: (a) the classical model by Yoshizawa [2], (b) the model used in hybrid RANS/LES by e.g. Paterson and Peltier [3] and (c) the model for the molecular SGS dissipation of SGS scalar variance from Jiménez et al. [5].

In terms of spatial localisation both the classical models as the model from Jiménez et al. [5] give good results, while the model used in hybrid RANS/LES fails to represent the topology of the exact viscous/molecular SGS dissipation terms.

Concerning the model constants the results showed that for the classical models the constants tend asymptotically to the theoretical values. In particular, for high-Reynolds numbers, Schmidt number not far from 1.0 and large filter sizes, the constants for the classical model are very close to the theoretical values, which are therefore a good approximation for use in engineering or geophysical applications. For the model by Jiménez et al. [5] however, the model constant varies with the Schmidt number in a way which is inconsistent with the approximation $r_{\text{sgs}} \sim 1/Sc$ proposed by Jiménez et al. [5]. The model constant is well approximated for $Sc = 0.7$ and $Sc = 3.0$, but not so much for smaller Schmidt numbers e.g. $Sc = 0.2$. This is a consequence of the lack of universality of the SGS mechanical-to-thermal time scale ratio r_{sgs}, which is used by several other models. Indeed, in addition to depending—like r the mechanical-to-thermal time scale ratio—on the Reynolds and Schmidt numbers, r_{sgs} also depends on the size of the implicit grid filter. Therefore, a new procedure for the computation of the model constant (at least for Schmidt numbers lower than $Sc \approx 1$) should be pursued. Finally, the model constants used in the hybrid RANS/LES model increase dramatically with the filter size, therefore making it impossible to use them as 'constants' during a LES. Moreover, it is unlikely that the 'dynamic procedure' will be able to solve this limitation, and therefore a new methodology for the computation of the model constants must be developed. A simple way to compute this model constant is suggested here through Equation (30).

Comparison of several one-point statistics from the exact and modelled viscous/molecular SGS dissipation terms showed that both classical and the model from Jiménez et al. [5] give generally good results. For the classical model the results seem to be better for the modelling of Σ than for the modelling of Σ_θ, where the model proposed by Jiménez et al. [5] performs even better. On the other hand, the results from the hybrid RANS/LES model showed once again very poor results.

The analysis of the exact and modelled viscous/molecular SGS dissipation terms in the Fourier space allowed to explain the main reason behind the poor results displayed by the hybrid RANS/LES model. It turns out that the modelled SGS dissipation given by the hybrid RANS/LES model is concentrated in much lower wave numbers than the exact molecular SGS dissipation, which represents the real trend to be reached.

The present results seem to imply that in order to be successful any model for the viscous or molecular SGS dissipation term must be defined in terms of quantities dominated by scales of motion near the implicit LES filter. The hybrid RANS/LES model from Paterson and Peltier [3] is clearly inconsistent with this requirement, since in this model the viscous and molecular SGS dissipation terms are defined in terms of the grid-scales kinetic energy $\bar{K}$ and GS scalar

variance $\overline{\Theta}$, which are clearly associated with the large scales of motion while the exact SGS dissipations Σ and Σ_θ take place mainly near the smallest scales of motion.Thus, the present work demonstrated that the classical model used by Schumann [1] is far superior to the hybrid RANS/LES model from Paterson and Peltier [3]; however, it must be stressed that in some sense this comparison is a bit unfair to the hybrid RANS/LES model since it uses resolved quantities in order to model unresolved quantities, whereas the classical model uses unresolved quantities. In practice the classical model will only be as good as the model used for K_{sgs}.

Acknowledgement

Carlos B. da Silva is supported by the Portuguese Minister of Science and Technology (MCTES) under 'Ciência 2007'.

References

[1] U. Schumann, *Subgrid-scale model for finite difference simulations of turbulent flows on plane channels and annuli*, J. Comput. Phys. 18 (1975), pp. 376–404.
[2] A. Yoshizawa, *A statistically-derived subgrid model for the large-eddy simulation of turbulence*, Phys. Fluids 25 (1982), pp. 1532–1538.
[3] E.G. Paterson and L.J. Peltier, *Detached-eddy simulation of high-reynolds-number beveled-trailling-edge boundary layers and wakes*, J. Fluids Eng. 127 (2005), pp. 897–906.
[4] K. Hanjalic, *Will RANS survive LES? A view of perspectives*, J. Fluids Eng. 127 (2005), pp. 831–839.
[5] C. Jiménez et al., *Subgrid scale variance and dissipation of a scalar field in large eddy simulations*, Phys. Fluids 13(2001), pp. 1748–1754.
[6] S. Ghosal et al., *A dynamic localisation model for large-eddy simulation of turbulent flows*, J. Fluid Mech. 286 (1995), pp. 229–255.
[7] M. Lesieur and O. Métais, *New trends in large-eddy simulations of turbulence*, Annu. Rev. Fluid Mech. 28 (1999), pp. 45–98.
[8] C. Meneveau and J. Katz, *Scale invariance and turbulence models for large-eddy simulation*, Annu. Rev. Fluid Mech. 32 (2000), pp. 1–32.
[9] S. Grag and Z. Warhaft, *On the small scale structure of simple shear flow*, Phys. Fluids 10 (1998), p. 662.
[10] A. Gilfason and Z. Warhaft, *On higher order passive scalar structure functions in grid turbulence*, Phys. Fluids 16 (2004), p. 4012.
[11] E. Garnier, O. Métais, and M. Lesieur, *Synoptic and frontal-cyclone scale instabilities in baroclinic jet flows*, *J. Atmos. Sci.* 55 (1998), pp. 1316–1335.
[12] C.B. da Silva and O. Métais, *On the influence of coherent structures upon interscale interactions in turbulent plane jets*, J. Fluid Mech. 473 (2002), pp. 103–145.
[13] C.B. da Silva and J.C.F. Pereira, *On the local equilibrium of the subgrid-scales: The velocity and scalar fields*, Phys. Fluids 17 (2005), 108103.
[14] H. Schmidt and U. Schumann, *Coherent structure of the convective boundary layer derived from large-eddy simulations*, J. Fluid Mech. 200 (1989), pp. 511–562.
[15] A. Yoshizawa and K. Horiuti, *A statistically-derived subgrid-scale kinetic energy model for the large-eddy simulation of turbulent flows*, J. Phys. Soc. Japan 54 (1985), pp. 2834–2839.
[16] K. Horiuti, *Large-eddy simulation of turbulent channel flow by one-equation modeling*, J. Phys. Soc. Japan 54 (1985), pp. 2855–2865.
[17] V.C. Wong, *A proposed statistical-dynamic closure method for the linear or nonlinear subgrid-scale stresses*, Phys. Fluids 4 (1992), pp. 1080–1082.
[18] A. Dejoan and R. Schiestel, *LES of unsteady turbulence via a one-equation subgrid-scale transport model*, Int. J. Heat Fluid Flow 23 (2002), p. 398.
[19] O. Debliquy, B. Knapen, and D. Carati, *A dynamic subgrid-scale model based on the turbulent kinetic energy*, in *Direct and Large-Eddy Simulations IV*, B.J. Geurts, R. Friedrich, and O. Métais, eds., Kluwer, Dordrecht, 2001, pp. 89–96.
[20] S. Krajnović and L. Davidson, *A mixed one equation subgrid model for large-eddy simulation*, Int. J. Heat Fluid Flow, 23 (2002), pp. 413–425.

[21] R. Schiestel and A. Dejoan, *Towards a new partially integrated transport model for coarse grid and unsteady turbulent flow simulations*, Theor. Comput. Fluid Dyn. 18 (2005), p. 443.

[22] L. Davidson and S. Peng, *k Hybrid LES–RANS modelling: A one-equation SGS model combined with a $k - w$ model for predicting recirculating flows*, Int. J. Numer. Methods Fluids 43 (2003), pp. 1003–1018.

[23] C. de Langhe, B. Merci, and E. Dick, *Hybrid RANS/LES modelling with an approximate renormalization group: I. Model development*, J. Turbul. 6 (2005).

[24] C. de Langhe et al., *Hybrid RANS/LES modelling with an approximate renormalization group: II. Applications* J. Turbul. 6 (2005), p. N14.

[25] T. Kajishima and T. Nomachi, *One-equation subgrid scale model using dynamic procedure for the energy dissipation*, J. Appl. Mech., Trans. ASME 73 (2006), pp. 368–373.

[26] F. Mathey and J.P. Chollet, Subgrid model of scaler mixing for large-eddy simulation of turbulent flows. In The Second ERCOFTAC Workshop on Direct and Large-Eddy Simulations, September 16–19 Grenoble, France (1996).

[27] H. Pitsch, *Large-eddy simulation of turbulent combustion*, Annu. Rev. Fluid Mech. 38 (2006), pp. 453–482.

[28] S. Grimaji and Y. Zhou, *Analysis and modeling of subgrid scalar mixing using numerical data*, Phys. Fluids 8 (1996), p. 1224.

[29] C. Jiménez, L. Valino, and C. Dopazo, *A priori and a posteriori tests of subgrid models for scalar transport*, Phys. Fluids 13(2001), pp. 2433–2436.

[30] C. B. da Silva and J. C. F. Pereira, *Analysis of the gradient-diffusion hypothesis in large-eddy simulations based on transport equations*, *Phys. Fluids* 19 (2007), 035106.

[31] W. Ashusrt et al., *Alignment of vorticity and scalar gradient with strain rate in simulated Navier–Stokes turbulence*, Phys. Fluids 30 (1987), pp. 2343–2353.

[32] M. Overholt and S. Pope, *Direct numerical simulation of a passive scalar with imposed mean gradient in isotropic turbulence*, Phys. Fluids 8 (1996), pp. 3128–3148.

[33] P. Vedula, P. Yeung, and R. Fox, *Dynamics of scalar dissipation in isotropic turbulence: A numerical and modelling study*, J. Fluid Mech. 433 (2001), pp. 29–60.

[34] J. Schumacher, K. Sreenivasan, and P. Yeung, *Very fine structures in scalar mixing*, J. Fluid Mech. 531 (2005), pp. 113–122.

[35] J. Schumacher and K. Sreenivasan, *Statistics and geometry of passive scalars in turbulence*, Phys. Fluids 17 (2005) 125107.

[36] C. Meneveau and J. O'Neil, *Scaling laws of the dissipation rate of turbulent subgrid-scale kinetic energy*, Phys. Rev. E 49(1994), pp. 2866–2874.

[37] S. Menon, P.K. Yeung, and W.W. Kim, *Effect of subgrid models on the computed interscale energy transfer in isotropic turbulence*, Comput. Fluids 25 (1996), pp. 165–180.

[38] S. Chumakov, *Scaling properties of subgrid-scale energy dissipation*, Phys. Fluids 19 (2007) 058104.

[39] C. Pierce and P. Moin, *A dynamic model for subgrid-scale variance and dissipation rate of a conserved scalar*, Phys. Fluids 12 (1998), p. 3041.

[40] A. Cook and W. Bushe, *A subgrid-scale model for the scalar dissipation rate in nonpremixed combustion*, Phys. Fluids 11 (1999), p. 746.

[41] B. Chaouat and R. Schiestel, *A new partially integrated transport model for subgrid stresses and dissipation rate for turbulent developing flows*, Phys. Fluids 17 (2005) 065106.

[42] S. Chumakov and C. Rutland, *Dynamic structure subgrid-scale models for large eddy simulation*, Int. J. Numer. Methods Fluids 47 (2005), pp. 911–932.

[43] ———, *Dynamic structure models for scalar flux and dissipation in large eddy simulation*, AIAA J. 42 (2004), pp. 1132–1139.

[44] U. Piomelli and J.R. Chasnov, *Large eddy simulations: Theory and applications*, kin in *Turbulence and Transition Modeling*, M. Hall, D.S. Henningson, A.V. Jhoannson and P. H. Alfredssoon, eds., Kluwer, Dordrecht, 1996.

[45] H. Kang and C. Meneveau, *Universality of large eddy simulation parameters across a turbulent wake behind a cylinder heated cylinder*, J. Turbul. 3 (2002), pp. 1–27.

[46] T. Watanabe and T. Gotoh, *Inertial-range intermittency and accuracy of direct numerical simulation for turbulence and passive scalar turbulence*, J. Fluid Mech. 590 (2007), pp. 117–146.

[47] H. Tennekes and J.L. Lumley, *A First Course in Turbulence*, The MIT Press, Cambridge, MA, 1972.

[48] F. Schmitt et al., *Direct investigation of the k-transport equation for a complex turbulent flow*, J. Turbul. 4 (2003), p. N21.

[49] B. Chaouat and R. Schiestel, *From single-scale turbulence models to multiple-scale and subgrid-scale models by Fourier transform*, Phys. Fluids 21 (2007), pp. 201–229.
[50] J. Smagorisky, *General circulation experiments with the primitive equations*, Mon. Weather Rev. 91 (1963), pp. 99–164.
[51] A. Yoshizawa, *Eddy-viscosity-type subgrid-scale model with a variable smagorinsky coefficient and its relationship with the one-equation model in large-eddy simulation*, Phys. Fluids 3 (1991), pp. 2007–2009.
[52] K. Alvelius, *Random forcing of three-dimensional homogeneous turbulence*, Phys. Fluids 11 (1999), pp. 1880–1889.
[53] V. de Borue and S. Orszag, *Local energy flux and subgrid-scale statistics in three dimensional turbulence*, J. Fluid Mech. 366 (1998), pp. 1–31.
[54] S. Liu, C. Meneveau, and J. Katz, *On the properties of similarity subgrid-scale models as deduced from measurements in a turbulent jet*, J. Fluid Mech. 275(1994), pp. 83–119.
[55] B. Vreman, B. Geurts, and H. Kuerten, *Reliazability conditions for the turbulent stress tensor in large-eddy simulation*, J. Fluid Mech. 278 (1994), pp. 351–362.
[56] R. Rogallo and P. Moin, *Numerical simulation of turbulent flows*, Annu. Rev. Fluid Mech. 16 (1984), pp. 99–137.
[57] J. Jimenez et al., *The structure of intense vorticity in isotropic turbulence*, J. Fluid Mech. 255 (1993), pp. 65–90.
[58] J. Jiménez and A. Wray, *On the characteristics of vortex filaments in isotropic turbulence*, J. Fluid Mech. 373 (1998), pp. 255–285.
[59] E.D. Siggia, *Numerical study of small-scale intermittency in three-dimensional turbulence*, J. Fluid Mech. 107 (1981), pp. 375–406.
[60] J.C.R. Hunt, A.A. Wray, and P. Moin, *Eddies, stream, and convergence zones in turbulent flows*, *Annual Research Briefs*, Center for Turbulence Research, Stanford, 1988.
[61] I. Dubief and F. Delcayre, *On coherent-vortex identification in turbulence*, J. Turbul. 1 (2000), p. N11.
[62] N. Park et al., *A dynamic subgrid-scale eddy viscosity model with a global model coefficient*, Phys. Fluids 18 (2006) 125109.
[63] K. Sreenivasan, *An update on the energy dissipation rate in isotropic turbulence*, Phys. Fluids 10 (1998), p. 528.
[64] N. Mazellier and J.C. Vassilicos, *The turbulence dissipation constant is not universal because of its universal dependance on large-scale flow topology*, Phys. Fluids 20 (2008), 015101.
[65] P. Burattini, P. Lavoie, and R.A. Antonia, *On the normalized turbulent energy dissipation rate*, Phys. Fluids 17 (2005), 098103.
[66] M. Germano et al., *A dynamic subgrid-scale eddy viscosity model*, Phys. Fluids 2 (1991), pp. 1760–1765.
[67] C. Fureby et al., *Differential subgrid stress models in large eddy simulations*, Phys. Fluids 9 (1997), pp. 3578–3580.
[68] F. Hamba, *An attempt to combine large eddy simulation with the $k-\varepsilon$ model in a channel-flow calculation*, Theoret. Comput. Fluid Dyn. 14 (2001), pp. 323–336.
[69] ———, *A hybrid RANS/LES simulation of turbulent channel flow*, Theor. Comput. Fluid Dyn. 16 (2003), pp. 387–403.

Bibliography

[1] U. Schumann. Subgrid-scale model for finite difference simulations of turbulent flows on plane channels and annuli. *J. Comp. Phys.*, 18:376–404, 1975.

[2] A. Yoshizawa. A statistically-derived subgrid model for the large-eddy simulation of turbulence. *Physics of Fluids*, 25:1532–8, 1982.

[3] E. G. Paterson and L. J. Peltier. Detached-eddy simulation of high-reynolds-number beveled-trailling-edge boundary layers and wakes. *Journal of Fluids Engineering*, 127:897–906, 2005.

[4] K. Hanjalic. Will rans survive les? a view of perspectives. *Journal of Fluids Engineering*, 127:831–9, 2005.

[5] C. Jiménez, F. Ducros, B. Cuenot, and B. Bédat. Subgrid scale variance and dissipation of a scalar field in large eddy simulations. *Physics of Fluids*, 13(6):1748–1754, 2001.

[6] C.B. da Silva and José C.F. Pereira. Analysis of the gradient-diffusion hypothesis in large-eddy simulations based on transport equations. *Physics of Fluids*, 19:035106, 2007.

[7] P. A. Davidson. *Turbulence: An Introduction for Scientists and Engineers.* Oxford University Press, New York, 2004.

[8] Arkadi Tsinober. *An Informal Introduction to Turbulence.* Kluwer Academic Publishers, New York, 2004.

[9] David C. Wilcox. *Turbulence Modeling for CFD.* DCW Industries, Inc., La Cañada, 1994.

[10] Uriel Frisch. *Turbulence: the legacy of A. N. Kolmogorov.* Cambridge University Press, New York, 1995.

[11] Pierre Sagaut. *Large Eddy Simulation for Incompressible Flows: An Introduction.* Springer, New York, 2006.

[12] H. Tennekes and J. L. Lumley. *A First Course in Turbulence.* Massachusets Institute of Technology, Cambridge, 1972.

[13] W. D. McComb. *The Physics of Fluid Turbulence.* Clarendon Press, Oxford, 1992.

[14] Stephen B. Pope. *Turbulent Flows.* Cambridge University Press, New York, 2000.

[15] Heinz Pitsch. Large-Eddy Simulation of Turbulent Combustion. *Annual Review of Fluid Mechanics*, 38:453–82, 2006.

[16] Marcel Lesieur, Olivier Métais, and Pierre Comte. *Large-Eddy Simulations of Turbulence*. Cambridge University Press, New York, 2005.

[17] O. Métais and M. Lesieur. Spectral large-eddy simulation of isotropic and stably stratified turbulence. *Journal of Fluid Mechanics*, 239:157–94, 1992.

[18] Robert H. Kraichnan. Eddy Viscosity in Two and Three Dimensions. *Journal of the Atmospheric Sciences*, 33:1521–36, 1976.

[19] G. K. Batchelor. *The theory of homogeneous turbulence*. Cambridge University Press, Cambridge, 1953.

[20] Vadim Borue and Steven A. Orzag. Local energy flux and subgrid-scale statistics in three-dimensional turbulence. *Journal of Fluid Mechanics*, 366:1–31, 1998.

[21] C.B. da Silva and O. Métais. On the influence of coherent structures upon interscale interactions in turbulent plane jets. *Journal of Fluid Mechanics*, 473:103, 2002.

[22] C.B. da Silva and J.C.F. Pereira. On the local equilibrium of the subgrid-scales: The velocity and scalar fields. *Physics of Fluids*, 17:108103, 2005.

[23] Jorge Bardina, Joel H. Ferziger, and W. C. Reynolds. Improved subgrid-scale models for large-eddy simulation. *AIAA*, 366:1–31, 1998.

[24] H. Schmidt and U. Schumann. Coherent structure of the convective boundary layer derived from large-eddy simulations. *Journal of Fluid Mechanics*, 200:511–62, 1989.

[25] A. Yoshizawa and K. Horiuti. A statistically-derived subgrid model for the large-eddy simulation of turbulent flows. *J. Phy. Soc. Japan*, 54:2834–9, 1985.

[26] Takeo Kajishima and Takayuki Nomachi. One-Equation Subgrid Scale Model Using Dynamic Procedure for the Energy Production. *Journal of Applied Mechanics, Transactions of the ASME*, 73:368–373, 2006.

[27] J. W. Deardorff. The Use of Subgrid Transport Equations in a Three-Dimensional Model of Atmospheric Turbulence. *Journal of Fluids Engineering*, pages 429–438, 1973.

[28] Fujihiro Hamba. An attempt to combine large eddy simulation with the $\mathrm{k}-\varepsilon$ model in a channel-flow calculation. *Theoretical and Computational Fluid Dynamics*, 14:323–336, 2001.

[29] Fujihiro Hamba. A hybrid rans/les simulation of turbulent channel flow. *Theoretical and Computational Fluid Dynamics*, 16:387–403, 2003.

[30] L. Temmerman, M. Hadžiabdić, M. Leschziner, and K. Hanjalić. A hybrid two-layer urans-les approach for large eddy simulation at high reynolds numbers. *International Journal of Heat and Fluid Flow*, 26:173–190, 2005.

[31] C.B. da Silva, S. Rego, and J.C.F. Pereira. Analysis of the viscous/molecular subgrid-scale dissipation terms in LES based on transport equations: A priori tests. *Journal of Turbulence*, 9:453–82, 2008.

[32] K. Alvelius. Random forcing of three-dimensional homogeneous turbulence. *Physics of Fluids*, 11(7):1880–1889, 1999.

[33] C. Canuto, M. Y. Hussaini, A. Quarteroni, and T. A. Zang. *Spectral Methods in Fluid Dynamics*. Springer-Verlag, 1987.

[34] Bernard J. Geurts. *Elements of direct and large-eddy simulation*. R.T. Edwards, Inc., Philadelphia, 2006.

[35] Heitor Pina. *Métodos Numéricos*. McGraw-Hill, Lisboa, 1995.

[36] Douglas C. Montgomery and Douglas C. Runger. *Applied Statistics and Probability for Engineers*. John Wiley and Sons, New York, 1994.